

ABSTRACT

Title of dissertation: SYNCHRONIZATION OF CHAOTIC
OPTOELECTRONIC OSCILLATORS:
ADAPTIVE TECHNIQUES AND THE
DESIGN OF OPTIMAL NETWORKS

Bhargava Ravoori, Doctor of Philosophy, 2011

Dissertation directed by: Professor Rajarshi Roy
Department of Physics

Synchronization in networks of chaotic systems is an interesting phenomenon with potential applications to sensing, parameter estimation and communications. Synchronization of chaos, in addition to being influenced by the dynamical nature of the constituent network units, is critically dependent upon the maintenance of a proper coupling between the systems. In practical situations, however, synchronization in chaotic networks is negatively affected by perturbations in the coupling channels. Here, using a fiber-optic network of chaotic optoelectronic oscillators, we experimentally demonstrate an adaptive algorithm that maintains global network synchrony even when the coupling strengths are unknown and time-varying. Our adaptive algorithm operates by generating real-time estimates of the coupling perturbations which are subsequently used to suitably adjust internal node parameters in order to compensate for external disturbances. In our work, we also examine the influence of network configuration on synchronization. Through measurements of the convergence rate to synchronization in networks of optoelectronic systems,

we show that having more network links does not necessarily imply faster or better synchronization as is generally thought. We find that the convergence rate is maximized for certain network configurations, called *optimal* networks, which are identified based on the eigenvalues of the coupling matrix. Further, based on an analysis of the eigenvectors of the coupling matrix, we introduce a classification system that categorizes networks according to their sensitivity to coupling perturbations as *sensitive* and *nonsensitive* configurations. Though our experiments are performed on networks consisting of specific nonlinear optoelectronic oscillators, the theoretical basis of our studies is general and consequently many of our results are applicable to networks of arbitrary dynamical oscillators.

SYNCHRONIZATION OF CHAOTIC OPTOELECTRONIC
OSCILLATORS: ADAPTIVE TECHNIQUES AND THE
DESIGN OF OPTIMAL NETWORKS

by

Bhargava Ravoori

Dissertation submitted to the Faculty of the Graduate School of the
University of Maryland, College Park in partial fulfillment
of the requirements for the degree of
Doctor of Philosophy
2011

Advisory Committee:
Professor Rajarshi Roy, Chair/Advisor
Professor Thomas E. Murphy
Dr. John C. Rodgers
Professor Michelle Girvan
Professor Michael A. Coplan

© Copyright by
Bhargava Ravoori
2011

Dedication

To my parents and my sister, whom I can never thank enough.

Chaos is inherent in all compounded things. Strive on with diligence.

-Sidhartha Gautama Buddha.

Acknowledgments

It has been said “Gratitude is the least articulate of the emotions, especially when it is deep”. I find it extremely hard to fully express my gratitude to all those people who made this thesis possible. I will attempt, anyway.

First and foremost, I would like to thank my advisor Prof. Rajarshi Roy and my co-advisor Prof. Thomas Murphy for being such wonderful mentors. They have been excellent guides during my journey into the beautiful world of chaos. They knew exactly when to hold my hand and nudge me in the right directions, and when to let me explore new avenues on my own. Their constant encouragement and invaluable support at various points of my graduate life will never be forgotten.

I sincerely thank all my committee members, who have agreed to take out time from their busy schedules to review my thesis. Special thanks to Dr. Rodgers for valuable suggestions and help with network analyzer measurements.

A big influence on my graduate studies came from the Hands-on Research in Complex Systems Schools in India, Brazil and Cameroon. During these schools, I met many people who have left an indelible mark on my life. I fondly remember the many good times we had during these trips. Thanks to everybody involved.

I would also like to thank Dr. Ira Schwartz, and Dr. Eric Forgoston for advice and stimulating discussions at various points of time. Special thanks to Prof. Edward Ott for guiding the experiments on adaptive synchronization. Prof. Francesco Sorrentino and Anurag Setty collaborated with us on the adaptive synchronization project and performed some of the numerical simulation work. Thanks are also due

to our collaborators at Northwestern University, Prof. Adilson Motter and Dr. Jie Sun, who provided theoretical support to our work on optimal networks.

I thank all my friends for always being there. My labmates– Adam, Caitlin, Hien and Karl who have been extremely supportive and always a great company. My friends from college, Murali and Chanti, for always knowing how to bring a smile to my face. Thanks to Cheeku for being a special part of my life. To Madan and Madhu for their support and the many wonderful dinners together.

I especially remember my high school teachers, Mr. Paul and Mr. Prasad, for their encouragement and for getting me interested in Mathematics and Physics. Thanks to Prof. R. R. Mishra and Prof. Gaurav Dar for being great teachers and mentors during college and encouraging me to take up graduate studies.

Thanks to Shyam Mehrotra for his help with soldering tasks. I would also like to thank Nancy Boone for purchasing help and Don Martin for ensuring our safety in the lab.

Table of Contents

List of Figures	vii
1 Introduction	1
1.1 Chaos and Synchronization	1
1.2 Applications of Chaos Synchronization	3
1.2.1 Application of Chaos Synchronization to Secure Communications	4
1.2.2 Application of Chaos Synchronization to Sensing	7
1.3 Influence of Network Structure on Synchronization	8
1.4 Outline of the Thesis	9
2 Optoelectronic Chaos Generator	12
2.1 Construction of a Time-delayed Optoelectronic Feedback Loop	13
2.1.1 Laser Diode	15
2.1.2 Mach-Zehnder Electro-optic Intensity Modulator	18
2.1.3 Photoreceiver	22
2.1.4 Filtering and Time-delay	23
2.1.5 Voltage Amplifier	30
2.2 Mathematical Modeling	31
2.3 Dynamical Behavior of the Feedback Loop	35
3 Coupled Optoelectronic Feedback Oscillators	41
3.1 Mathematical Formulation	42
3.2 Synchronization of Coupled Oscillators: Experiments	45
3.3 Stability Analysis: Master Stability Function	53
3.4 Summary	60
4 Adaptive Synchronization of Coupled Optoelectronic Oscillators	61
4.1 Adaptive Algorithm	63
4.2 Implementation of the Adaptive Algorithm: Two-node Network	67
4.3 Experimental Results from a Two-node Network	70
4.4 Adaptive Synchronization: Three-node Network Experiments	86
4.5 Summary	94
5 Optimal Network Topologies for Synchronization	95
5.1 Synchronizability of a Network: Past Research	97
5.2 Experimental Setup: Four-node Network	99
5.3 Optimal Network Configurations for Synchrony	101
5.4 Experimental Measurements of Optimality	103
5.5 Influence of Connection Geometry	111
5.6 Summary	120

6	Conclusions and Future Research	121
6.1	Conclusions	121
6.2	Discussion: Generality and Significance of Results Presented	124
6.3	Future Directions	125
	Bibliography	128

List of Figures

1.1	Communication through chaos masking.	6
2.1	Schematic of the nonlinear time-delayed optoelectronic feedback loop.	14
2.2	Semiconductor laser diode output characteristics.	17
2.3	Transmission characteristics of a Mach-Zehnder electro-optic modulator.	19
2.4	Photoreceiver circuit schematic.	23
2.5	Simplified block diagram of a DSP board.	26
2.6	Measured amplitude response of the digital filter.	29
2.7	Implementation of a time-delay using the DSP board.	30
2.8	Circuit schematic of the amplifier used in the feedback loop.	31
2.9	Mathematical block diagram of the optoelectronic feedback loop.	34
2.10	Measurement of the feedback gain β	37
2.11	Dynamical behavior of the optoelectronic feedback loop.	39
2.12	Measured and simulated bifurcation diagrams for the optoelectronic oscillator.	40
3.1	Block diagram illustration of the coupling of two optoelectronic oscillators.	46
3.2	Dynamical behavior of coupled optoelectronic feedback loops.	50
3.3	Range of coupling strength for stable synchrony	51
3.4	Measurement of the maximal transverse Lyapunov exponent (TLE), $-\mu$	54
3.5	Maximal TLE, $-\mu$, as a function of the coupling strength κ	55
3.6	Master stability function (M) and the regime of stable synchronization.	58
4.1	Experimental schematic of a unidirectionally coupled two-oscillator network.	69
4.2	Response of the 2-node system to a step change in the coupling strength κ	72
4.3	Numerical simulation of the response of an adaptive 2-node system to a step change in the coupling strength κ	73
4.4	Adaptive tracking of a sinusoidal modulation of the coupling strength κ	76
4.5	Adaptive synchronization algorithm applied to track an arbitrary coupling perturbation.	77
4.6	Synchronization of the transmitter and receiver dynamics using the adaptive scheme.	78
4.7	Synchronization error θ as a function of the modulation frequency f_m	82
4.8	Improvement in synchronization error θ due to adaptive control.	83
4.9	Figure of Merit (FOM) as a function of the modulation frequency f_m	84
4.10	Tracking measure η as a function of the modulation frequency f_m	85
4.11	Experimental schematic of a network of three optoelectronic oscillators.	87

4.12	Maintenance of synchrony on a network of three optoelectronic oscillators.	91
4.13	Adaptive tracking of multiple simultaneous perturbations.	92
5.1	Experimental schematic of an optoelectronic node in a 4-node network.	99
5.2	Synchronizability measure σ as a function of the number of network links m	102
5.3	A set of 4-node optimal and suboptimal configurations.	104
5.4	Mean convergence rate to synchronization as a function of the number of network links.	106
5.5	Numerical measurement of convergence rate of optimal and suboptimal configurations of a 50-node network.	108
5.6	Measurement of the MSF along the real axis.	109
5.7	Synchronization range ρ , inferred from the measured MSF, as a function of the number of network links m	111
5.8	Optimal configurations with $m = 3$ for the 4-node network.	113
5.9	Structure of all optimal and suboptimal binary networks with $N = 4$ nodes.	114
5.10	Differentiating behavior between sensitive and nonsensitive networks.	115
5.11	Simulated convergence transients of 50-node network configurations with varying geometric degeneracy.	118
5.12	Transient to synchronization for sensitive and nonsensitive networks with $N = 50$ nodes.	119

Chapter 1

Introduction

1.1 Chaos and Synchronization

Chaos is the complex aperiodic time-evolution of a deterministic nonlinear system. It is encountered in a wide variety of fields including mechanics [1], biology [2, 3], chemistry [4, 5], electronics [6, 7], and optics [8, 9]. The hallmark of chaos is its extreme sensitivity to perturbations. Two chaotic systems starting from very close initial conditions quickly diverge in time leading to wildly different trajectories. The sensitivity of chaos to perturbations makes long-term predictions of chaotic systems infeasible because even small errors in measurement or estimation of the dynamical variables grow as the system evolves in time. In this context, the proposition that two coupled chaotic systems can be synchronized (i.e. they can be made to evolve along the same trajectory in lock-step) came as a surprise to the nonlinear dynamics community [10–12]. This type of coordinated time-evolution is termed *isochronal synchronization*. Here, two systems are said to be coupled if they exchange partial information about their respective dynamical states. The phenomenon of synchronization of nonlinear oscillators is pervasive in nature and science. Fireflies flashing in unison [13], the synchronous operation of pacemaker cells in the heart [14], the synchronization of Josephson-junction arrays [15] and lasers [16, 17] are a few examples. The condition of epilepsy has also been attributed

to the simultaneous firing of neurons in a specific region of the brain [18].

Initial research on chaos synchronization was mostly theoretical and dealt with low-dimensional [19] systems that are mathematically described by a set of ordinary differential equations (ODEs). The description of a dynamical system by a set of ODEs implicitly assumes that the interactions between the dynamical variables are instantaneous. This assumption is justified only if the signal propagation delays are much smaller than the time-scale of the dynamics. In many systems, however, this is not the case and the effect of time delays becomes important. Time-delayed systems are found in almost every field of science including physics, biology and chemistry [20]. For example, in Ref. [2], Mackey and Glass modeled the regulation of breathing rate and the production of white blood cells as nonlinear time-delayed feedback processes. The dynamics of a time-delayed feedback system is affected not just by its present state but by the past states as well. Such systems are mathematically described by delay-differential equations which, in principle, are infinite-dimensional because a continuous history function defined over at least one delay period is required to solve the equations. The interplay of nonlinearity and memory can lead to a rich variety of dynamical behavior including high-dimensional chaos. Experimental studies of the synchronization of time-delayed chaotic systems have implications for our fundamental understanding of nonlinear oscillators and also for many practical applications. However, the difficulty in achieving and maintaining stable synchronization of time-delayed nonlinear oscillators due to their inherent dynamical complexity and sensitivity to coupling perturbations, meant that this area of research has not received the attention it deserves.

In the work presented here, we focus on the experimental synchronization of a network of chaotic optoelectronic time-delayed feedback loops. The systems considered here serve as versatile laboratory models of dynamical oscillators commonly encountered in nature, embodying feedback, nonlinearity and time-delays. Thus the results presented here can help us glean insight into the behavior of networks of nonlinear oscillator systems in general. In addition to enhancing our understanding of the behavior of nonlinear oscillator networks, our research is also motivated by the applications of chaos synchronization. Dynamical oscillators similar to the ones we study have been used for microwave signal generation [21] and recently for encrypted communications [22]. In this introductory chapter, we provide a brief overview of some practical applications of chaos synchronization and explain the pertinence of the research presented here to these applications.

1.2 Applications of Chaos Synchronization

Since the idea of chaos synchronization was introduced, many practical applications of this phenomenon have been proposed. Methods based on chaos synchronization find applications in secure communications [23, 24], prediction [25], parameter estimation [26] and sensing [27]. In this section, we briefly discuss the application of chaos synchronization to communication and sensing while providing some relevant background.

1.2.1 Application of Chaos Synchronization to Secure Communications

Synchronization, in one form or the other, is the central concept on which all communication is based. For successful communication between any two entities, it is imperative for them to share some common features, be it language, timing or information about encryption protocols. For example, in digital communication systems, the recovery of the transmitted message is possible at the receiver only if it has a clock that is synchronized with the transmitter clock. As it is in conventional communication systems, synchronization is an essential concept in chaos-based systems as well. The basic idea of chaos-based secure communication is to utilize the inherent complexity of a chaotic system to provide security by making the transmitted message unrecognizable to possible eavesdroppers. Fig. 1.1 illustrates the idea of a simple chaos-based encrypted communication system. Although other chaos encryption schemes which supposedly offer better security have been proposed [28,29], the simple system presented in Fig. 1.1 captures the main idea. It relies on a chaotic transmitter system and a receiver that are synchronized with each other. The chaotic signal generated by the transmitter is superimposed over the message signal, effectively concealing it from potential eavesdroppers. The resultant encrypted signal is then relayed to the receiver over the communication channel. The receiver has a chaos generator (a replica of the one used at the transmitter) which is synchronized to the transmitter through the chaotic signal that is shared over the communication channel. Here, the communication channel itself acts as the coupling medium be-

tween the transmitter and the receiver. The message is recovered by subtracting the superimposed chaos. This application of chaos synchronization for secure communication was first proposed by Cuomo and Oppenheim in the context of electronic systems [23]. VanWiggeren and Roy demonstrated encrypted communication using chaotic laser systems [24, 30]. Recently, Argyris *et al.* implemented this communication scheme to send digital information at gigabit per second bit-rates over the fiber-optic telecommunications network of Athens [22]. Argyris *et al.* exploited the high-dimensional chaos generated by a nonlinear time-delayed optoelectronic system to encrypt digital information which was then relayed to a receiver several kilometers away. The real significance of the work was that (a) it used a real fiber-optic network, and (b) it used commercially-available components.

A crucial aspect of the experiment described above is the maintenance of synchrony between the transmitter and receiver nodes. Lack of proper synchronization leads to a poor bit-error rate thereby degrading the communication process. The synchronization of chaotic oscillators is critically dependent upon the maintenance of a proper coupling. Channel change or ‘drift’ is a potentially common situation (e.g., due to environmental fluctuations) and especially so when the coupling channel spans several kilometers. In this thesis, we report results from the implementation of an adaptive strategy [27] that maintains network synchronization by dynamically adjusting the internal parameters of the coupled oscillators to compensate for unknown external perturbations. The adaptive algorithm thus provides robust synchronization thereby improving the reliability of the communication process. Some results on this topic presented in this thesis have also been published in Refs. [31,32].

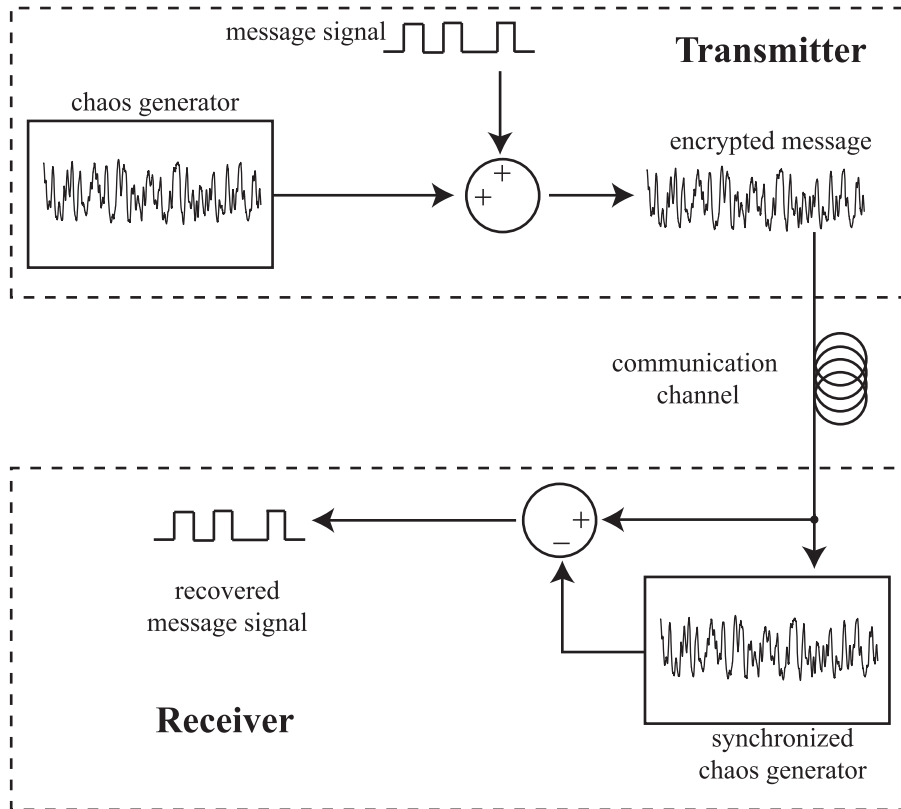


Figure 1.1: Communication through chaos masking. The message signal is encrypted by the transmitter by superimposing a chaotic signal. The masked signal is relayed to the receiver over the communication channel. Through the transmitted masked signal, the receiver chaos generator is synchronized with the chaos generated at the transmitter. The message is recovered by the receiver by subtracting the superimposed chaotic component.

1.2.2 Application of Chaos Synchronization to Sensing

As discussed in the previous section, chaos synchronization is sensitive to perturbations of the coupling channels. This sensitivity of chaos synchronization to coupling strength fluctuations can be harnessed to realize practical sensor applications.

In Ref. [27], Sorrentino and Ott conceived a network-based adaptive algorithm that, in the process of maintaining global synchronization, builds an estimate of unknown coupling perturbations. In order to realize a sensor, we implement this adaptive algorithm on a fiber-optic network of nonlinear chaotic oscillators envisioned to be distributed in the region of space that is to be monitored. Even though, in our experiments, the chaotic light signals exchanged between the oscillators are enclosed in fiber-optic cables, a free-space communication scenario can easily be realized. The coupling in our experimental network is engineered such that, initially, global isochronal synchronization of the network is established. In this setting, any external intruding element introduces a disturbance in the coupling channels which leads to the loss of synchrony in the network. However, by employing the adaptive control algorithm, each network node suitably adjusts its internal parameters to compensate for the external perturbations and network synchrony is quickly regained. Now, by analyzing the local adjustments each node had to make in order to regain synchrony, we can determine the original coupling perturbation. In this thesis, we present a proof-of-concept demonstration of this real-time distributed sensor through experiments performed on networks with two and three

nodes. First, we establish the success of the adaptive strategy in tracking a single coupling channel using a two-node network [31]. Then, using a three-node network we demonstrate the successful tracking of simultaneously occurring perturbations in multiple network links [32].

1.3 Influence of Network Structure on Synchronization

Another aspect of chaos synchronization, that hasn't received much experimental attention in the past, involves the study of the influence of network structure on chaos synchronization. A study of the influence of network structure on synchronization has implications for understanding the emergence of collective behavior in several natural and man-made complex systems.

Synchronization in a network of dynamical oscillators depends both on the nature of the dynamical units and on the properties of the interaction network. In Ref. [33], Pecora and Carroll theoretically addressed the question of whether or not a given network configuration of dynamical oscillators results in stable synchronization. By modeling network synchronization in terms of diffusively-coupled identical oscillators, they showed that the stability of the synchronous behavior is entirely determined by the eigenvalue spectrum of the coupling matrix that describes the network structure. However, in many situations, it is very important to not just determine whether a given network of chaotic oscillators synchronizes, but *how well* it does. This question has attracted a huge interest within the complex networks community. Several assertions, all based on theoretical analysis, have been made

about the influence of network structure on various synchronization properties such as the minimum amount of coupling required to synchronize a network of dynamical oscillators, the range of coupling strength over which synchronization is stable, the rate at which synchronization is achieved, etc. . . [34–40]. Recently, Nishikawa and Motter predicted that binary networks of dynamical systems optimal for synchronization have a quantized number of links, in multiples of a constant that depends only on the number of nodes [41]. In this thesis, we present the first experimental results that verify this claim. Specifically, we measure the rate of convergence to synchronization in a network of chaotic optoelectronic nodes as the number of network links are varied. We observe that the convergence rate indeed depends nonmonotonically on the number of links as is predicted in Ref. [41]. Further, we observe and discover that networks with the same number of nodes and coupling links, and with identical eigenvalues of the coupling matrix, which are theoretically predicted to have the same asymptotic synchronization properties can exhibit fundamentally different approaches to synchronization in the real-world. We explain this previously unnoticed significant difference in terms of the properties of the eigenvectors of the associated coupling matrices [42].

1.4 Outline of the Thesis

The material presented in this thesis is organized into four chapters.

Chapter 2 is devoted to discussing the construction of a nonlinear time-delayed optoelectronic feedback loop capable of producing a wide variety of dynamical be-

behavior ranging from periodic oscillations to high-dimensional chaos. We present details of the operational characteristics of the various elements that make up our feedback oscillator. A mathematical model of the feedback loop is developed and the parameters that affect the behavior of the oscillator are identified. Experimental measurements and numerical simulations showing the behavior of the feedback loop are reported.

In Chapter 3, we focus on isochronal synchronization of coupled optoelectronic oscillators. We discuss the mathematical representation of a general network of oscillators in terms of a coupling matrix and present the associated dynamical equations. We present experimental measurements showing synchronization of two coupled chaotic optoelectronic feedback loops and identify the coupling parameter range over which synchronization is stable. We also discuss various measures that quantify the synchronization behavior of the coupled oscillators.

In Chapter 4, we discuss the details of the adaptive algorithm designed for the maintenance of synchronization. We present details of the implementation of this algorithm on networks composed of two and three optoelectronic oscillators. Experimental results show both the maintenance of network synchronization and the tracking of *a priori* unknown coupling strength fluctuations.

Chapter 5 is devoted to the study of the influence of network structure on synchronization. First, the experimental construction of a binary network with 4 optoelectronic feedback loops is discussed. We then report experimental results showing the non-monotonic dependence of the convergence rate to synchronization on the number of network connections, allowing us to identify networks that are

optimal for synchronization. Finally, we propose a classification system of networks, as *sensitive* and *nonsensitive* configurations, based on the eigenvector properties of the associated coupling matrix. We supplement our experimental observations with numerical simulations that explicitly show the applicability of the discussed methods to larger networks.

Chapter 6 provides a conclusion to the thesis and discusses future work.

Chapter 2

Optoelectronic Chaos Generator

This chapter is devoted to describing the construction and behavior of a non-linear optoelectronic time-delayed feedback oscillator. The optoelectronic oscillator described here is built from commercially available standard telecommunications and electronic equipment and is capable of generating a wide variety of dynamical behavior ranging from periodic oscillations to high-dimensional chaos. It forms the elemental constituent of networks considered in the following chapters.

We will begin by describing the basic architecture of the oscillator in Sec. 2.1. The theoretical characteristics of the various components used in its construction are detailed and experimental measurements of the behavior of the various elements are presented.

In Sec. 2.2, we develop the equations that model the dynamical behavior of the oscillator. Various parameters that affect the dynamics of the nonlinear feedback loop are also identified in this section.

In Sec. 2.3 we examine the dynamical behavior of the oscillator as the feedback parameters are changed. Experimental measurements of the dynamical behavior are presented along with numerical results obtained from simulating the mathematical equations developed in Sec. 2.2.

2.1 Construction of a Time-delayed Optoelectronic Feedback Loop

In this section, we present details of the nonlinear optoelectronic oscillator which serves as the basic dynamical element in the network studies presented in the following chapters. An experimental schematic of our optoelectronic oscillator is shown in Fig. 2.1. The oscillator is composed of a semiconductor laser diode, a nonlinear electro-optic intensity modulator (called a Mach-Zehnder modulator), a photoreceiver, a bandpass filter, a time-delay and an amplifier connected as a feedback loop. The bandpass filter and the time-delay are implemented digitally using a digital signal processing (DSP) board. The characteristics of these components are discussed in detail in this section. First, we briefly describe how these components are configured as a feedback loop. In our optoelectronic system, the laser diode acts as a source of a steady optical power. The output from the laser is fiber-optically coupled into the Mach-Zehnder electro-optic modulator. An inline polarization controller allows us to align the polarization of the laser light with the polarization accepted by the modulator, thereby maximizing the amount of light coupled into the modulator. The electro-optic modulator varies the intensity of the input light based on an applied electrical voltage. The optical signal output by the modulator is converted into an electrical voltage signal by the photoreceiver. This voltage signal is then electronically filtered, time-delayed and amplified. The resultant signal is then applied to the electrical input to the modulator to control its optical output.

A good understanding of nonlinear time-delayed feedback systems has implications for many fields of science and technology. The coordination of animal motor

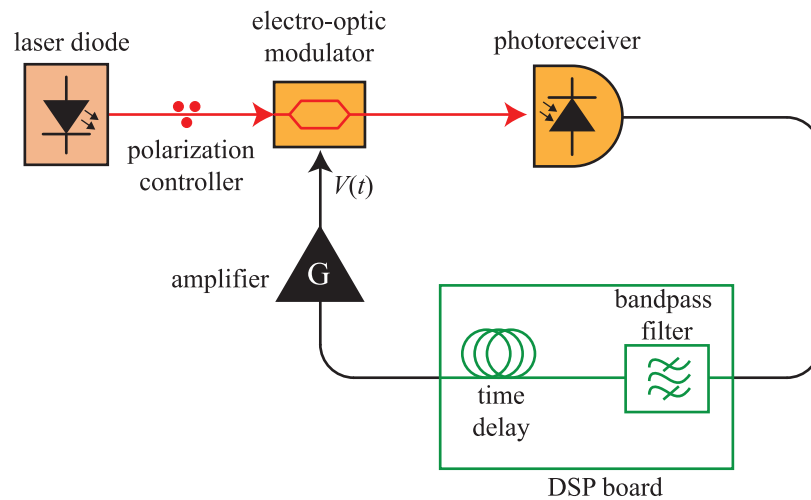


Figure 2.1: Schematic of the nonlinear time-delayed optoelectronic feedback loop. The feedback loop featured here comprises modular optoelectronic and electronic components and is capable of generating a wide variety of dynamical behaviors. It consists of a semiconductor laser diode, a Mach-Zehnder electro-optic modulator, a photoreceiver, a DSP board which implements bandpass filtering and time-delay operations, and an amplifier connected as a feedback loop.

skills, the spread of epidemics, the regulation of the rate of chemical reactions are some interesting examples where time-delayed feedback plays a crucial role [20]. In control systems, time-delayed feedback is known to lead to interesting dynamics. For example, phase-locked loops with time-delay are known to behave chaotically [43]. The optoelectronic feedback loop considered in our experiments presents an easily assembled, controllable nonlinear time-delayed feedback system that allows us to study the properties of delay interactions in general. Optoelectronic feedback loops, similar to the one described here, have been the subject of past research and are known to generate robust chaos at sufficiently high feedback strengths [44, 45]. Chaos generators with this construction have also been used in encrypted optical communications [22]. In the following subsections we discuss the characteristics of the various elements used in the construction of our optoelectronic feedback system.

2.1.1 Laser Diode

A semiconductor distributed feedback (DFB) laser serves as the source of optical power in our feedback loop. Semiconductor lasers are perhaps the most ubiquitous kind of lasers today due to their easy operation and low-cost. They are made by sandwiching an active semiconductor gain medium between two passive semiconductor layers with a comparatively larger band-gap thereby creating a double heterostructure to confine electrons and holes. The outer passive layers are also designed to have a higher refractive index compared to the active layer thereby producing an optical waveguide that confines the photons in the active layer, allowing

laser action. Distributed feedback occurs due to the presence of an optical Bragg grating etched on the outer passive layers of the laser. The Bragg grating acts as a mirror, selectively reflecting only one wavelength. This creates a single-mode resonator, unlike a Fabry-Perot cavity which supports many longitudinal modes. The word ‘distributed’ implies that reflection (feedback) occurs not at a single point (as in a Fabry-Perot cavity) but at many points all along the grating. Due to the presence of the grating, DFB lasers have a narrow line-width thereby producing a nearly monochromatic light output. By appropriately choosing the active semiconductor material, semiconductor lasers can be made to operate at wavelengths ranging anywhere from 370 nm to 2.6 μm . The semiconductor lasers used in our experiments lase at a wavelength ≈ 1550 nm. This wavelength is especially significant to the telecommunications industry since fiber-optic cables have the least loss at this wavelength. Fig. 2.2(a) shows a commercially available semiconductor laser of the kind used in our experiments (Bookham LC25W4932BA). The laser diodes used in our experiments have an integrated thermo-electric cooler which maintains a steady temperature (to within 0.01 K) thus ensuring the wavelength and power stability of the optical output.

The pump energy required to initiate lasing action in a semiconductor laser comes from driving an electric current through the laser. Under sufficient electrical excitation, a population inversion is created in the energy levels of the active medium. Under these conditions, photons created by the recombination of carriers are amplified through stimulated emission leading to the laser output. The minimum current required to establish population inversion and thus turn on the laser

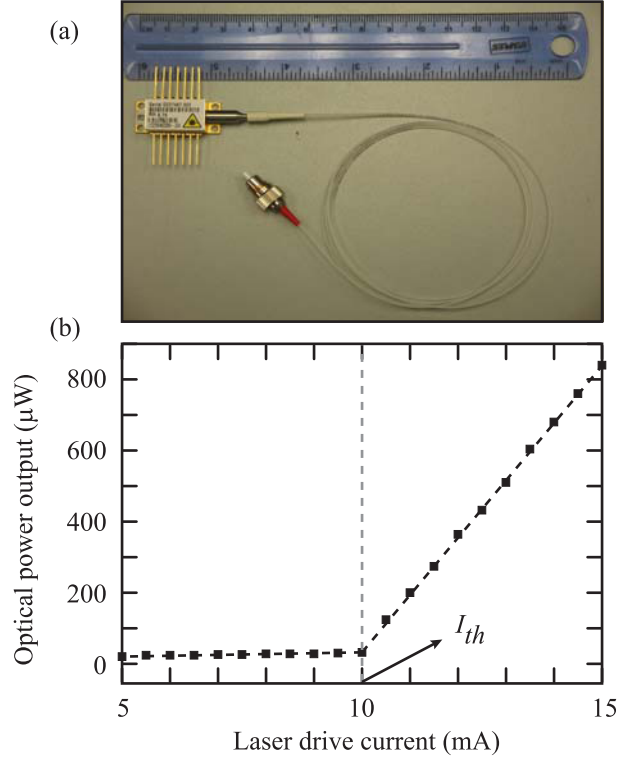


Figure 2.2: Semiconductor laser diode output characteristics. (a) A commercially available laser diode used in our experiments. (b) Optical output characteristics of the laser as a function of the drive current. The optical output turns on when the drive current exceeds the threshold current I_{th} identified by the vertical dashed line.

output is called the *threshold current*, I_{th} . In our experiments, we use a laser diode driver module (ILX LDC3908) to supply a well regulated steady electrical current to the laser diodes. Fig. 2.2 presents the input-output characteristics of a semiconductor laser used in our experiments. It shows the output optical power as function of the current that drives the laser. It has a nonlinear characteristic with the optical output turning on when the drive current exceeds the threshold. In our experiments, we operate the laser in the linear regime above threshold producing a steady optical power output, P_0 , ranging from 0.2 mW to 4 mW.

2.1.2 Mach-Zehnder Electro-optic Intensity Modulator

The Mach-Zehnder electro-optic intensity modulator (hereby referred to as just Mach-Zehnder modulator or MZM) produces the nonlinearity in our time-delayed feedback loop. It is commercially available as an integrated photonic device and is commonly used by the telecommunications industry to modulate data onto an optical carrier [46]. It can operate at modulation speeds of several tens of Gigabits per second. The Mach-Zehnder modulator is essentially an optical interferometer with transmission characteristics controlled by an applied electrical voltage.

The construction of an MZM is shown in Fig. 2.3 (a). It consists of an input optical waveguide that is split into two different optical paths of equal lengths (of the order of a few centimeters). The two paths are subsequently recombined to form the output optical waveguide. By virtue of this construction, an incoming light signal is split into two components of equal power and made to travel down different paths before being recombined at the output. If the optical signals traveling down the two paths arrive at the output in phase with each other, they interfere constructively leading to the complete transmission of the input signal. If, however, they do not arrive in phase, the signal is attenuated to a degree that is determined by their phase difference.

In an MZM, a voltage-controlled phase difference is induced between the two paths using the electro-optic effect. Electro-optic effect refers to the phenomenon in which a material's optical properties, such as the refractive index, depend on the applied electric field [47]. Linear electro-optic effect (also known as the Pockels effect)

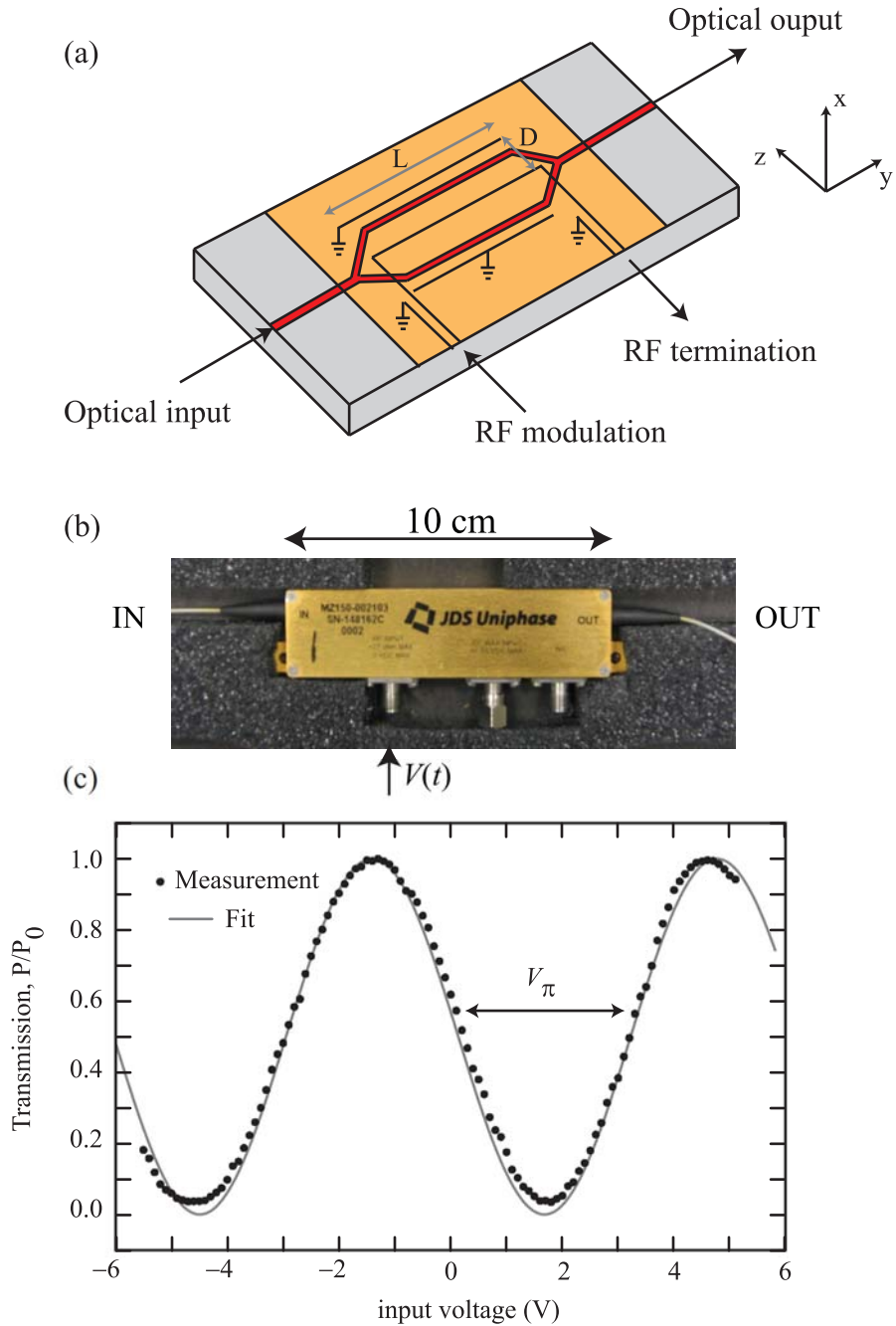


Figure 2.3: Transmission characteristics of a Mach-Zehnder electro-optic modulator. (a) Schematic of the modulator. The modulator is an optical interferometer with a voltage-controlled transmission characteristic. (b) A commercially available electro-optic modulator. (c) Transmission of an electro-optic modulator as a function of the applied voltage. The transmission follows a \cos^2 (●) characteristic as the minimum least-squares fit shows (gray line).

describes the situation where the first-order effect of the electric field dominates over higher-order influences. The waveguides of the MZMs used in our experiments are made of a linear electro-optic crystal called Lithium Niobate (LiNbO_3). LiNbO_3 is a uniaxial crystal i.e. it has one crystal axis that is different from the other two axes. This axis, called the optic axis, is denoted in Fig. 2.3 (a) as the z -direction. A polarizer (not shown) present at the input of the MZM only admits light polarized along the optic axis. This ensures that there are no unwanted birefringence effects within the MZM. In our feedback loop, we use a polarization controller to align the polarization of the laser light with the polarization admitted by the MZM, thus maximizing the amount of light coupled into the MZM. The refractive index of LiNbO_3 along the optic axis (z -direction) depends on an applied electric field E (along the z -direction) as $n(E) = n_0 - n_0^3 r_{33} E / 2$, where n_0 is the refractive index when there is no applied electric field and r_{33} denotes the linear electro-optic coefficient that determines the strength of the electro-optic effect. We point out that LiNbO_3 is commonly the material of choice for electro-optic MZM construction due to its high electro-optic coefficient and optical transparency in the near-infrared wavelength range (1300-1550 nm) used in telecommunications.

Within an MZM, the applied modulation voltage V sets up an electric field $E = V/D$ across the waveguides through suitably placed electrodes (see Fig. 2.3 (a)). Here D is the separation distance between the electrodes. The electric field causes a change in the refractive indices along the two paths leading to the establishment of a phase difference between the two optical waves. Note that the changes in refractive indices along the two paths are of opposite sign due to the opposing directions of

the applied electric field. Thus for an input light signal of wavelength λ , the phase difference between two paths is given by

$$\Delta\phi = \left(\frac{2\pi}{\lambda}\right) n_0^3 r_{33} \left(\frac{V}{D}\right) L, \quad (2.1)$$

where L is the length of the waveguides. Usually, the lengths of the two waveguides can not be perfectly matched leading to an additional constant phase difference ϕ_0 between the two waves. Thus the total phase difference is given by

$$\Delta\phi = \phi_0 + \left(\frac{2\pi}{\lambda_0}\right) n_0^3 r_{33} \left(\frac{V}{D}\right) L. \quad (2.2)$$

The above equation can be rewritten as

$$\Delta\phi = \phi_0 + \frac{\pi V}{2V_\pi}, \quad (2.3)$$

where $V_\pi \equiv \lambda D / 4n_0^3 r_{33} L$, called the *half-wave voltage*, is the voltage that needs to be applied to produce an additional phase shift of 180 degrees between the two signals. The output optical output of the modulator is then given by the interferometric relationship as

$$P = P_0 \cos^2\left(\frac{\pi V}{2V_\pi} + \phi_0\right) \quad (2.4)$$

where P_0 denotes the input optical power. A picture of a commercially available MZM, similar to the ones used in our experiments (JDSU MZ150, Lucent 2623NA), is shown in Fig. 2.3 (b). The input and output of the modulator are fiber-coupled allowing the laser light to be channeled easily to the MZM. The transmission characteristic, P/P_0 , of the MZMs used in our experiments is measured by recording the output light intensity as the input voltage is varied. The measured transmission

function of JDSU MZ150 is shown in Fig. 2.3 (c). It agrees well with the theoretically predicted $\cos^2(\bullet)$ function. From fitting the data to the theoretically predicted trigonometric relationship, we obtain the half-wave voltage V_π to be 5.6 V. Using a similar process, we measured the half-wave voltage of Lucent 2623NA to be $V_\pi = 3.6$ V. We also note that the phase bias ϕ_0 can be set to a value of choice by applying an appropriate DC voltage in addition to the modulation signal.

2.1.3 Photoreceiver

The optical output from the electro-optic modulator is transduced into an electrical voltage by a photoreceiver. The electrical schematic of the photoreceiver circuit used in our experiments is shown in Fig. 2.4. The photoreceiver circuit consists of a photodiode, a transimpedance amplifier and a variable-gain voltage amplifier. We use a p-i-n type photodiode, with the intrinsic (i in p-i-n) active material being $\text{In}_{0.53}\text{Ga}_{0.47}\text{As}$. This composition of InGaAs has an energy bandgap $E_g = 0.75$ eV [48], which makes it sensitive to a wavelength of 1550 nm. The photodiode is reverse-biased between 0 and 5 V leading to the establishment of an electric field across the intrinsic region. Incident light is absorbed by the reverse-biased photodiode leading to the creation of approximately one electron-hole pair per photon in the intrinsic region. These charge carriers are swept by the electric field to the p-type and n-type regions leading to the production of a photocurrent I_p . The generated photocurrent is proportional to the incident optical power P : $I_p = RP$. The proportionality constant R is called the responsivity of the photodiode. The

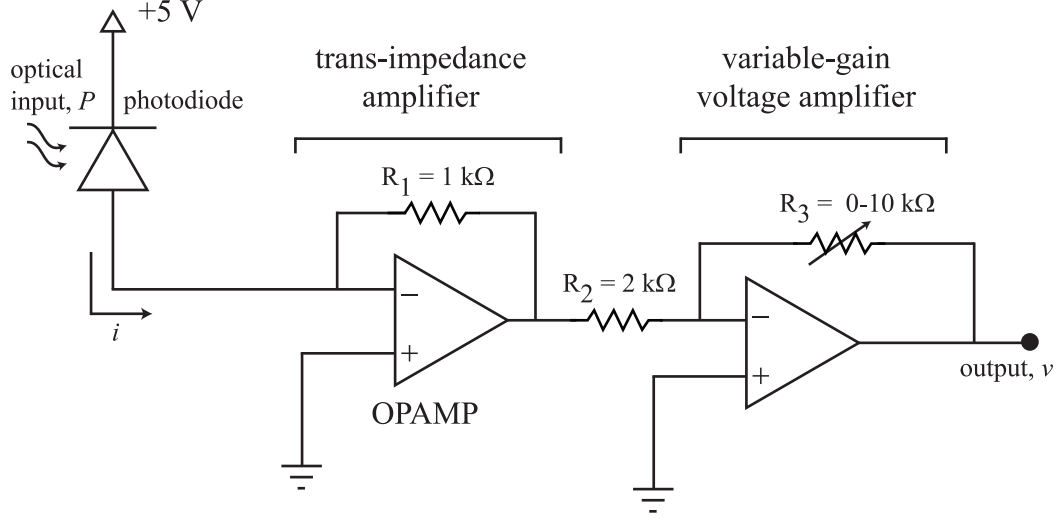


Figure 2.4: Photoreceiver circuit schematic. The photoreceiver consists of a photodiode followed by a trans-impedance amplifier and a variable gain voltage amplifier.

photocurrent is then converted into a voltage using a transimpedance amplifier with gain $G_{\text{TIA}} = R_1 R_3 / R_2$. Thus the output voltage of the photoreceiver is $V_{\text{PR}} = G_{\text{TIA}} R P$. In our experiments, we adjust R_3 such that $R G_{\text{TIA}} = 1 \text{ V/mW}$.

2.1.4 Filtering and Time-delay

The output of the photoreceiver is electronically filtered and time-delayed. As part of the feedback loop, we implement a two-pole bandpass filtering process which can be represented by the transfer function as

$$\hat{H}(s) = \frac{s\tau_H}{(1 + s\tau_L)(1 + s\tau_H)} \quad (2.5)$$

where τ_H and τ_L represent the highpass and lowpass filter time-constants respectively. In the time-domain, the filtering action can be expressed in terms of linear

state-space differential equations and an algebraic equation as

$$\begin{aligned}\frac{d\mathbf{u}}{dt} &= \mathbf{A}\mathbf{u}(t) + \mathbf{B}r(t), \\ w(t) &= \mathbf{C}\mathbf{u}(t) + \mathbf{D}r(t),\end{aligned}\tag{2.6}$$

where $r(t)$ is the input to the filter, $w(t)$ is the output, \mathbf{u} is a vector that represents the state of the filter. \mathbf{A} , \mathbf{B} , \mathbf{C} , and \mathbf{D} are matrices that describe the filter. For a two-pole bandpass filter described by Eqn. 2.5 these matrices are

$$\mathbf{A} = \begin{bmatrix} -\left(\frac{1}{\tau_H} + \frac{1}{\tau_L}\right) & -\frac{1}{\tau_L} \\ \frac{1}{\tau_H} & 0 \end{bmatrix}, \mathbf{B} = \begin{bmatrix} \frac{1}{\tau_L} \\ 0 \end{bmatrix}, \mathbf{C} = \begin{bmatrix} 1 & 0 \end{bmatrix}, \text{ and } \mathbf{D} = 0.\tag{2.7}$$

We note here that the state space representation of a particular system is not unique. There are in fact an infinite number of ways to represent Eqns. 2.6 by manipulating the \mathbf{A} , \mathbf{B} , \mathbf{C} and \mathbf{D} matrices using row operations.

In our experiments, we implement the bandpass filter in discrete-time using a DSP board. Incorporating a DSP board in the feedback loop provides us with the flexibility of programmable filtering and delay. This offers a significant advantage over conventional analog filters especially when studying synchronization. Synchronization requires matched dynamical filter characteristics which are easier to realize using programmable filtering. On the other hand, constructing matched analog filters that are made from discrete electrical elements such as resistors, capacitors and amplifiers is hard to accomplish. Another advantage of digital signal processing is that it allows us to change the parameters of the feedback loop, such as gain and delay, in real-time which is not possible with static components. In Chapter 4 of this thesis, we describe the implementation of an adaptive synchronization algo-

rithm that takes full advantage of the DSP's programmability and computational ability. Fig. 2.5 shows a simplified block diagram of the DSP board used in our experiments (Spectrum Digital DSK6713, DSK6416) identifying its main components. The detailed schematics of the DSP boards can be found in [49, 50]. The DSP board contains two 16-bit analog to digital converters (ADC) which sample the input continuous time signal at regular time intervals. On our DSP boards, the time between samples (referred to as the sampling interval T_s) is set by configuring the sampling rate $F_s \equiv 1/T_s$. The digitized input sequence is manipulated by the signal processor to mimic the bandpass filtering process. The filtered digital signal is finally converted back into an analog signal using one of the two available 16-bit digital to analog converters (DAC) before being output. Our feedback loop is therefore a hybrid discrete/continuous-time system that retains the advantages of optical signal transmission, while exploiting the flexibility of discrete-time signal processing. The DSP boards used in our experiments are designed for audio processing applications and have a maximum sampling rate of $F_s = 96$ kHz. The bandwidth of the signals that can be processed by the DSP board is limited by the Nyquist rate $F_s/2 = 48$ kHz. This represents a hard cut-off of the maximum bandwidth of the dynamics of our optoelectronic oscillator. However, this limitation on the feedback loop bandwidth can be easily be overcome by using field programmable gate array (FPGA) boards that can sample signals at speeds in excess of 1 GSs^{-1} [51]. Alternatively, one can also use high-speed RF bandpass filters and amplifiers to scale the feedback loop to operate at higher speeds [25, 45].

The digital filter implemented in our experiments can be described by a discrete-

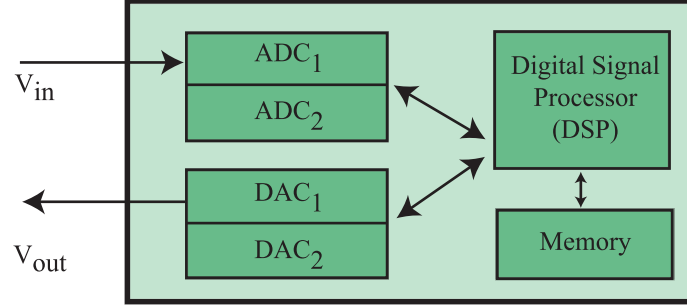


Figure 2.5: Simplified block diagram of a DSP board. The DSP contains an analog to digital converter (ADC) that samples an incoming analog signal at regular intervals. The sampled data is then processed by a digital signal processor (DSP). The processed digital signal is then converted back into an analog signal by a digital to analog converter (DAC).

time transfer function $\hat{H}(z)$ which is obtained from the continuous-time transfer function $\hat{H}(s)$ by applying a bilinear transform with frequency pre-warping [52]. Frequency pre-warping ensures that various analog frequency features (such as filter corner frequencies) are accurately transformed from the continuous domain to the discrete domain. Carrying out the bilinear transform produces

$$\hat{H}(z) = \frac{1}{4}(1 - z_L)(1 + z_H) \frac{(z^2 - 1)}{(z - z_L)(z - z_H)}, \quad (2.8)$$

where z_L and z_H are the poles of the discrete-time filter given as

$$z_H = \frac{1 - \tan\left(\frac{T_s}{2\tau_H}\right)}{1 + \tan\left(\frac{T_s}{2\tau_H}\right)} \text{ and } z_L = \frac{1 - \tan\left(\frac{T_s}{2\tau_L}\right)}{1 + \tan\left(\frac{T_s}{2\tau_L}\right)}. \quad (2.9)$$

Analogous to the continuous time equations, the discrete-time filter equations can be represented in the time domain as state-space difference equations shown below.

$$\begin{aligned} \mathbf{u}[n + 1] &= \mathbf{A}\mathbf{u}[n] + \mathbf{B}r[n], \\ w[n] &= \mathbf{C}\mathbf{u}[n] + \mathbf{D}r[n]. \end{aligned} \quad (2.10)$$

Here $r[n]$ represents the discrete-time input to the digital filter, $w[n]$ is the output, and \mathbf{u} is a 2-dimensional state vector. The matrices \mathbf{A} , \mathbf{B} , \mathbf{C} , and \mathbf{D} describe the filter and are given as

$$\mathbf{A} = \begin{bmatrix} -(z_L + z_H) & -z_L \\ z_H & 0 \end{bmatrix}, \quad \mathbf{B} = \begin{bmatrix} z_L \\ 0 \end{bmatrix}, \quad (2.11)$$

$$\mathbf{C} = \begin{bmatrix} 0 & -\frac{(1-z_L)(1+z_H)(1+z_L z_H)}{4z_L z_H} \end{bmatrix}, \quad \text{and } \mathbf{D} = \frac{1}{4}(1 - z_L)(1 + z_H).$$

We note that the discrete-time filter matrices \mathbf{A} , \mathbf{B} , \mathbf{C} , and \mathbf{D} shown above are not the same as the filter matrices for the continuous-time case (Eqn. 2.7). The pair of first-order state space difference equations (Eqn. 2.10) can be combined into a single second-order iterative difference equation that is more suited for numerical iteration. We use the transfer function $\hat{H}(z)$ to derive this alternative time-domain representation. In the z -transform domain, the input-output relationship can be expressed as

$$\hat{W}(z) = \hat{H}(z)\hat{R}(z) \quad (2.12)$$

where $\hat{W}(z)$ and $\hat{R}(z)$ represent the z -transforms of the output and the input signals respectively. Substituting the form of $\hat{H}(z)$ and expanding, we obtain

$$\begin{aligned} \hat{W}(z) &= (z_L + z_H)z^{-1}\hat{W}(z) - z_L z_H z^{-2}\hat{W}(z) \\ &+ (1 - z^{-2})\frac{(1 - z_L)(1 + z_H)}{4}\hat{R}(z). \end{aligned} \quad (2.13)$$

Now, taking the inverse z -transform gives the time-domain equation

$$w[n] = b_0 r[n] + b_2 r[n - 2] - a_1 w[n - 1] - a_2 w[n - 2], \quad (2.14)$$

The coefficients b_0 , a_2 , b_1 , and a_1 describe the filter and are given as

$$b_0 = \frac{(1 - z_L)(1 + z_H)}{4}, \quad b_2 = -\frac{(1 - z_L)(1 + z_H)}{4}, \quad (2.15)$$

$$a_1 = -(z_L + z_H), \quad \text{and} \quad a_2 = z_L z_H.$$

For a bandpass filter with a highpass filter cut-on frequency of 100 Hz and a lowpass filter cut-off frequency of 10 kHz and sampling rate $F_s = 96$ kHz, the filter coefficients can be calculated to be $a_1 = -1.4939$, $a_2 = 0.4972$, $b_0 = 0.2514$, and $b_2 = -0.2514$. Fig. 2.6 shows the measured amplitude response (shown in red) of this filter implemented using the DSP board. The theoretically predicted response (in blue) is also shown for comparison. The measured response faithfully follows the theoretically predicted characteristics, except at low frequencies. The additional attenuation seen at low frequencies in the experiments is attributed to the presence of a DC-blocking capacitor on the DSP board.

In our experiments, the DSP board is also used to implement a time-delay. Conventional analog electrical time-delays use either coaxial cables or a series of LC delay units. LC delay lines generally introduce additional frequency dependence that is undesirable. On the other hand, implementation of a cable time-delay of the order of a few milli-seconds requires an impractically long cable and can be very lossy. DSP systems overcome both these problems and can produce a lossless and frequency independent time delay that is readily adjustable. Using the DSP board, we implement the time-delay as shown in Fig. 2.7. The discrete-time samples from the ADC are collected in an indexed memory buffer of length k . At each sampling instant, the stored samples are moved down the buffer by one unit and

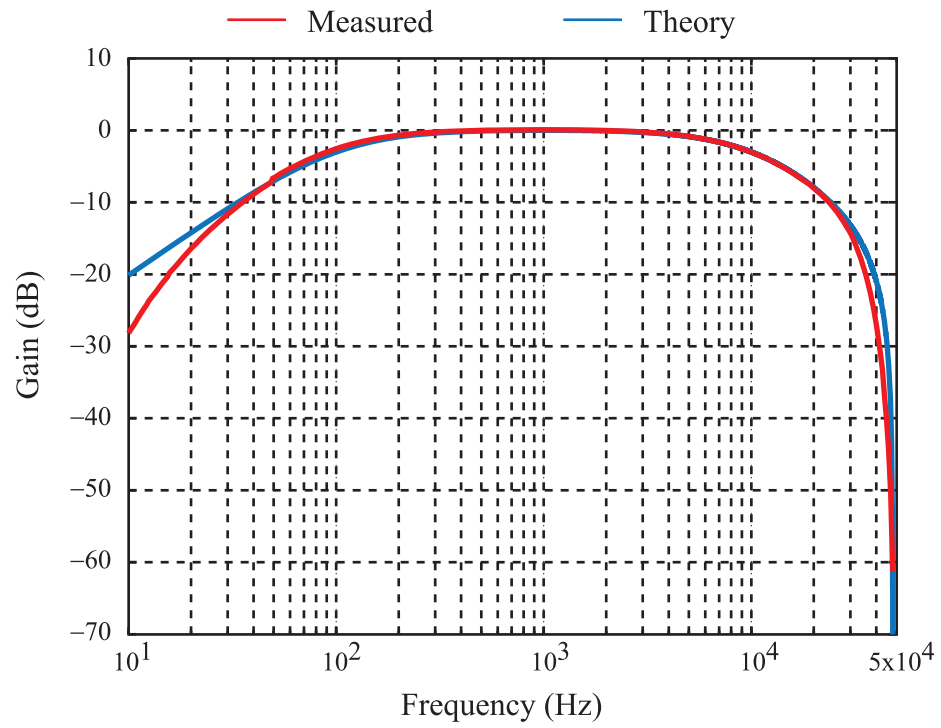


Figure 2.6: Measured amplitude response of the digital filter. The experimentally measured response is shown in red and the theoretically predicted behavior is shown in blue.

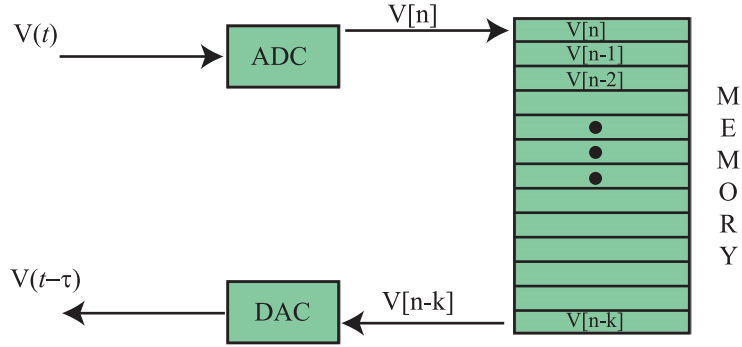


Figure 2.7: Implementation of a time-delay using the DSP board. The digital samples are stored in a memory buffer (of k units) before being output by the DAC. At each time-step the values in the buffer are advanced by one unit, thus producing a delay $\tau = k/F_s$.

simultaneously the value in the k^{th} unit is output through the DAC. This process produces a time-delay equal to k sampling intervals or $\tau = k/F_s$ seconds. Thus by configuring the length of the memory buffer a desired delay τ can be set.

2.1.5 Voltage Amplifier

The filtered and time-delayed output signal from the DSP board is amplified by a voltage amplifier before being fed back into modulator. In our experiments, we use an operational amplifier (LM741) based circuit to produce a voltage gain $G_{VA} \approx -20$. The circuit diagram of the amplifier circuit used in our experiments is shown in Fig. 2.8. The circuit consists of an buffer stage and a gain stage. The buffer stage presents a high input impedance ($R_{in} = 10 \text{ k}\Omega$) which ensures that the DSP board outputs do not need to provide high current. The gain state produces the amplification of the signal. In addition to amplifying the signal, the gain state also adds an adjustable DC voltage to the output allowing us to control the operating

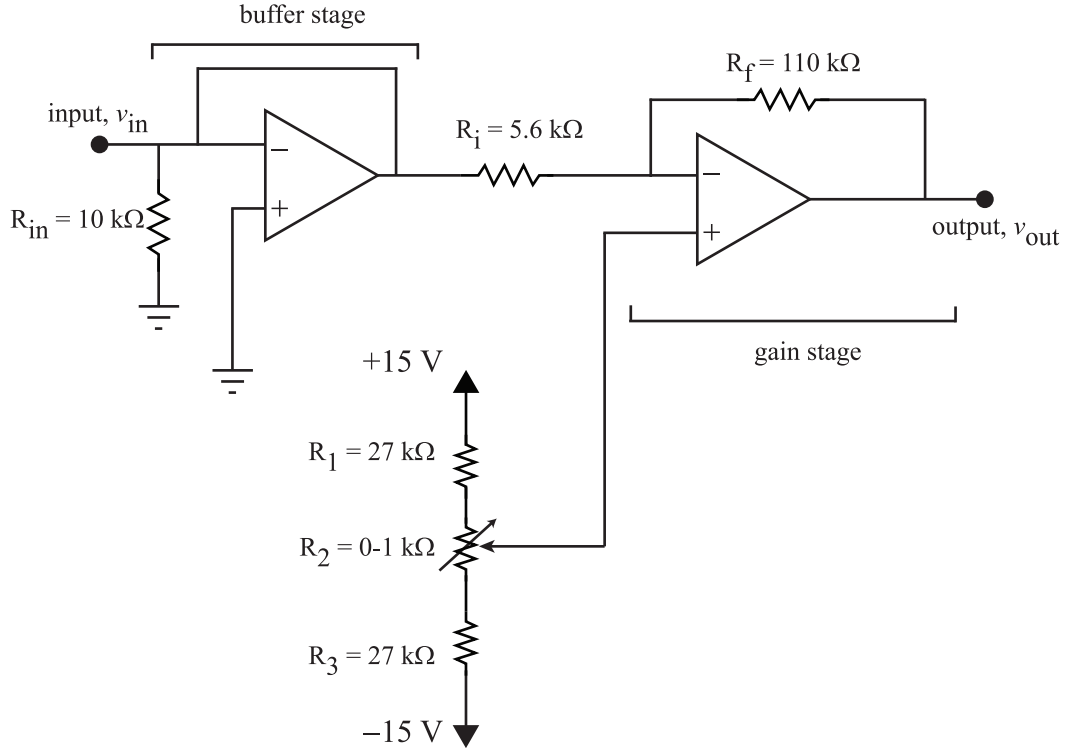


Figure 2.8: Circuit schematic of the amplifier used in the feedback loop.

point ϕ_0 of the modulator. For the resistor values chosen, the offset DC voltage can approximately range from -5 V to $+5\text{ V}$ which spans roughly two times the half-wave voltage of our modulators.

2.2 Mathematical Modeling

In this section, we develop the mathematical model that describes the dynamics of the optoelectronic feedback loop. We develop our model based on the characteristics of the various constituent components presented in the previous section. We express the dynamical equations in continuous-time as a set of delay-differential equations and in discrete-time as a recursive map equation. We consider

the continuous-time case first. The optical output of the MZM, as discussed in the previous section, is given as

$$P(t) = P_0 \cos^2 \left(\frac{\pi V(t)}{2V_\pi} + \phi_0 \right) \quad (2.16)$$

where P_0 is the steady optical output of the laser diode and $V(t)$ is the input electrical modulation voltage. The output of the MZM is transduced into an electric voltage by the photoreceiver whose response is $G_{\text{TIA}}R$. Thus the electrical output of the photo-detector is given as

$$G_{\text{TIA}}RP(t) = G_{\text{TIA}}RP_0 \cos^2 \left(\frac{\pi V(t)}{2V_\pi} + \phi_0 \right). \quad (2.17)$$

Next we consider the effect of the amplifier and time-delay. Even though, in our experiments, the amplification process occurs after the filtering, it is convenient for the purposes of analysis to commute it with the filter. This commutation is justified as the filtering and the amplification are both linear processes. Assuming a voltage gain of G_{VA} from the amplifier and a time-delay τ , we can write the input to the filter as

$$r(t) = G_{\text{VA}}G_{\text{TIA}}RP_0 \cos^2 \left(\frac{\pi V(t - \tau)}{2V_\pi} + \phi_0 \right). \quad (2.18)$$

We then use the time-domain state-space equations for the bandpass filter to write the dynamical equation describing the feedback loop. Substituting the above form of the input signal in Eqn. 2.6, we obtain

$$\begin{aligned} \frac{d\mathbf{u}}{dt} &= \mathbf{A}\mathbf{u}(t) + \mathbf{B}G_{\text{VA}}G_{\text{TIA}}RP_0 \cos^2 \left(\frac{\pi V(t - \tau)}{2V_\pi} + \phi_0 \right), \\ V(t) &= \mathbf{C}\mathbf{u}(t). \end{aligned} \quad (2.19)$$

Here, we make use of the facts that $\mathbf{D} = 0$ and that the output of the filter $w(t)$ is the same as the modulation voltage $V(t)$ input to the MZM . The above equations can be rewritten in a compact form as

$$\frac{d\mathbf{u}}{dt} = \mathbf{A}\mathbf{u}(t) + \mathbf{B}G_{\text{VA}}G_{\text{TIA}}RP_0 \cos^2 \left(\frac{\pi\mathbf{C}\mathbf{u}(t-\tau)}{2V_\pi} + \phi_0 \right). \quad (2.20)$$

To express the above state-space equation in terms of physical voltages, we choose the state vector \mathbf{u} to be

$$\mathbf{u}(t) = \begin{bmatrix} V(t) \\ \frac{1}{\tau_H} \int_{-\infty}^t V(t') dt' \end{bmatrix}, \quad (2.21)$$

and substitute the values for \mathbf{A} , \mathbf{B} and \mathbf{C} from Eqn. 2.7. This gives us

$$\begin{aligned} \tau_L \frac{dV}{dt} = & - \left(1 + \frac{\tau_L}{\tau_H} \right) V(t) - \frac{1}{\tau_H} \int_{-\infty}^t V(t') dt' \\ & + P_0RG \cos^2 \left(\frac{\pi V(t-\tau)}{2V_\pi} + \phi_0 \right), \\ \frac{d}{dt} \int_{-\infty}^t V(t') dt' = & V(t). \end{aligned} \quad (2.22)$$

To simplify the above equations, we define the following dimensionless quantities.

$$x(t) \equiv \frac{\pi V(t)}{2V_\pi}, \quad y(t) \equiv \frac{1}{\tau_H} \int_{-\infty}^t x(t') dt', \quad \text{and} \quad \beta \equiv \frac{\pi G_{\text{VA}}G_{\text{TIA}}RP_0}{2V_\pi}. \quad (2.23)$$

The quantity $x(t)$ denotes the normalized input voltage to the MZM and is the observed dynamical variable in our experiments. The quantity β , which incorporates the various proportionality factors in the feedback loop, denotes the total round-trip gain. It is an important parameter which, along with the time-delay, bias-point and filter constants, determines the dynamics of the feedback loop. The block diagram

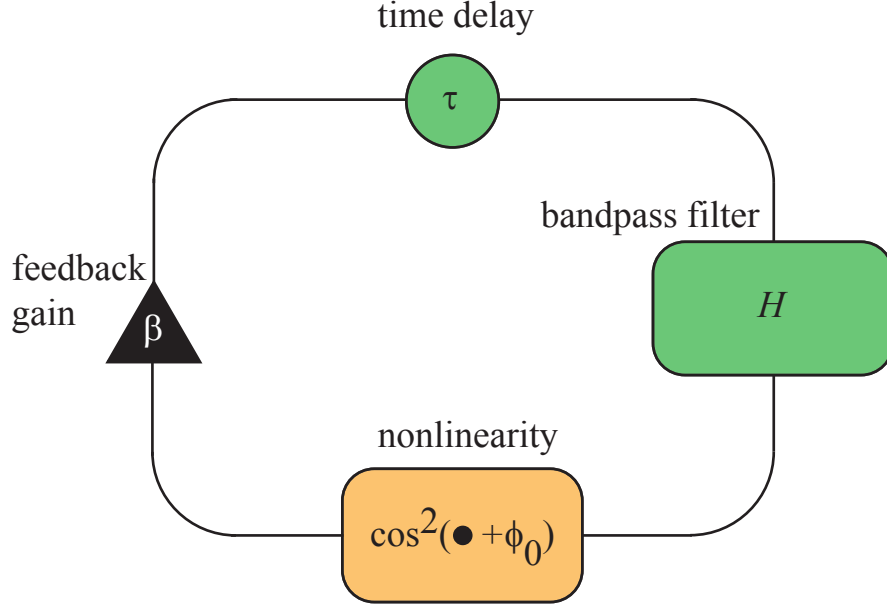


Figure 2.9: Mathematical block diagram of the optoelectronic feedback loop.

shown in Fig. 2.9 presents a simplified mathematical picture of the optoelectronic feedback loop in continuous time. The delay-differential equations derived above can now be re-expressed as dimensionless equations that describe the dynamics of the optoelectronic oscillator. These equations are presented below.

$$\begin{aligned}\tau_L \frac{dx}{dt} &= - \left(1 + \frac{\tau_L}{\tau_H} \right) x(t) - \frac{1}{\tau_H} y(t) + \beta \cos^2 [x(t - \tau) + \phi_0], \\ \tau_H \frac{dy}{dt} &= x(t).\end{aligned}\tag{2.24}$$

To develop the discrete-time model for the feedback loop, we follow the same process as detailed above. The input signal to the digital filter can be expressed in terms of dimensionless feedback strength β and modulation voltage x as

$$r[n] = \beta \cos^2 (x[n - k] + \phi_0)\tag{2.25}$$

where k is the discrete-time feedback delay in terms of sample intervals. As evident

from the above equation, the input to the filter is a nonlinearly transformed, time-delayed version of the output signal. Using the iterative equation representing the digital-filter (Eqn. 2.14), the map equation describing the feedback loop dynamics can be written as

$$\begin{aligned}
 x[n] = & b_0\beta \cos^2(x[n-k] + \phi_0) + b_2\beta \cos^2(x[n-k-2] + \phi_0) \quad (2.26) \\
 & - a_1x[n-1] - a_2x[n-2].
 \end{aligned}$$

2.3 Dynamical Behavior of the Feedback Loop

In this section, we discuss the dynamical behavior of the optoelectronic feedback loop. We present experimentally measured time traces showing the wide variety of dynamical behavior that can be exhibited by the system. We supplement the experimental measurements with results obtained from numerical simulations of the dynamical equations developed in the previous section.

In our experiments, the phase-bias ϕ_0 of the MZM is set to $-\pi/4$, which corresponds to the half-transmission point of the modulator. At this bias-point, the steady-state solution of the system is most linearly unstable [53]. In other words, at this operating point, the feedback loop has the greatest tendency towards oscillatory dynamics. There are examples in the literature which consider the dynamics of similar optoelectronic feedback loops set at other operating points [45]. For the measurements presented here, the bandwidth of the filter is set to range from $f_H = 1/(2\pi\tau_H) = 100$ Hz to $f_L = 1/(2\pi\tau_L) = 10$ kHz while the sampling rate of the ADC is set to 96 kS s^{-1} . We hold the delay constant at $k = 22$ time-steps. At a sampling

rate of $F_s = 96$ kHz, this corresponds to a time delay of $230 \mu\text{s}$.

We examine the behavior of the feedback loop as the round-trip gain β is varied. We accomplish a fine control of β by programming a scaling factor in the DSP board. The maximum achievable value of the round-trip gain is determined by the steady laser input power P_0 . For the set of measurements shown in this section, P_0 was set to produce a maximum β of 5.0. We can experimentally measure the feedback gain in an open-loop configuration by introducing a small-amplitude modulation signal into the MZM biased at $\phi_0 = \pi/4$. At this bias-point, the system behaves linearly for a small-amplitude signal and thus the ratio of the output amplitude to the input amplitude gives a measure of β . Using a network analyzer (Agilent 4395A), we measure the feedback gain as a function of the modulation frequency for a given DSP scale factor. The network analyzer outputs a swept-frequency sinusoidal signal which is used as a stimulus to the open-loop system. The amplitude of the corresponding output signal is then analyzed as a function of frequency to obtain the gain characteristics of the open-loop system. This measurement is presented in Fig. 2.10. The open-loop gain measurement follows the bandpass filter characteristic with 3 dB points at 100 Hz and 10 kHz as expected. The value of β is given by the open-loop gain at the center frequency of the filter pass-band, indicated by the dashed line in Fig. 2.10.

The dynamical behavior of the feedback loop $x(t)$ for three different values of β is shown in Fig. 2.11. The experimental measurements are reported in panel (a) while panel (b) shows the results from numerical simulations of the discrete-time difference equations (Eqn. 2.26) developed in the previous section. For a low feedback

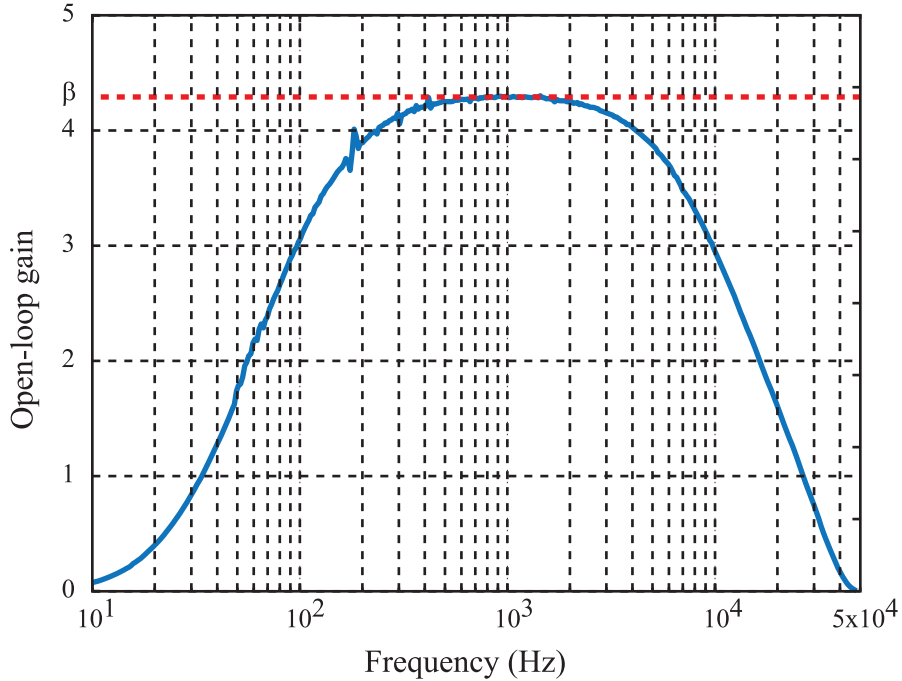


Figure 2.10: Measurement of the feedback gain β .

strength $\beta = 1.5$, the amplitude of the MZM modulation signal is small. Consequently, nonlinear effects from the MZM are not very strong. In this regime, the system exhibits periodic behavior. As the feedback strength is increased, nonlinear effects from the MZM become stronger and the dynamical complexity increases. For $\beta = 3.0$, the system executes aperiodic motion, but still with strong periodic signatures. As β is increased further, the system exhibits robust chaos. Here, “robust” means that the system remains in the chaotic state over a wide range of parameters.

In Fig. 2.12, we show the experimentally measured and numerically calculated bifurcation diagrams which characterize the behavior of the optoelectronic feedback loop as a control parameter (in this case β) is varied. The process used to obtain

the bifurcation diagram is as follows: At each value of the control parameter, a long time trace capturing the dynamical nature of the system is obtained. The amplitude histogram of this time trace can be interpreted as being proportional to the probability with which the system takes any given amplitude value. The bifurcation diagram is formed by horizontally stacking these probability histograms (shown in gray scale with black corresponding to zero) as the control parameter is varied. For $\beta < 1$ it can be seen from the bifurcation diagram that the system is almost always found in the steady state $x = 0$. As β is increased, the system undergoes a series of bifurcations and displays increasingly complicated behavior ranging from periodic oscillations (characterized by two highly probable amplitude values) to robustly chaotic dynamics (characterized by all amplitude values being equally probable).

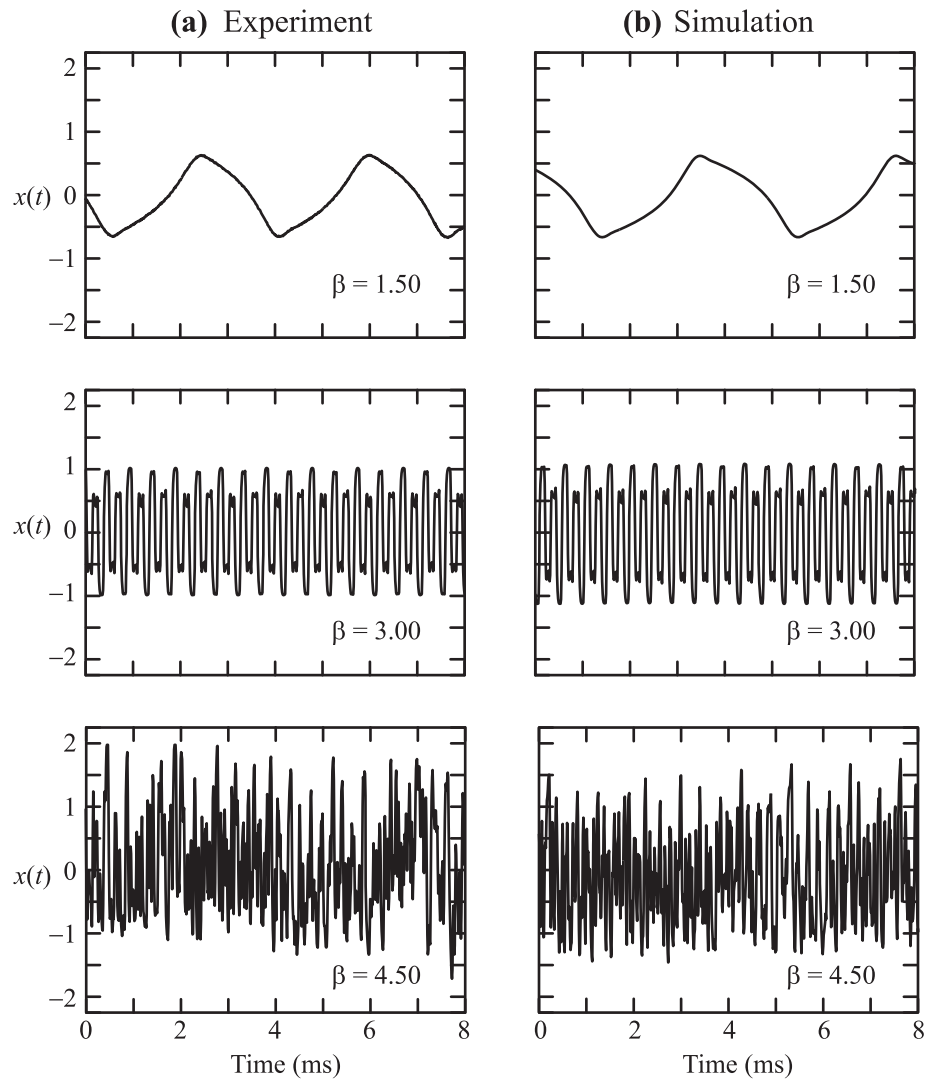


Figure 2.11: Dynamical behavior of the optoelectronic feedback loop. The dynamics of the oscillator system increase in complexity as the round-trip gain β is increased. (a) Experimentally measured data. (b) Data from numerical simulations.

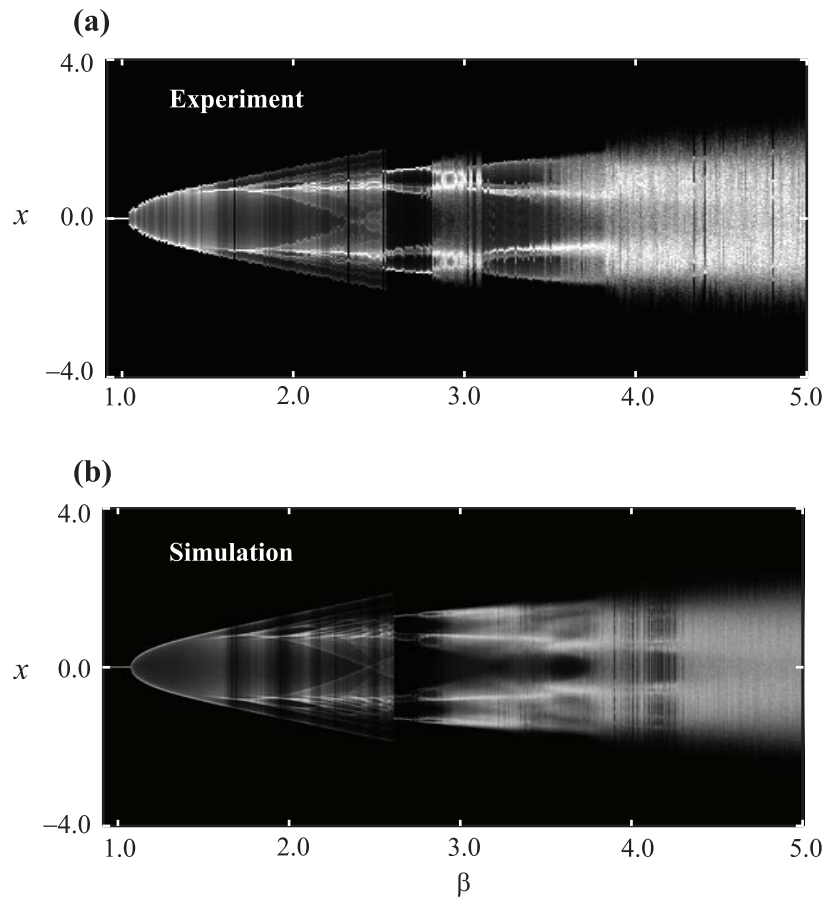


Figure 2.12: Experimentally measured and numerically calculated bifurcation diagrams for the optoelectronic feedback loop with β as the control parameter. (a) Experiment and (b) simulation.

Chapter 3

Coupled Optoelectronic Feedback Oscillators

The trajectories of two identical chaotic systems that begin from slightly different initial conditions quickly diverge and become uncorrelated even though each system describes the same attractor in phase space. In the face of this extreme sensitivity to small perturbations, it is surprising that two chaotic systems can be driven to execute coordinated motion, with each system behaving identically as the other at every instant of time. This phenomenon of synchronization is realized by coupling the two systems, or in other words, by allowing a flow of information between them. In this chapter we discuss the coupling of the optoelectronic feedback loops described in the previous chapter and present experimental measurements demonstrating synchronization.

We begin, in Sec. 3.1, by developing the coupled equations that describe a general network of optoelectronic oscillators. The connection topology in the network is represented mathematically in the form of a coupling matrix. We discuss two different coupling scenarios. The first case, called injective coupling, describes the situation where the coupling term from node j to node i is a function of the state of node j alone. The second case, termed diffusive coupling, depicts the situation where the coupling term is a function of the difference of the states of both oscillators.

In Sec. 3.2, we present the details of the experimental implementation of a simple network of two optoelectronic feedback loops. We report measurements of synchronized behavior and identify parameter regimes for which synchronization is observed. In this section, we also discuss the transient behavior to synchronization and present measurements of the convergence rate to synchronization.

In Sec. 3.3, we describe a theoretical technique that is widely used to analyze the stability of the synchronous solution. This approach, called master stability analysis [33], predicts if a given network of dynamical oscillators exhibits stable synchronous behavior based on the eigenvalues of the coupling matrix.

Sec. 3.4 provides a brief summary of the chapter.

3.1 Mathematical Formulation

Consider N independent identical optoelectronic oscillators where the dynamics of the i^{th} oscillator is governed by the continuous-time differential equation

$$\begin{aligned} \frac{d\mathbf{u}_i}{dt} &= \mathbf{A}\mathbf{u}_i(t) + \mathbf{B}\beta \cos^2(x_i(t - \tau) + \phi_0), \\ x_i(t) &= w_i(t) = \mathbf{C}\mathbf{u}_i(t). \end{aligned} \tag{3.1}$$

where \mathbf{A} , \mathbf{B} , and \mathbf{C} are given in Eqn. 2.7, and $\mathbf{u}_i(t)$ is the state vector of the i^{th} oscillator normalized by the factor $\pi/(2V_\pi)$. The quantity $x_i(t)$ denotes the normalized voltage input to the modulator and is equal, for uncoupled oscillators, to the filter output $w_i(t)$. Eqn. 3.1 is a dimensionless version of Eqn. 2.19.

In a network configuration, the oscillators are coupled by combining the filter

outputs of the network nodes to form the input voltage to the modulator. The equations for the i^{th} oscillator in the network can then be written as

$$\begin{aligned}\frac{d\mathbf{u}_i}{dt} &= \mathbf{A}\mathbf{u}_i(t) + \mathbf{B}\beta \cos^2(x_i(t - \tau) + \phi_0), \\ w_i(t) &= \mathbf{C}\mathbf{u}_i(t), \\ x_i(t) &= w_i(t) + \sum_{j \neq i} K_{ij} w_j(t),\end{aligned}\tag{3.2}$$

where the quantity K_{ij} denotes the strength of the coupling from node j to node i . Further, setting $K_{ii} = 1$, which represent the self-feedback strengths, allows us to write the net feedback term at node i as $x_i(t) = \sum_{j=1}^N K_{ij} w_j(t)$. Thus, the topology of the network can be represented by the coupling matrix \mathbf{K} , which has as its elements, the interaction strengths of all links. The above coupling equations describe the case of *injective coupling* where the coupling term depends only on the states of other oscillators of the network. Eqn. 3.2 admits a synchronous solution if, and only if, the total external coupling into each node, $\sum_{j=1}^N K_{ij}$ is the same for all nodes i . In other words, a necessary condition for the existence of a global synchronous solution $x_1(t) = x_2(t) = \dots = x_N(t) = x_s(t)$ is that the row-sum of the coupling matrix \mathbf{K} be uniform. The synchronous solution then follows the equation

$$\begin{aligned}\frac{d\mathbf{u}_s}{dt} &= \mathbf{A}\mathbf{u}_s(t) + \mathbf{B}\beta \cos^2(x_s(t - \tau) + \phi_0), \\ x_s(t) &= \left(\sum_{j=1}^N K_{ij} \right) w_s(t) = \left(\sum_{j=1}^N K_{ij} \right) \mathbf{C}\mathbf{u}_s(t).\end{aligned}\tag{3.3}$$

Another method of coupling extensively used to model network interactions is called *diffusive coupling*. In this scheme, the coupling term into node i comprises the sum of the differences of the states of the oscillators $w_j - w_i$. The equations for

a network of diffusively-coupled optoelectronic oscillators are given by

$$\begin{aligned}
\frac{d\mathbf{u}_i}{dt} &= \mathbf{A}\mathbf{u}_i(t) + \mathbf{B}\beta \cos^2(x_i(t - \tau) + \phi_0), \\
w_i(t) &= \mathbf{C}\mathbf{u}_i(t), \\
x_i(t) &= w_i(t) + \sum_{j \neq i} K_{ij} (w_j(t) - w_i(t)).
\end{aligned} \tag{3.4}$$

The coupling matrix that represents the topology of a network of diffusively-coupled oscillators is called the Laplacian matrix (denoted as \mathbf{L}). The off-diagonal elements of the Laplacian matrix L_{ij} ($i \neq j$) are the same as the off-diagonal elements of the matrix \mathbf{K} and denote the strength of coupling from node j to node i . However, the diagonal elements L_{ii} are equal to the negative of the total coupling strength into each node i . Eqn. 3.4 can be expressed in terms of the Laplacian matrix elements as

$$\begin{aligned}
\frac{d\mathbf{u}_i}{dt} &= \mathbf{A}\mathbf{u}_i(t) + \mathbf{B}\beta \cos^2(x_i(t - \tau) + \phi_0), \\
w_i(t) &= \mathbf{C}\mathbf{u}_i(t), \\
x_i(t) &= w_i(t) + \sum_{j=1}^N L_{ij} w_j(t).
\end{aligned} \tag{3.5}$$

We note that, by construction, the row-sums of the Laplacian matrix are all uniform and equal to zero. Thus, the above equations automatically admit a synchronous solution whose evolution follows the equations for an uncoupled oscillator. For this reason, diffusive coupling has been the preferred form of coupling in many studies related to network synchronization [33, 54].

3.2 Synchronization of Coupled Oscillators: Experiments

In this section, we describe the implementation of a network of two nominally identical coupled optoelectronic oscillators. The nodes in our experimental network can be coupled either optically or electrically. For optical coupling, the output of the electro-optic modulator of each oscillator is split into two parts and fed back into both systems. The most general optical coupling scenario is shown as a block diagram in Fig. 3.1 (a). The self-feedback coupling strengths of the two nodes are described by the constants K_{11} and K_{22} and the delays are denoted as τ_{11} and τ_{22} . The cross-coupling strengths are given by K_{21} (node 1 to node 2) and K_{12} (node 2 to node 1) and the corresponding delays are τ_{21} and τ_{12} . To implement the coupling electrically, the outputs of the filters are combined and fed back to serve as the modulation voltages. This situation is portrayed as a block diagram in Fig. 3.1 (b). Here, we note that the filtering, time-delay, and coupling are all linear operations and thus can be exchanged with each other without affecting the dynamics. We point out that in Fig. 3.1 (b), by commuting the filter block with the coupling strength and delay, we retrieve the situation described in Fig. 3.1 (a). Both the implementations of coupling, optical and electrical, thus lead to the same behavior. We couple the oscillators optically in our experiments except when specified otherwise. The mathematical equivalence of the two forms of coupling allows us to exploit the practical advantages of optical coupling even though the analysis, for convenience, is performed using the equations with coupled electrical voltages.

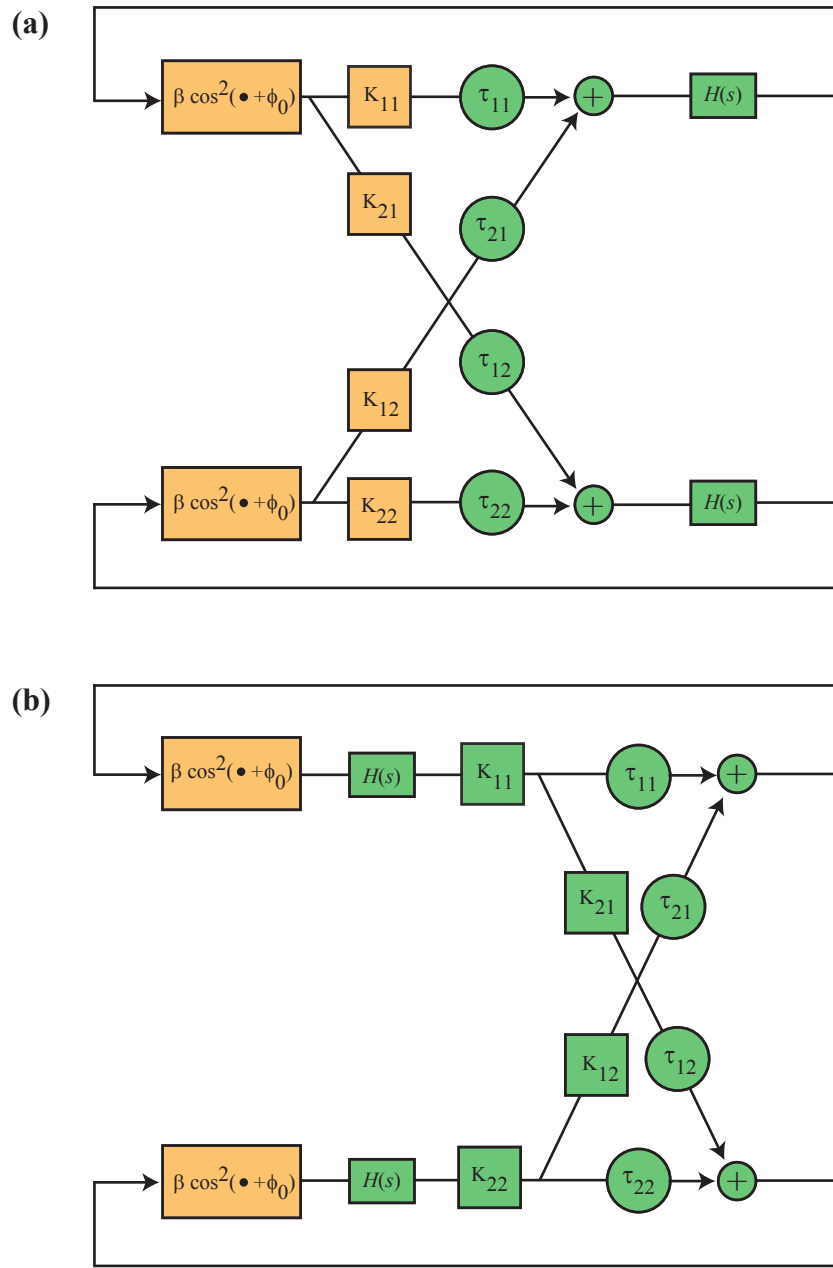


Figure 3.1: Block diagram illustration of the coupling of two optoelectronic oscillators as implemented (a) optically and (b) electrically.

For a two node system, the coupled dynamical equations can be represented in terms of the general coupling parameters as

$$\begin{aligned}\frac{d\mathbf{u}_1}{dt} &= \mathbf{A}\mathbf{u}_1(t) + \mathbf{B}\beta \cos^2(\mathbf{C} [K_{11}\mathbf{u}_1(t - \tau_{11}) + K_{12}\mathbf{u}_2(t - \tau_{12})] + \phi_0), \\ \frac{d\mathbf{u}_2}{dt} &= \mathbf{A}\mathbf{u}_2(t) + \mathbf{B}\beta \cos^2(\mathbf{C} [K_{22}\mathbf{u}_2(t - \tau_{22}) + K_{21}\mathbf{u}_1(t - \tau_{21})] + \phi_0).\end{aligned}\quad (3.6)$$

The necessary conditions for the above equations to permit an isochronal synchronous solution are derived in Ref. [55] and are reproduced below as

$$\begin{aligned}K_{11} + K_{12} &= K_{22} + K_{21}, \\ \tau_{11} = \tau_{12} = \tau_{22} = \tau_{21} &= \tau.\end{aligned}\quad (3.7)$$

Further, restricting our attention to cases when the synchronous solution follows the dynamics of an independent feedback loop imposes the additional constraint $K_{11} + K_{12} = K_{22} + K_{21} = 1$. The equations describing the two oscillators then become

$$\begin{aligned}\frac{d\mathbf{u}_1}{dt} &= \mathbf{A}\mathbf{u}_1(t) + \mathbf{B}\beta \cos^2(\mathbf{C} [(1 - K_{12})\mathbf{u}_1(t - \tau) + K_{12}\mathbf{u}_2(t - \tau)] + \phi_0), \\ \frac{d\mathbf{u}_2}{dt} &= \mathbf{A}\mathbf{u}_2(t) + \mathbf{B}\beta \cos^2(\mathbf{C} [(1 - K_{21})\mathbf{u}_2(t - \tau) + K_{21}\mathbf{u}_1(t - \tau)] + \phi_0).\end{aligned}\quad (3.8)$$

The above equations can be recognized to be of the form of the diffusively coupled equations shown in Eqn. 3.4.

In our experiments, we consider the symmetric coupling case, $K_{12} = K_{21} = \kappa$.

This situation is described by the equations

$$\begin{aligned}\frac{d\mathbf{u}_1}{dt} &= \mathbf{A}\mathbf{u}_1(t) + \mathbf{B}\beta \cos^2(\mathbf{C} [(1 - \kappa)\mathbf{u}_1(t - \tau) + \kappa\mathbf{u}_2(t - \tau)] + \phi_0), \\ \frac{d\mathbf{u}_2}{dt} &= \mathbf{A}\mathbf{u}_2(t) + \mathbf{B}\beta \cos^2(\mathbf{C} [(1 - \kappa)\mathbf{u}_2(t - \tau) + \kappa\mathbf{u}_1(t - \tau)] + \phi_0).\end{aligned}\quad (3.9)$$

We point out here that even though the above equations admit a synchronous solution, its stability is not guaranteed for all κ . Synchrony may only be observed for a range of κ for which the synchronous solution is stable. In Sec. 3.3, we introduce a theoretical technique to analyze the stability of the synchronous solution in terms of the properties of the coupling matrix. In what follows here, we present experimental observations that identify the range of κ for which the synchronous solution is stable. For the measurements shown here, we performed the coupling electrically using the DSP boards. Our DSP boards (Spectrum Digital DSK6416) have two on-board ADCs and DACs. We utilize an ADC and DAC pair to independently implement the digital filtering and time-delay for each optoelectronic oscillator. The coupling terms for the two nodes are constructed by suitably combining the outputs of the digital filters from the two systems. These combination signals are subsequently converted into analog voltages by the DACs and fed to the MZMs as modulation signals. As part of our measurements, we record at each node i ($=1, 2$), the normalized voltage input to the modulator $x(t)$ (as defined in Eqn. 3.4) using an 8-bit digital oscilloscope (Tektronix TDS7104). The parameters of the two loops are adjusted to be nominally identical and equal to $\beta = 6.0$, $\tau = 230 \mu\text{s}$ and $\phi_0 = -\pi/4$. The sampling rate of the ADC is set to 96 kHz and the filter band is set to range from $f_H = 100 \text{ Hz}$ to $f_L = 10 \text{ kHz}$. In Figs. 3.2 (a) and (b), we show the recorded time-traces for two values of coupling strengths $\kappa = 0.125$ and $\kappa = 0.375$ respectively. When $\kappa = 0.125$, the two-node network does not exhibit synchronized behavior (Fig. 3.2 (a)). However, for a higher coupling strength, $\kappa = 0.375$, the coupled feedback loops exhibit stable synchronous behavior as shown in Fig. 3.2 (b). Figs. 3.2 (c) and (d) show

the synchronization plots for these two cases. While for the lower coupling strength case the dynamics of the two oscillators are weakly correlated, they are identically synchronized for $\kappa = 0.375$.

We now investigate the range of coupling strength over which the network exhibits synchronous behavior. To this end, we measure a normalized synchronization error

$$\theta = \left(\frac{\langle (x_1(t) - x_2(t))^2 \rangle}{\langle x_1^2(t) + x_2^2(t) \rangle} \right)^{1/2} \quad (3.10)$$

as the coupling strength κ is varied. Here, $\langle \bullet \rangle$ denotes an average over the time for which $x_1(t)$ and $x_2(t)$ are measured (which is much longer than the dynamical time-scale). The normalized synchronization error θ takes a value of zero when the two oscillators are isochronally synchronized and a value of one when the dynamics are uncorrelated but identically distributed. We point out that for the case when the symmetric coupling strength $\kappa = 0.5$, the two oscillators are guaranteed to synchronize as the modulation signals in both oscillators are trivially equal (see Eqn. 3.9). In fact, in Ref. [55], it is shown that the synchronization of the two oscillators is guaranteed to be stable whenever $K_{12} + K_{21} = 1$. In Fig. 3.3, we show the measurements and simulations of θ as a function of κ . The range of κ over which the two oscillators synchronize is observed to be approximately symmetric about the trivial case $\kappa = 0.5$. The disparity between the experimental and numerical results is caused due to the non-identity of the two constituent nodes which is unavoidable in experiments. The non-identity of the oscillators, along with noise and measurement quantization, causes the minimum experimentally attainable level

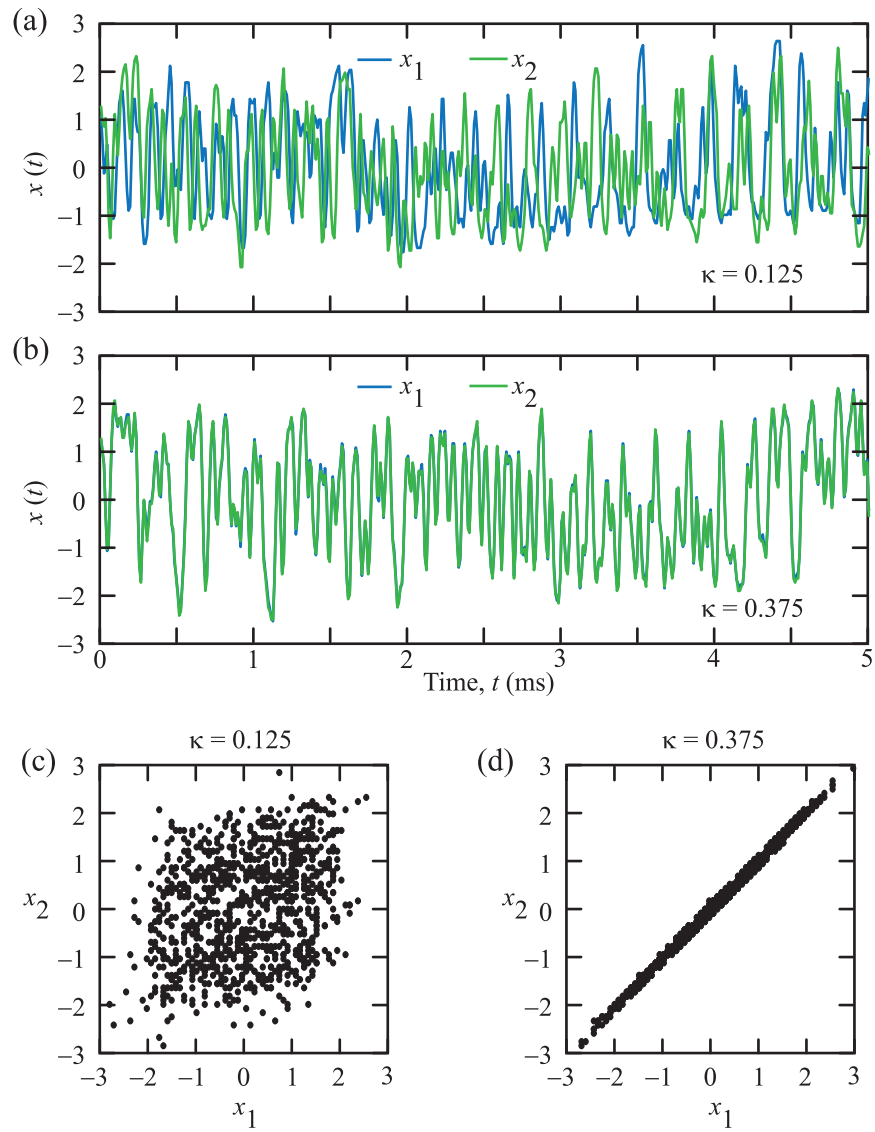


Figure 3.2: Dynamical behavior of coupled optoelectronic feedback loops. The two oscillators exhibit synchronized behavior when the interaction strength is sufficiently strong. Time series measurements of the two oscillators with coupling strengths (a) $\kappa = 0.125$ and (b) $\kappa = 0.375$ are shown. (c) and (d) show the synchronization plots for the same respective coupling strengths.

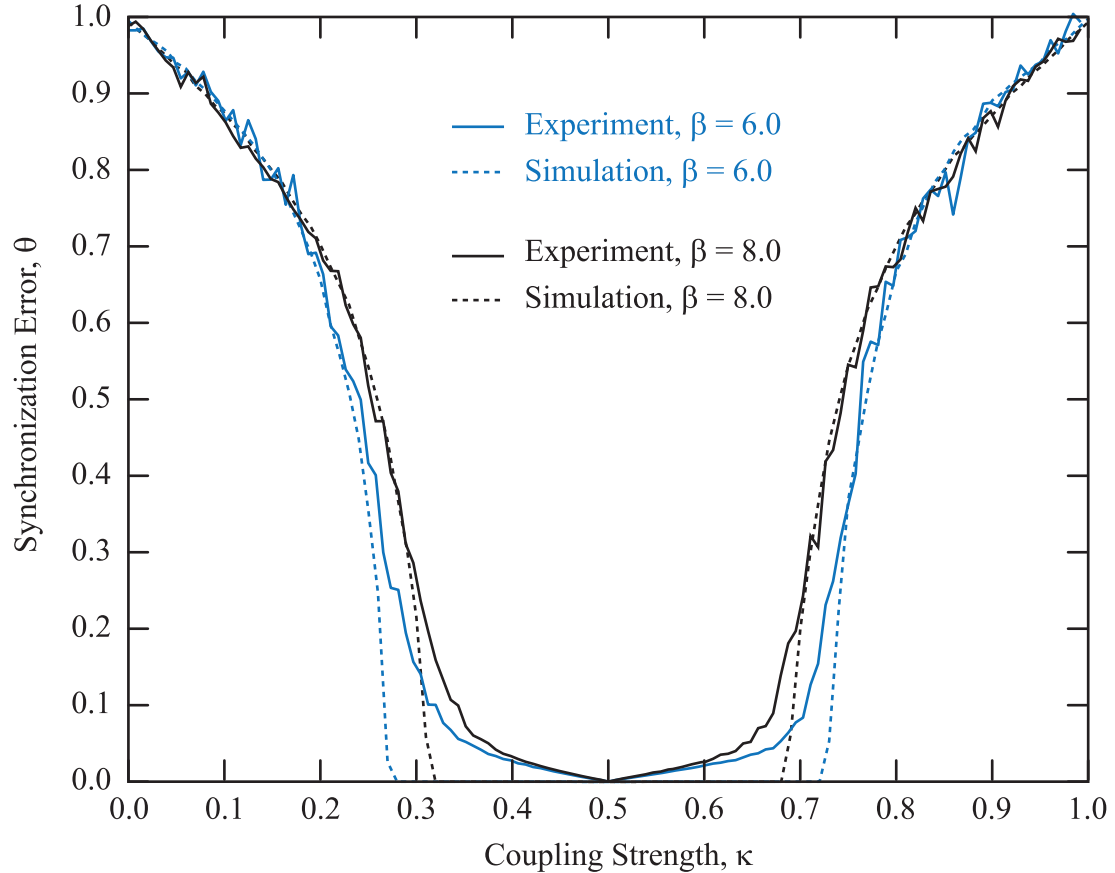


Figure 3.3: Range of coupling strength for stable synchrony. The solid lines show experimental measurements of the synchronization error θ as the coupling strength κ is varied, when $\beta = 6.0$ (blue) and $\beta = 8.0$ (black). The dashed lines show the corresponding results from numerical simulations.

of θ to be nonzero. It is also observed from Fig. 3.3, that the range of synchronization depends on the feedback strength β . In general, a higher value of β leads to more complicated dynamical behavior and consequently a smaller synchronization range.

Next, we examine the transient behavior to synchronization in the coupled oscillator system. An important measure that characterizes the transient behavior of coupled oscillators is the rate at which they converge to the synchronous solu-

tion. The rate to synchronization (μ) in a network of dynamical systems is a widely significant property which has implications for sensor networks and communication systems. In sensor networks, the convergence rate determines the speed of perturbations that can successfully be detected, while in certain chaos based communication systems, the rate of convergence influences the speed at which information can be successfully communicated, or the bandwidth of information that can be effectively encrypted or hidden by the chaotic carrier.

The rate at which the trajectories of coupled oscillators converge or diverge is quantified by the transverse Lyapunov exponents (TLEs) [19]. The TLEs are defined as the average exponential rates at which the trajectories of the coupled systems converge/diverge along various network modes transverse to the synchronization manifold $\mathbf{u}_1 = \mathbf{u}_2 = \dots = \mathbf{u}_N$. A negative TLE implies that the trajectories converge along the corresponding mode while a positive TLE indicates divergent behavior. The synchronous solution in a network of oscillators is stable if the maximal TLE (among all transverse modes) is negative. The stability analysis for the two-node network of the optoelectronic oscillators described here is done in Ref. [55]. For the two-oscillator system, there is only one perturbation mode transverse to the synchronization manifold. Thus the convergence properties are completely characterized by the corresponding TLE.

An experimental measurement of the rate to synchronization μ (or the maximal TLE which is equal to $-\mu$) can be accomplished by abruptly turning on the coupling between two oscillators and analyzing the transient from the initially uncorrelated state to synchronized behavior. This process is illustrated in Fig. 3.4. A

measurement of the dynamics $x(t)$ of the two oscillators, before and after the coupling is turned on, is shown in Fig. 3.4 (a). The bidirectional coupling strength κ is switched from a value of zero to $\kappa = 0.3125$ at $t = 0$. Fig. 3.4 (b) shows the natural logarithm of the smoothed absolute difference $\ln(\langle |x_1(t) - x_2(t)| \rangle)$ as a function of time. A moving-window smoothing is performed, over a time-interval of $100 \mu s$, in order to avoid potential divergences of the logarithm caused when $x_1(t) = x_2(t)$. The transient shows an exponential convergence from the initially uncorrelated behavior to a synchronous state as predicted [19]. By estimating the slope of the transient, we can determine the convergence rate μ (or the maximal TLE, $-\mu$). Fig. 3.5 shows the maximal TLE, $-\mu$, measured as a function of the coupling strength along with results from numerical simulations. For each value of κ , the measurements and simulations were performed for 100 independent realizations and the mean value of the estimated maximal TLE is shown along with its standard deviation. Note that the maximal TLE is negative indicating the convergent nature of the network dynamics.

3.3 Stability Analysis: Master Stability Function

In 1998, Pecora and Carroll introduced a theoretical technique to analyze the stability of the synchronous solution of a network of dynamical oscillators [33]. This method, called master stability function (MSF) analysis, provides a necessary and sufficient condition for the stability of the synchronous solution in terms of the eigenvalues of the coupling matrix. Here, we briefly describe the technique and discuss its implications for our study. Consider a network of N generalized oscillators

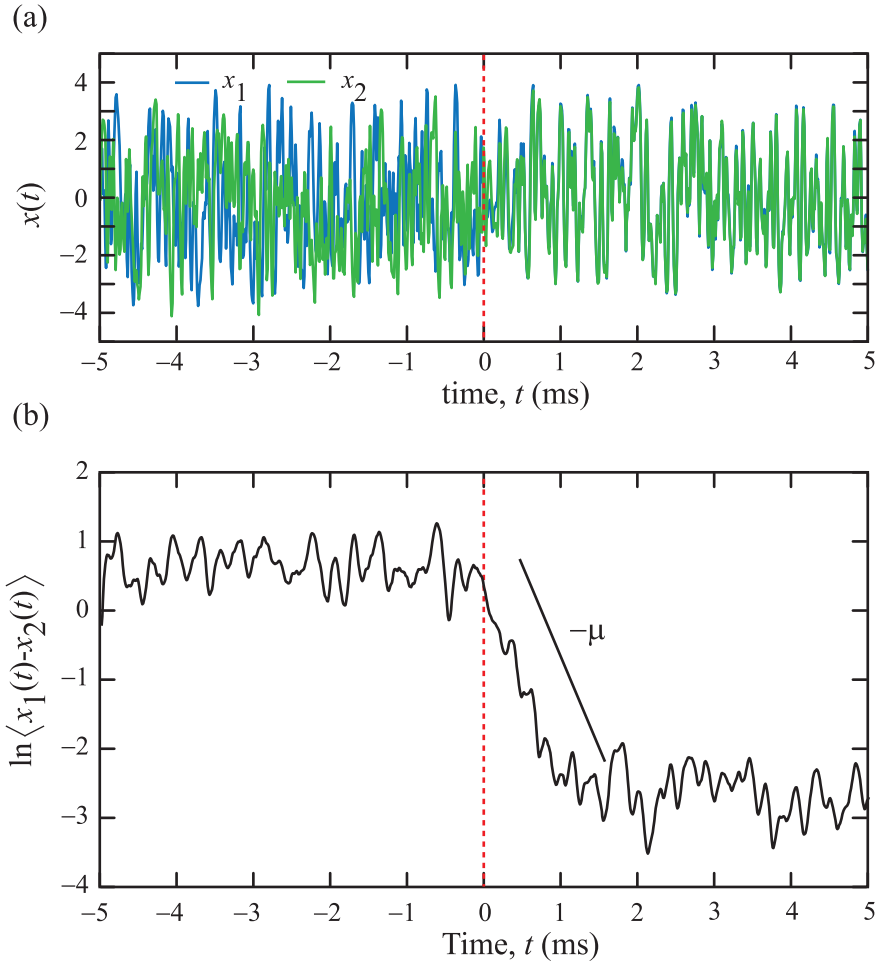


Figure 3.4: Measurement of the maximal transverse Lyapunov exponent (TLE), $-\mu$. (a) Time series measurement of the dynamics of the oscillators before and after the coupling is turned on abruptly at $t = 0$. The transient to synchronization is exponential in nature as is evident from (b) which shows $\ln(\langle |x_1 - x_2| \rangle)$ plotted as a function of time t . The maximal TLE, $-\mu$, is estimated from the slope of the transient.

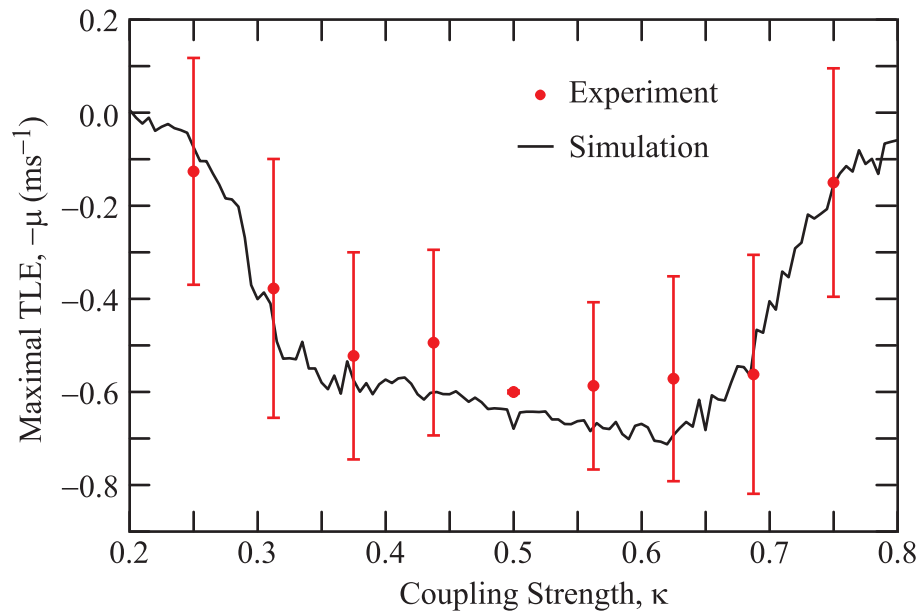


Figure 3.5: Maximal TLE, $-\mu$, as a function of the coupling strength κ . The red dots show the mean value of $-\mu$ obtained from 100 independent experiment measurements while the solid line shows results from simulations. The bars represent the standard deviation of the measurements.

where the dynamics of the i^{th} oscillator are described by the equation

$$\frac{d\mathbf{x}_i}{dt} = \mathbf{F}(\mathbf{x}_i) + \sum_j L_{ij} \mathbf{H}(\mathbf{x}_j). \quad (3.11)$$

Here \mathbf{x}_i is an $m \times 1$ vector that denotes the state of the i^{th} oscillator, \mathbf{F} is a vector function that describes the uncoupled oscillator dynamics, \mathbf{L} is the Laplacian coupling matrix which is assumed to have a zero row-sum, and \mathbf{H} describes the vector coupling function. The above N equations describing the dynamics of the network can be combined into a single equation as

$$\frac{d\mathbf{x}}{dt} = \mathbf{F}(\mathbf{x}) + \mathbf{L} \otimes \mathbf{H}(\mathbf{x}) \quad (3.12)$$

where $\mathbf{x} = (\mathbf{x}_1, \mathbf{x}_2, \dots, \mathbf{x}_N)$, $\mathbf{F}(\mathbf{x}) = [\mathbf{F}(\mathbf{x}_1), \mathbf{F}(\mathbf{x}_2), \dots, \mathbf{F}(\mathbf{x}_N)]$, $\mathbf{H}(\mathbf{x}) = [\mathbf{H}(\mathbf{x}_1), \mathbf{H}(\mathbf{x}_2), \dots, \mathbf{H}(\mathbf{x}_N)]$, and \otimes denotes the direct or Kronecker product [56]. The stability of the synchronous solution is analyzed by considering the variational equation obtained by linearizing Eqn. 3.12 about the synchronous solution. Performing the linearization gives

$$\frac{d\boldsymbol{\xi}}{dt} = [\mathbf{1}_N \otimes D\mathbf{F} + \mathbf{L} \otimes D\mathbf{H}] \boldsymbol{\xi}. \quad (3.13)$$

Here $\boldsymbol{\xi} = [\boldsymbol{\xi}_1, \boldsymbol{\xi}_2, \dots, \boldsymbol{\xi}_N]$ is the vector incorporating the variations of all nodes and $D\mathbf{F}$ and $D\mathbf{H}$ denote the Jacobian matrices corresponding to \mathbf{F} and \mathbf{H} evaluated at the synchronous solution, $\mathbf{x}_1 = \mathbf{x}_2 = \dots = \mathbf{x}_N$. Eqn. 3.13 can be readily block-diagonalized (provided the Laplacian coupling matrix \mathbf{L} is diagonalizable¹, as we assume here) to result in N ($m \times 1$) equations written as

$$\frac{d\boldsymbol{\xi}_i}{dt} = [D\mathbf{F} + \lambda_i D\mathbf{H}] \boldsymbol{\xi}_i. \quad (3.14)$$

¹An extension of this theory to the case where the coupling matrix is nondiagonalizable has been done in Ref. [57].

We note that in the above equation, i indexes the eigenmodes (not the network nodes) of the coupling matrix \mathbf{L} and λ_i denote the corresponding eigenvalues. The coupling matrix \mathbf{L} has at least one zero eigenvalue $\lambda_1 = 0$ owing to its zero row-sum property [58]. This mode corresponds to evolution along the synchronization manifold, $\mathbf{x}_1 = \mathbf{x}_2 = \dots = \mathbf{x}_N$, while the other $N - 1$ modes are transverse to the synchronization manifold. A perturbation along the transverse directions represents a deviation away from the synchronous solution. For the synchronous solution to be stable we require that the perturbations along the transverse directions decay i.e. we require that the maximal Lyapunov exponents of the variational equations for all transverse modes be negative. Since the variational equations for the transverse modes (Eqn. 3.14) differ from each other only by the eigenvalue λ_i , we can rewrite Eqn. 3.14 by incorporating a generalized complex eigenvalue $(\alpha_R + i\alpha_I)$ as

$$\frac{d\xi}{dt} = [D\mathbf{F} + (\alpha_R + i\alpha_I)D\mathbf{H}]\xi. \quad (3.15)$$

Calculating the maximal Lyapunov exponent of the general equation above yields us the stability function M whose argument is the complex eigenvalue $(\alpha_R + i\alpha_I)$. Then, to determine the stability of the synchronous solution of any given network, one only has to calculate the eigenvalues of the coupling matrix that correspond to the transverse modes and evaluate the MSF for these eigenvalues. If for all eigenvalues, the value of the MSF is negative, then the synchronous solution is linearly stable.

By decoupling the network topology and the dynamical nature of the constituent nodes, the MSF provides us with a powerful tool that allows us to predict

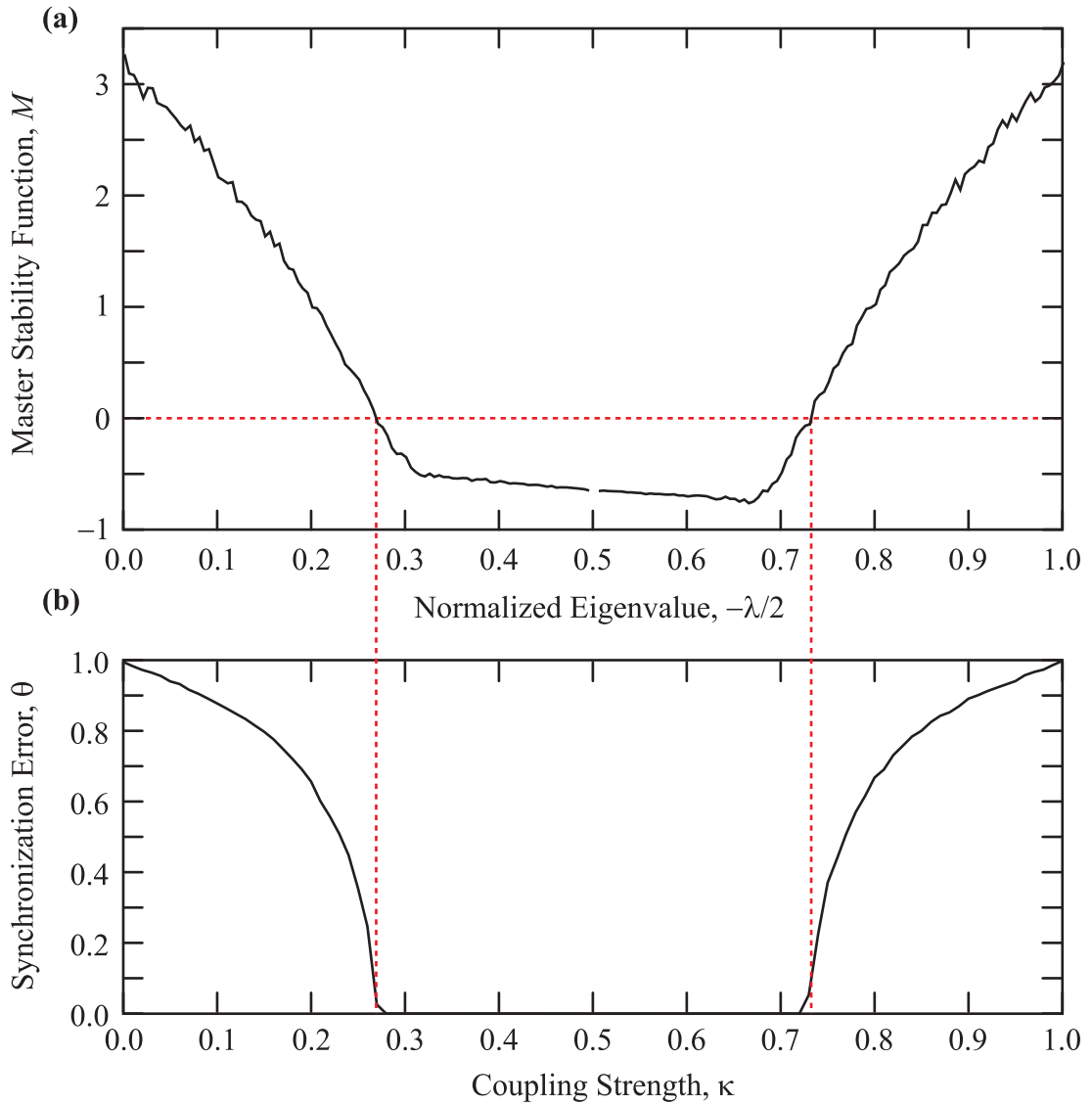


Figure 3.6: Master stability function (M) and the regime of stable synchronization. (a) A cut along the real-axis of M as a function of the scaled eigenvalue for $\beta = 6.0$. The scaling relates the eigenvalue directly to the coupling strength κ . (b) Synchronization error θ as a function of κ (reproduced here from Fig. 3.3). The vertical dashed lines identify the regime of stable synchronization for the two-oscillator network as predicted by the MSF.

whether a given network of oscillators will synchronize. We employ this technique to analyze the range of coupling strength over which a network of two optoelectronic oscillators can stably synchronize. The symmetric, bidirectionally coupled 2-node network realized in our experiments is described by the Laplacian coupling matrix

$$\mathbf{L} = \begin{bmatrix} -\kappa & \kappa \\ \kappa & -\kappa \end{bmatrix}. \quad (3.16)$$

The eigenvalues of the matrix above are $\{\lambda_1, \lambda_2\} = \{0, -2\kappa\}$. Of these eigenvalues, $\lambda_1 = 0$ corresponds to the mode that evolves along the synchronization manifold. Thus, the synchronous solution in the two-node network will be stable if the MSF takes a negative value at $\lambda_2 = -2\kappa$. Fig. 3.6 (a) shows a cut along the real axis of the theoretically calculated MSF for our optoelectronic oscillators for a feedback strength value of $\beta = 6.0$. In order to establish a direct correspondence with the coupling strength κ , the MSF is plotted as a function of the eigenvalue scaled by $-1/2$. In Fig. 3.6 (b), we reproduce the numerically calculated synchronization error θ (also shown in Fig. 3.3) for $\beta = 6.0$, obtained by simulating the time domain equations for the two-node network. The vertical lines in the figure identify the coupling strengths at which the MSF changes sign. These points determine the region of κ for which the synchronous solution is linearly stable (we are interested in the region where M is negative). As the results show, the MSF correctly predicts the range of coupling strength for which the network exhibits stable synchronization. The utility of the MSF goes further than just predicting the range of coupling strength over which the network synchronizes. It can also be used to infer the rate of convergence to synchrony. This can be seen by comparing the MSF (shown

in Fig. 3.6 (b)) to the maximal TLE calculated from simulating the dynamical equations (Fig. 3.5). Within the region of stability the maximal TLE calculated from simulations agrees well with the MSF values. The MSF approach, thus, provides us with a very powerful tool to analyze the synchronization behavior of any given network of dynamical oscillators.

3.4 Summary

In this chapter, we introduced the mathematical equations that describe a general network of optoelectronic oscillators. Experimental results and numerical simulations showing the synchronization of coupled oscillators were reported. Quantities that characterize the synchronized behavior, such as the synchronization error θ and the rate to synchronization μ , were defined and their measurements from a two-node network were presented. Finally, we described the master stability function approach, a powerful means of analyzing the stability of the synchronous solution.

Chapter 4

Adaptive Synchronization of Coupled Optoelectronic Oscillators ¹

In the preceding chapter, we discussed the coupling of optoelectronic feedback loops and developed the mathematical equations that describe the dynamics of a network. We considered two coupling methods viz. injective and diffusive coupling. In both these schemes, for the existence of a global synchronous solution, it is required that the row-sums of the corresponding coupling matrix be uniform. However, in practical situations, where the coupling matrix elements are unavoidably subject to environmental perturbations, this condition may not always be satisfied. By engineering the network to have the flexibility to adapt and adjust to coupling perturbations, we can minimize the effect of unknown coupling changes and establish a system that automatically synchronizes.

Adaptive synchronization algorithms in a network of nonlinear oscillators have been a topic of great interest [27, 59–67], partly because of the need for high-quality synchronization in practical applications. In Ref. [27], Sorrentino and Ott proposed an adaptive synchronization algorithm that establishes and maintains synchrony even when the coupling parameters are unknown and time-dependent. This strategy provides a prescription according to which each node of the network builds a dynamical estimate of the total incoming coupling strength based on just the received coupling signal and its own local dynamics. Each oscillator then uses the

¹Some of the results presented in this chapter have also been published in Refs. [31, 32]

estimate to suitably adjust its internal parameters to compensate for the external perturbations.

We realize this adaptive synchronization algorithm on networks of optoelectronic oscillators. The adaptive algorithm is implemented by exploiting the computational power of the DSP boards that have been integrated as part of the feedback loops. Using networks of two and three oscillators, we demonstrate synchronization even when the coupling strengths are changing in time. Additionally, we are able to track the perturbations in real-time and establish the utility of networks of chaotic oscillators as sensors.

In Sec. 4.1, we derive the adaptive synchronization technique, introduced in [27], as applied to our optoelectronic systems. In Sec. 4.2, we discuss the details of the experimental set-up of a unidirectional diffusively-coupled network of two optoelectronic oscillators used to demonstrate the success of the adaptive algorithm.

Results from the implementation of the adaptive synchronization algorithm on the two-oscillator network are presented in Sec. 4.3. The results presented in this section have been published in Refs. [31, 55]. The adaptive algorithm successfully keeps the two oscillators synchronized while allowing us to track the coupling channel perturbations. We establish the efficacy of the adaptive technique by comparing the degree of synchronization attained with the adaptive strategy enabled to that of an uncontrolled network.

In Sec. 4.4, we present results demonstrating the success of the adaptive strategy in tracking perturbations occurring simultaneously in multiple coupling links in a network of three mutually-coupled optoelectronic oscillators. In this context, we

discuss the implications of tracking capabilities of the adaptive strategy to sensing applications. Some of the results presented in this section have been published in Ref. [32].

4.1 Adaptive Algorithm

In this section, we derive an adaptive synchronization strategy for a network of optoelectronic oscillators using the methods described in Ref. [27]. We begin by considering N coupled optoelectronic oscillators described by the equations Eqns. 3.2 which are reproduced below for convenience.

$$\begin{aligned} \frac{d\mathbf{u}_i(t)}{dt} &= \mathbf{A}\mathbf{u}_i + \beta\mathbf{B} \cos^2 [x_i(t - \tau) + \phi_0], \\ w_i(t) &= \mathbf{C}\mathbf{u}_i(t), \\ x_i(t) &= w_j(t) + \sum_{j \neq i} K_{ij} w_j(t). \end{aligned} \tag{4.1}$$

Each network node i is assumed to have access only to the received cumulative coupling signal $h_i(t) \equiv \sum_{j \neq i} K_{ij} w_j(t)$ but not to the individual node dynamics $w_j(t)$ of the other oscillators or the coupling strengths K_{ij} . By adding the local filter output $w_i(t)$ to $h_i(t)$ and enforcing $K_{ii} = 1$ we can express the net feedback signal as

$$s_i(t) \equiv \sum_{j=1}^N K_{ij} w_j(t). \tag{4.2}$$

For a synchronous solution to be admitted by Eqns. 4.1, we require that the row sums of the coupling matrix \mathbf{K} be uniform. This condition ensures that all the optoelectronic oscillators operate at the same net feedback strength, thus allowing

the possibility of synchronization. In order to ensure that a synchronous solution is permitted, we modify the above equations by dividing the feedback signal x_i by the total coupling strength, $k_i \equiv \sum_{j=1}^N K_{ij}$ (including the self-feedback strength K_{ii}).

The equations can then be expressed as

$$\begin{aligned} \frac{d\mathbf{u}_i(t)}{dt} &= \mathbf{A}\mathbf{u}_i + \beta\mathbf{B} \cos^2 [x_i(t - \tau) + \phi_0], \\ w_i(t) &= \mathbf{C}\mathbf{u}_i(t), \\ x_i(t) &= \frac{1}{k_i} s_i(t). \end{aligned} \tag{4.3}$$

It can be readily seen that Eqns. 4.3 admit a synchronous solution that evolves according to the equations of an uncoupled oscillator. However, in rewriting the equations in the above form, we assumed full knowledge of the net coupling k_i coming into each node i . But, what can be done in cases when this knowledge is not available? This is usually the case in practical situations, where the coupling elements may be subject to unpredictable environmental fluctuations. To address this problem, we derive a strategy that adaptively forms a dynamical estimate \bar{k}_i of the net coupling coming into each node based on just the local feedback signal $s_i(t)$ and its own internal dynamics $w_i(t)$. By replacing k_i in the above equations with this estimate \bar{k}_i we can ensure that the synchronous solution is possible even when the couplings are not known *a priori*.

We begin by defining a mean-squared exponentially weighted synchronization error function $\psi_i(t)$ as

$$\psi_i(t) \equiv \int_{-\infty}^t e^{-\nu(t-t')} [s_i(t') - \bar{k}_i(t')w_i(t')]^2 dt', \tag{4.4}$$

where, ν defines the size of the exponential averaging window. The exponentially

weighted moving average is in fact equivalent to a lowpass filter operation. Our objective is to find \bar{k}_i that minimizes the above synchronization error. To this end, we take the derivative of $\psi_i(t)$ with respect to \bar{k}_i and set it equal to zero. This gives us

$$\int_{-\infty}^t e^{-\nu(t-t')} [s_i(t')w_i(t')] dt' = \int_{-\infty}^t e^{-\nu(t-t')} [\bar{k}_i(t')w_i^2(t')] dt'. \quad (4.5)$$

If we assume that the time-variation of the coupling coefficients is much slower compared to the dynamics of the oscillators and the exponential averaging time, then we can effectively treat \bar{k}_i as a constant in the integral on the right hand side. We can then pull this term out of the integral and obtain an equation that describes the evolution of \bar{k}_i . Carrying out this procedure gives us

$$\bar{k}_i(t) = \frac{\int_{-\infty}^t e^{-\nu(t-t')} [s_i(t')w_i(t')] dt'}{\int_{-\infty}^t e^{-\nu(t-t')} [w_i^2(t')] dt'} \equiv \frac{P_i(t)}{Q_i(t)}. \quad (4.6)$$

Thus, by taking the ratio of two locally available signals, each node of the network can estimate the total incoming coupling strength. \bar{k}_i can be more conveniently calculated by recognizing that the numerator $P_i(t)$ and the denominator $Q_i(t)$ follow the differential equations

$$\begin{aligned} \frac{dP_i(t)}{dt} &= -\nu P_i(t) + s_i(t)w_i(t), \\ \frac{dQ_i(t)}{dt} &= -\nu Q_i(t) + w_i^2(t). \end{aligned} \quad (4.7)$$

Each of the above differential equations corresponds to a lowpass filter with a time-constant $1/\nu$. For the success of the adaptive algorithm, the filter corner frequency has to be chosen such that $\tau_o \ll \nu^{-1} \ll \tau_n$ where τ_o is the time-scale on which the oscillator dynamics evolves and τ_n is the time-scale on which the network evolves.

To make the above scheme amenable to implementation using our DSP boards, we now derive the adaptive algorithm in discrete-time. In discrete-time, we define the average synchronization error as

$$\psi[n] \equiv \sum_{m=0}^{\infty} z_0^m \left\{ s_i[n-m] - \bar{k}_i[n-m] w_i[n-m] \right\}^2, \quad (4.8)$$

where z_0 (< 1), called the *forgetting factor*, determines the span of the moving average window, which can be expressed in terms of the sampling time as $T_s/(1-z_0)$.

Differentiating Eqn. 4.8 with respect to \bar{k}_i and setting the derivative to zero gives us

$$\sum_{m=0}^{\infty} z_0^m s_i[n-m] w_i[n-m] = \sum_{m=0}^{\infty} z_0^m \bar{k}_i[n-m] w_i^2[n-m]. \quad (4.9)$$

Again, assuming that the coupling parameters vary sufficiently slowly compared to the averaging time allows us to pull \bar{k}_i out of the summation. Rearranging the terms gives us

$$\bar{k}_i[n] = \frac{\sum_{m=0}^{\infty} z_0^m s_i[n-m] w_i[n-m]}{\sum_{m=0}^{\infty} z_0^m w_i^2[n-m]} \equiv \frac{P_i[n]}{Q_i[n]}. \quad (4.10)$$

On a DSP board, we can compute the estimate \bar{k}_i by independently computing $P_i[n]$ and $Q_i[n]$ using the iterative difference equations

$$\begin{aligned} P_i[n] &= z_0 P_i[n-1] + (1-z_0) s_i[n] w_i[n], \\ Q_i[n] &= z_0 Q_i[n-1] + (1-z_0) w_i^2[n], \end{aligned} \quad (4.11)$$

which are nothing more than discrete-time lowpass filters with z_0 as the pole.

4.2 Implementation of the Adaptive Algorithm: Two-node Network

Here, we present the details of a two-node experimental network used to implement the adaptive algorithm developed in the preceding section. Results demonstrating the success of the adaptive strategy are reported in the Sec. 4.3. Fig. 4.1 shows a schematic of our experimental setup. It consists of two unidirectionally coupled optoelectronic oscillators which will, henceforth, be identified as the transmitter (denoted node 1) and the receiver (denoted node 2). The transmitter is an independently running feedback loop system while the receiver dynamics are influenced by the transmitter through a coupling signal. In our experiments, the transmitter and the receiver are coupled optically. The optical output of the MZM of the transmitter is split into two equal parts using a 50-50 fiber-optic splitter. While one part serves as the self-feedback signal, the other part is relayed to the receiver over a fiber-optic communication channel. In our experiments, we simulate environmental coupling disturbances by a time-dependent coupling strength $\kappa(t)$. This is accomplished by inserting another MZM in the fiber-optic coupling link from the transmitter to the receiver systems. When biased at the quadrature point $\phi_0 = -\pi/4$, the modulator acts as a linear voltage-controlled attenuator for small modulation voltages. An arbitrary waveform generator (Agilent 81150A) is used to generate the electrical modulation voltage that controls the coupling variation imposed by the modulator. The self-feedback optical signals of the transmitter and the receiver, denoted $P_1(t)$ and $P_2(t)$ respectively, and the coupling signal to the receiver $\kappa P_1(t)$ are photo-detected and subject to bandpass filtering and time-delay operations on the DSP

boards. The resultant filtered quantities, $x_1(t)$, $x_2(t)$ and $\kappa(t)x_1(t)$, are then used to construct the feedback voltages input to the modulator. Here, we assume that the time-variation of κ is slow compared to the filter corner frequencies allowing us to effectively treat $\kappa(t)$ as a constant for the purposes of filtering. This allows us to write the resultant of the filtering action on $\kappa P_1(t)$ as $s(t) \equiv \kappa(t)x_1(t)$. In addition to the filtering and time-delay operations, the receiver also implements, through its DSP board, the adaptive algorithm that constructs a dynamical estimate $\bar{\kappa}$ of the coupling strength based on the filtered received signal $s(t)$ and the local dynamics $x_2(t)$. We emphasize that the receiver has access only to the signal $s(t) = \kappa(t)x_1(t)$ and has no knowledge of the transmitter dynamics $x_1(t)$ or the coupling strength $\kappa(t)$ separately. Though we implement the adaptive strategy using a DSP board, analog signal processing with mixers and lowpass filters could also have been used.

In our experiments, the transmitter and the receiver systems are adjusted to be nominally identical. The feedback strengths of the two oscillators are set to be equal to $\beta = 3.58$ by adjusting the input optical power to the MZMs appropriately. Both the modulators are biased to operate at $\phi_0 = -\pi/4$. The sampling rate of the ADCs and the DACs on both the DSP boards is set to $F_s = 1/T_s = 24$ kSs⁻¹ and highpass and the lowpass filter corner frequencies are programmed to be $1/(2\pi\tau_H) = 100$ Hz and $1/(2\pi\tau_L) = 2.5$ kHz. A feedback time-delay $k = 36$ sampling time-steps (corresponding to a physical delay of 1.5 ms) is programmed on both the DSP boards. For these parameter values, the oscillators execute high-dimensional chaotic dynamics [55]. We point out that our experimental system could be scaled to operate at higher frequencies using either faster digital signal

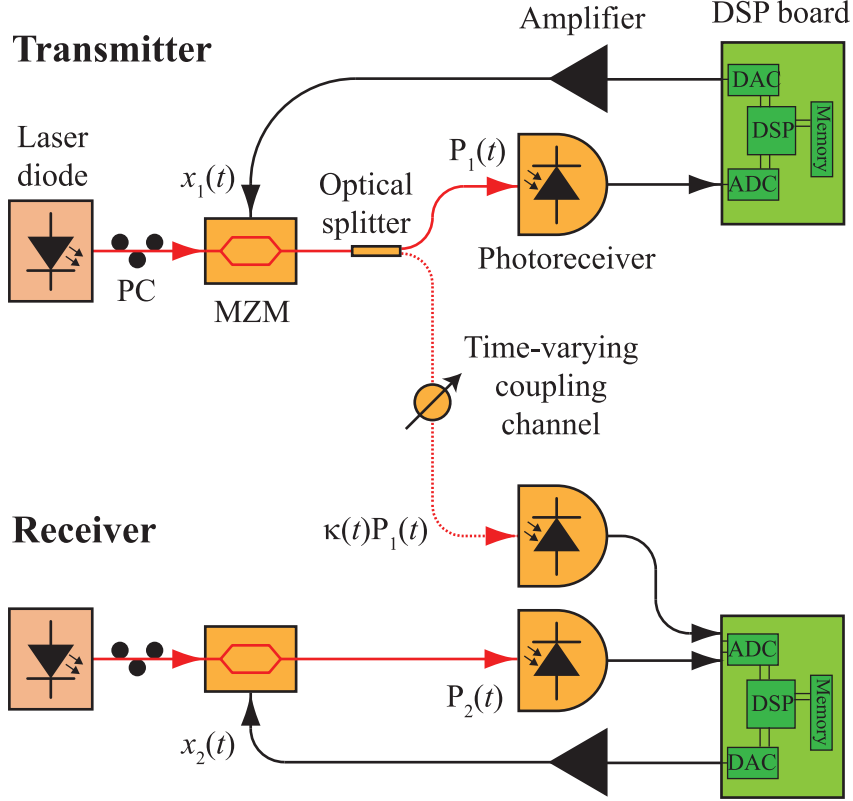


Figure 4.1: Experimental schematic of a unidirectionally coupled two-oscillator network. The fiber-optic coupling channel may be subject to unknown time-dependent perturbations.

processing or high-speed analog filters and mixers.

The equation describing the transmitter system (represented in discrete-time) is given as

$$x_1[n] = -\sum_{j=1}^2 a_j x_1[n-j] + \beta \sum_{j=0}^2 b_j \cos^2(x_1[n-k-j] + \phi_0) \quad (4.12)$$

where a_j and b_j are the filter coefficients. For the two-pole bandpass filter chosen here they are given as $a_1 = -1.4962$, $a_2 = 0.5095$, $b_0 = 0.2452$, $b_1 = 0.0$, and $b_2 = -0.2452$. The receiver dynamics are influenced by the transmitter through the

coupling signal. It is governed by the equations,

$$x_2[n] = -\sum_{j=1}^2 a_j x_2[n-j] + \beta \sum_{j=0}^2 b_j \cos^2 \{(1 - \bar{\kappa}[n-k])x_2[n-k-j] + s[n-k-j] + \phi_0\}, \quad (4.13)$$

where $\bar{\kappa}[n]$ is obtained by solving the iterative equations,

$$\begin{aligned} P[n] &= z_0 P[n-1] + (1 - z_0) s[n] x_2[n], \\ Q[n] &= z_0 Q[n-1] + (1 - z_0) x_2^2[n], \\ \bar{\kappa}[n] &= \frac{P[n]}{Q[n]}. \end{aligned} \quad (4.14)$$

In our experiments we choose the forgetting factor z_0 to be 0.95 corresponding to an averaging time of $T_s/[2\pi(1 - z_0)] = 0.83$ ms.

As our measurements, we record the following signals (after photodetection) using a digital oscilloscope (Tektronix TDS 7104).

- The optical output of the transmitter, $P_1(t)$.
- The optical output of the receiver, $P_2(t)$.
- The optical coupling signal, $\kappa P_1(t)$.

In addition to the above signals, we also observe the calculated value of $\bar{\kappa}$.

4.3 Experimental Results from a Two-node Network

In this section, we present the experimental results from the implementation of the adaptive strategy on the two-node network. As can be readily seen from

Eqns. 4.12 and 4.13, the two coupled optoelectronic oscillators in our experiment admit a synchronous solution only when the $\bar{\kappa} = \kappa$. Under this condition, carrying out the master stability analysis (as discussed in Sec. 3.3) reveals that the synchronous solution for the coupled oscillator system is stable when $0.45 < \kappa < 1.49$. Thus, if the receiver can correctly estimate κ , the system can be maintained in a synchronous state over a range of different values of κ . As described in the previous section, our adaptive strategy strives to maintain the synchronous solution by matching the estimate $\bar{\kappa}$ to the actual coupling strength κ .

To illustrate the functioning of the adaptive algorithm, we begin by considering the effect of a mismatched coupling strength estimate $\bar{\kappa}$ on synchronization. This situation is portrayed in Figs. 4.2 (a) and (b). Fig. 4.2 (a) shows the coupling strength $\kappa(t)$ (black curve) and its estimate $\bar{\kappa}(t)$ (green curve). Fig. 4.2 (b) shows the synchronization error signal $[x_1(t) - x_2(t)]$. The network is initially ($t < 0$) configured by setting $\bar{\kappa} = \kappa = 0.8$. Under these conditions, the receiver is synchronized to the transmitter as seen from the small error in Fig. 4.2 (b). At time $t = 0$, the coupling strength is suddenly switched to $\kappa = 1.13$ while the estimate is held fixed at $\bar{\kappa} = 0.8$. This causes the two oscillators to quickly lose synchrony as the difference error signal shows. This is expected, since the coupled equations that describe the dynamics of the network, without adaptation, no longer admit a synchronous solution. In Figs. 4.2 (c) and (d) we consider the same situation, only this time we employ the adaptive algorithm. Fig. 4.2(c) shows the dynamical estimate $\bar{\kappa}$ (green curve) calculated by the receiver using Eqns. 4.14. We see that, using the adaptive strategy, the receiver system is able to form a dynamical estimate $\bar{\kappa}$ that tracks the

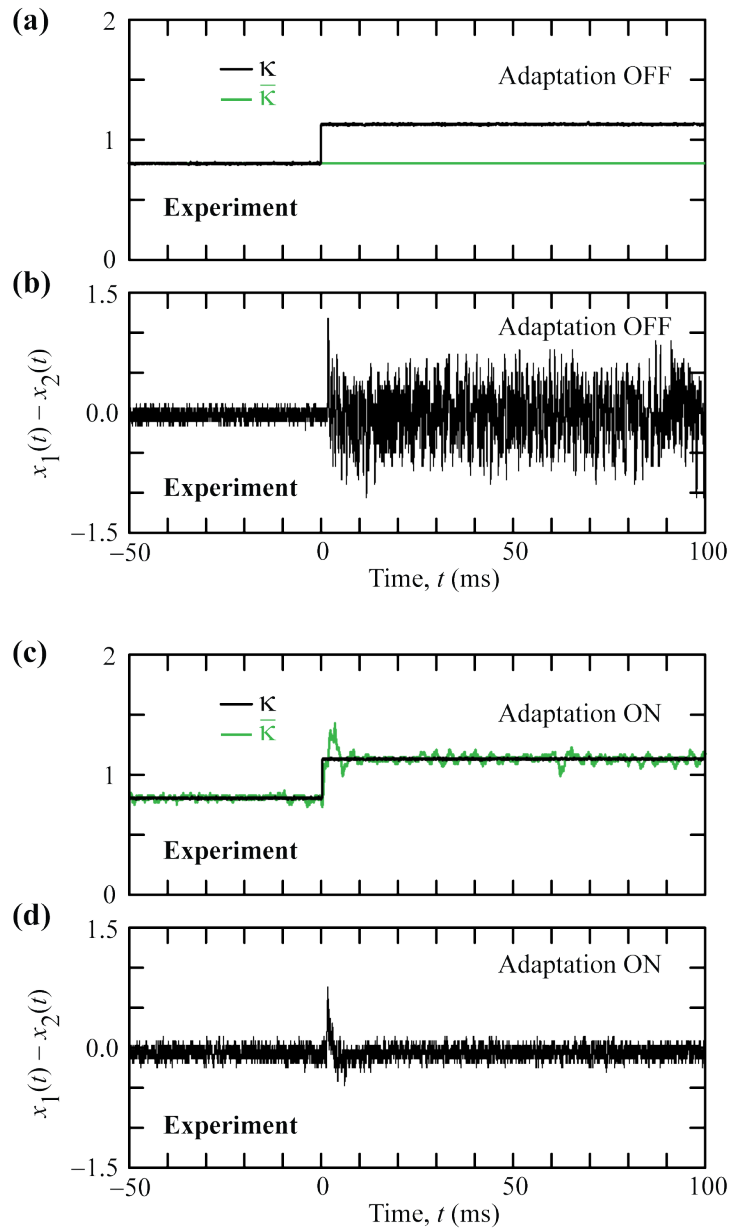


Figure 4.2: Response of the 2-node system to a step change in the coupling strength κ . (a) The coupling strength $\kappa(t)$ (black curve) is suddenly changed from 0.8 to 1.13 at $t = 0$. The adaptive strategy is disabled and the estimate $\bar{\kappa}$ (green curve) is held constant at 0.8. (b) The synchronization error as measured by the difference signal $[x_1(t) - x_2(t)]$. The same situation as portrayed in (a) and (b) is explored in (c) and (d), but with the adaptive algorithm enabled. The dynamical estimate $\bar{\kappa}$ now tracks $\kappa(t)$ leading to the maintenance of synchrony.

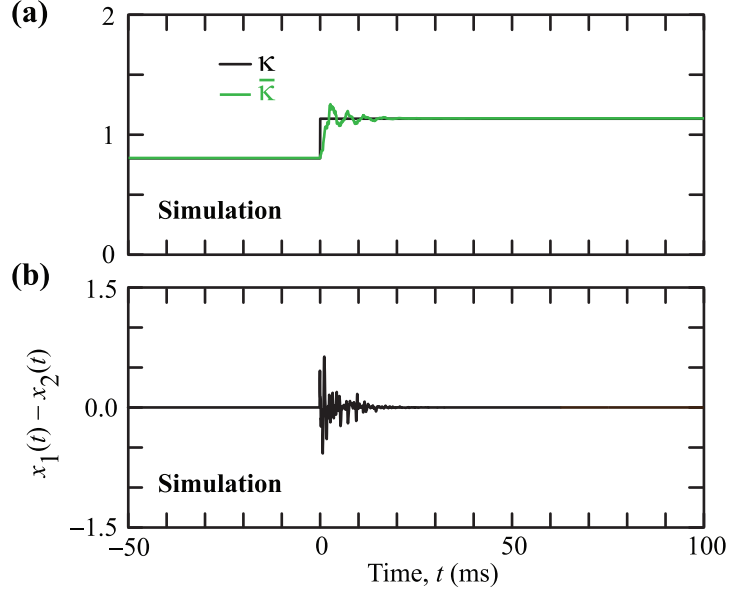


Figure 4.3: Numerical simulation of the response of an adaptive 2-node system to a step change in the coupling strength κ .

time-varying coupling κ . It is then able to suitably compensate for the changes in the coupling strength and keep the network synchronized as evidenced by the small error signal in Fig. 4.2 (d). In Fig. 4.3, we present results from numerical simulations of the same situation. In both experiments and simulations, we observe that, even with the adaptive strategy enabled, there is a brief period of time immediately following $t = 0$ when synchronization is lost. In this context, we point out that the adaptive algorithm, in fact, has the capability to acquire network synchrony from an unsynchronized state. The period for which the adaptive network loses synchrony following the step change, reflects the amount of time required by the adaptive algorithm to successfully build the estimate of κ . This time is related to the averaging time of the lowpass filters used in the adaptive algorithm, determined by

the choice of the forgetting factor z_0 . Using a smaller z_0 implies a smaller averaging time allowing us to track faster variations in κ . However, this affects the quality of the estimate as the process would then be using information over a shorter window of time in order to build $\bar{\kappa}$. If z_0 is set to be too low, then the algorithm may altogether fail to build an estimate of the fluctuating coupling strength, leading to a total loss of synchrony. Ref. [68] presents a detailed analysis of the effect of z_0 on the stability of the adaptive algorithm.

Next, we consider a variation of κ that is a smooth function of time. The adaptive algorithm is expected to work best when the coupling perturbations are slow and smooth. By using an arbitrary waveform generator and an electro-optic modulator inserted in the coupling channel, we impose a coupling strength variation of the form

$$\kappa(t) = \kappa_0 [1 + \epsilon \sin(2\pi f_m t)] \quad (4.15)$$

Here, κ_0 is the average coupling level about which we impose a sinusoidal variation, ϵ denotes the amplitude of the coupling strength change and f_m is a frequency that determines the speed of the imposed variation. The speed of the coupling variation is to be compared to the time-scale of the lowpass averaging process associated with the adaptive algorithm. The corner frequency of the lowpass averaging filter associated with the adaptive algorithm is given as $F_s(1 - z_0)/(2\pi)$. This value is equal to 191 Hz for our experimental parameters ($z_0 = 0.95$ and $F_s = 24 \text{ kSs}^{-1}$). Fig. 4.4 shows the performance of the adaptive strategy when a variation of the above form is applied with $\kappa_0 = 0.8$, $\epsilon = 0.2$ and $f_m = 20 \text{ Hz}$. Fig. 4.4 (a) shows the

form of the imposed variation $\kappa(t)$ (black curve) and its estimate $\bar{\kappa}$ (green curve) calculated by the receiver. The estimate faithfully tracks the imposed variation. In Fig. 4.4 (b), we show the synchronization plot of the optical output of the oscillators, $P_1(t)$ and $P_2(t)$, normalized with respect to the input optical power P_0 . The figure shows the relationship $P_1(t) = P_2(t)$ is satisfied thus confirming the maintenance of synchrony.

So far, we have demonstrated the success of the adaptive strategy in reestablishing synchronization after a step-like disturbance (Figs. 4.2 and 4.3) and tracking a purely sinusoidal coupling perturbation (Fig. 4.4). In what follows, we present results from the application of the adaptive strategy to track a more realistic perturbation with multiple frequency components. This perturbation is constructed, using an arbitrary waveform generator, as the sum of sinusoidal signals of frequencies 2, 4, 6, 8, and, 10 Hz with randomly chosen amplitudes and phases, together with a DC offset ($= 0.08$).

The results from the application of the adaptive synchronization technique to track this perturbation are presented in Fig. 4.5 and 4.6. In the top panel of Fig. 4.5 (a), we show experimental measurements of the optical signal $\kappa(t)P_1(t)$ received at the receiver (orange curve) and the difference synchronization error signal $(P_1 - P_2)$ (black curve) both normalized to the optical power P_0 entering the MZM. The received signal reflects the long time-scale coupling strength variations as a result of the simulated environmental fluctuations. Before time $t = 0$, the adaptive algorithm is disabled and the estimate $\bar{\kappa}$ is held fixed at the mean value of the coupling strength $\kappa = 0.8$. During this period, the synchronization of the two

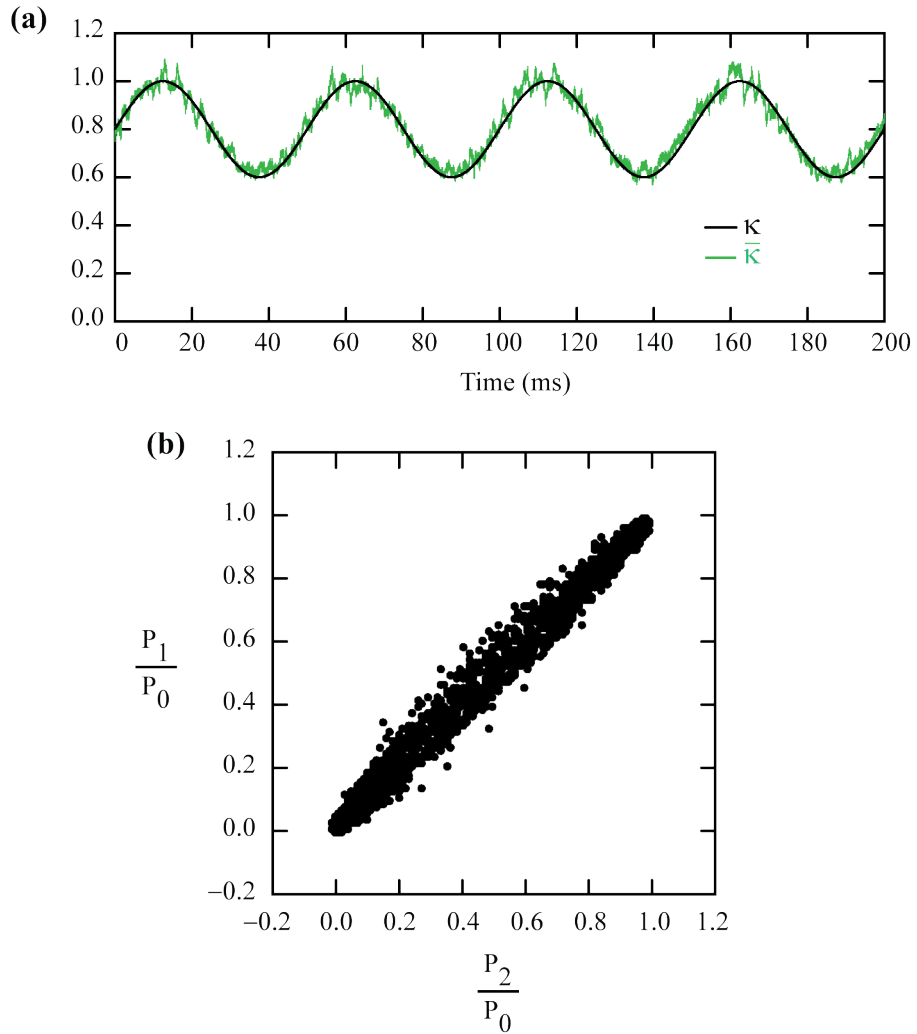


Figure 4.4: Adaptive tracking of a sinusoidal modulation of the coupling strength κ . (a) Imposed sinusoidal coupling strength modulation $\kappa(t)$ (black) and the dynamical tracking estimate $\bar{\kappa}(t)$ computed using the adaptive strategy (green). (b) Synchronization plot showing the synchronized dynamical behavior of the 2-node network.

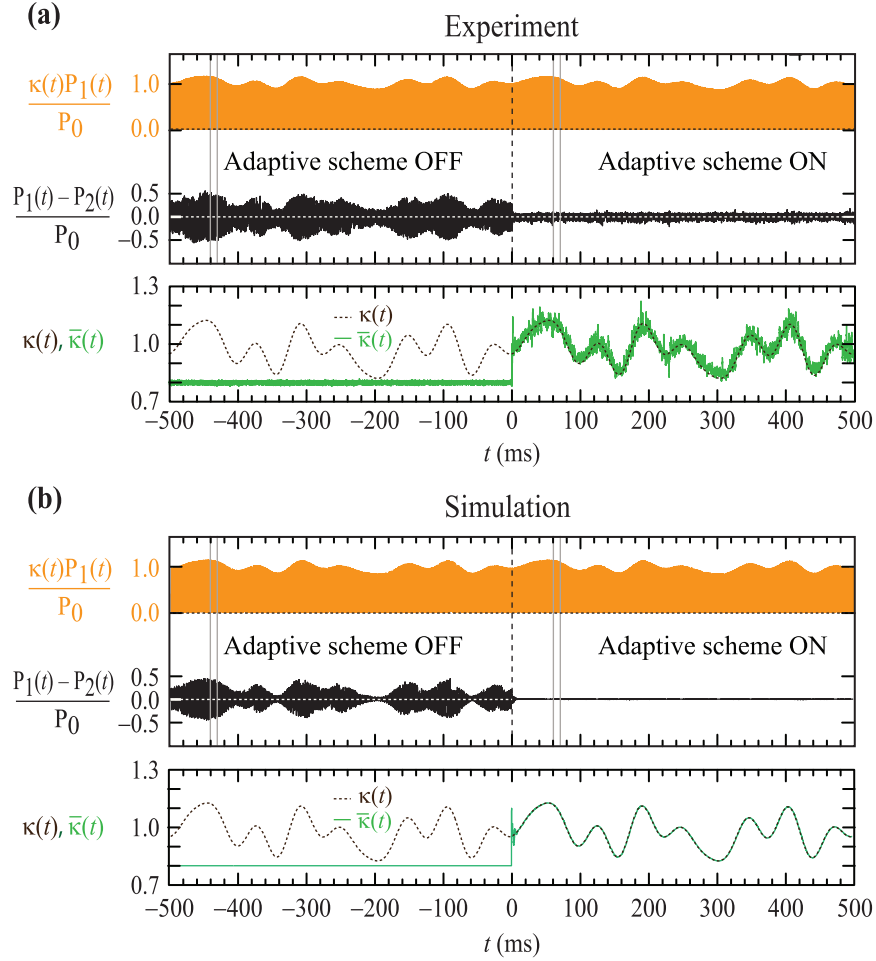


Figure 4.5: Adaptive synchronization algorithm applied to track an arbitrary coupling perturbation. (a) Results from experiments. The top-panel shows the measured coupling signal $\kappa(t)P_1(t)$ (orange curve) and the difference signal $[P_1(t) - P_2(t)]$ (black curve). Before $t = 0$, indicated by the vertical dashed line, the adaptive algorithm is disabled and the two oscillators are desynchronized. Following the enabling of the adaptive algorithm, synchronization is regained. The bottom panel shows the applied coupling perturbation $\kappa(t)$ (dotted line) and its real-time estimate $\bar{\kappa}(t)$ obtained once the adaptive strategy is switched on. (b) Corresponding results from numerical simulations. The gray solid vertical lines indicate the four intervals of time we present in more detail in Fig. 4.6.

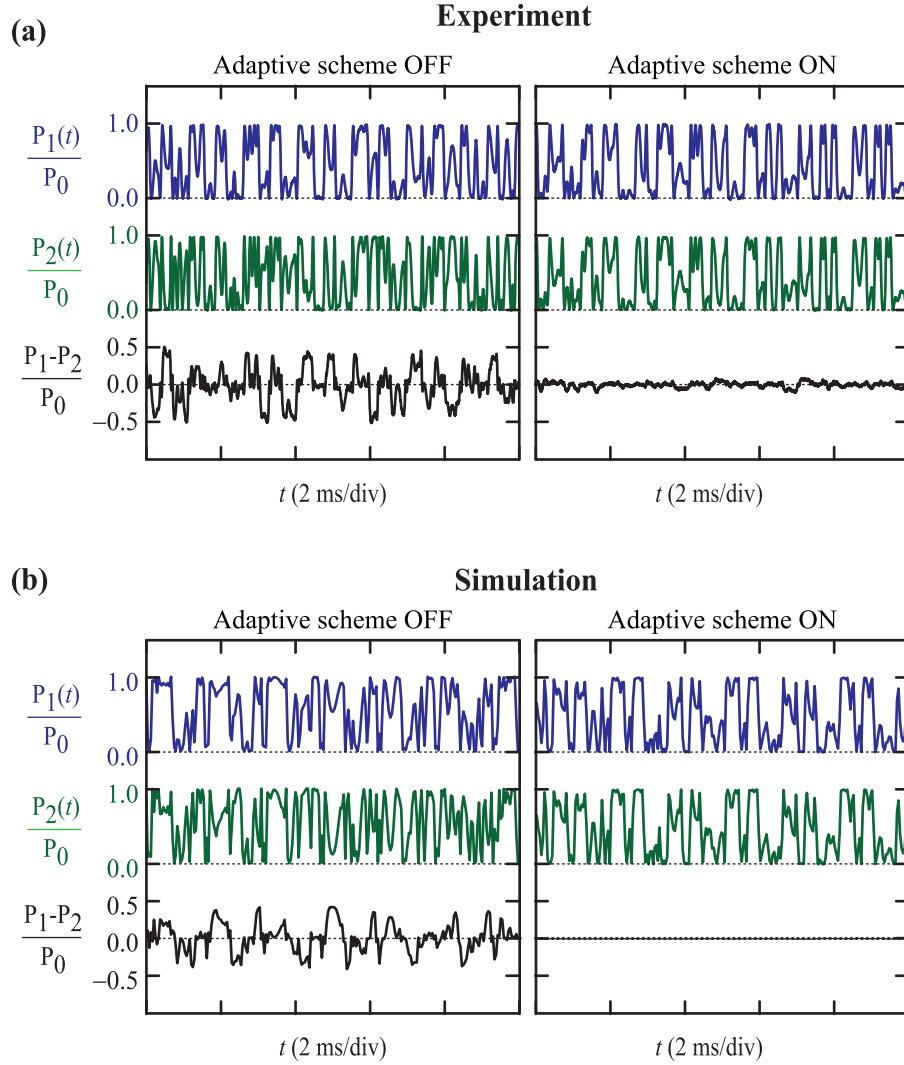


Figure 4.6: Synchronization of the transmitter and receiver dynamics using the adaptive scheme. (a) The left and right panels are 10 ms time traces of the internal dynamics $P_1(t)$ and $P_2(t)$ and the error signal $[P_1(t) - P_2(t)]$ corresponding to the time intervals shown in Fig. 4.5 (a). Under the same coupling conditions, the two loops only synchronize when the adaptive strategy is enabled. (b) Results from simulations corresponding to the time intervals shown in Fig. 4.5 (b).

feedback loops is poor as shown by the large difference signal $(P_1 - P_2)$. After $t = 0$, the adaptive algorithm is switched on. Now, the receiver forms a real-time estimate of the time-dependent coupling which is then used to compensate for the fluctuations in the coupling strength. The difference signal is immediately diminished showing the successful synchronization of the receiver to the transmitter dynamics. The calculated estimate of the channel variation $\bar{\kappa}(t)$ along with the actual variation $\kappa(t)$ is shown in the bottom panel of Fig. 4.5. To detail the dynamics of the feedback loops occurring at sub-millisecond time scales, we show in Fig. 4.6 (a), the measured optical signals of the two feedback loops for two 10-ms time windows, one where the adaptive scheme is off ($-440 \text{ ms} < t < 430 \text{ ms}$) and one where the adaptive scheme is enabled ($-60 \text{ ms} < t < 70 \text{ ms}$). In Figs. 4.5 (b) and Fig. 4.6 (b), we present simulation results which correspond to the experiments. The numerical simulations and the experimental results are seen to be in good agreement with each other.

Now that we have demonstrated the success of the adaptive strategy in maintaining network synchronization and tracking various coupling perturbations, we turn our attention to characterizing its operational efficacy. In order to evaluate the performance of the adaptive algorithm, we use the sinusoidal coupling strength modulation (Eqn. 4.15) introduced earlier. We characterize the performance of the adaptive algorithm as the strength ϵ and the speed f_m of the imposed fluctuation are varied. As a quantitative measure of the degree of synchronization, we define a normalized synchronization error θ as

$$\theta = \frac{[\langle (P_1 - P_2)^2 \rangle]^{1/2}}{P_0} \quad (4.16)$$

Here $\langle \bullet \rangle$ denotes an average over the available time-record. Note that this definition of the synchronization θ is slightly different from Eqn. 3.10. While the normalized feedback voltages $x_{1,2}$ were used to measure the synchronization error earlier, we use the optical power signals $P_{1,2}$ here. θ has a minimum value of zero when the two oscillators are identically synchronized and a maximum value of unity when P_1 and P_2 are uncorrelated. We measure θ as the modulation frequency f_m is varied, for different values of the modulation depth ϵ . Fig. 4.7 (a) shows the synchronization error θ calculated from the measured time-series for various modulation depths, $\epsilon = 0.05, 0.10, 0.20$, and 0.40 . Unavoidable mismatches in the experimental parameters of the two optoelectronic oscillators, such as feedback loop gain β and the MZM bias point ϕ_0 , prevent the value of θ from ever being zero. The minimum synchronization error attainable in experiments is about 4%. This level is identified in Fig. 4.7 (a) by a gray dashed line. From our observations, we can see that the adaptive strategy works successfully for small coupling fluctuations (up to a 20% deviation from the mean value κ_0) maintaining a 10% synchronization level for modulation frequencies f_m up to 150 Hz. For larger modulations ($\epsilon = 0.4$), this range is smaller. Fig. 4.7 (b) shows the θ obtained from numerical simulations which show a reasonable agreement with the experimental measurements. The simulations represent an ideal situation where the node parameters are identically matched. Consequently, for low modulation strengths and modulation frequencies θ down to nearly zero. We point out here that the adaptive dynamical equations presented earlier do not, strictly speaking, lead to a perfect estimation of the coupling strengths except when all the coupling elements K_{ij} are constant. This is because our derivation of

the adaptive strategy is based on the assumption that the coupling strength estimate can be treated as a constant in Eqn. 4.5 (Eqn. 4.9 for discrete-time).

In order to establish the efficacy of our adaptive algorithm, we compare the synchronization error measurements when the adaptive algorithm is enabled with those when it is turned off. In Fig. 4.8, we compare, for a modulation depth $\epsilon = 0.4$, the experimentally measured synchronization error θ with adaptation enabled and when it is disabled. At all frequencies observed, the adaptive technique yields an improvement in the degree of synchronization compared to the uncontrolled case, with the greatest improvement seen at lower frequencies. Numerical simulations (lower dashed line) of the adaptive synchronization method show the theoretically possible improvement in synchronization. These simulations are performed assuming perfectly matched dynamical oscillators and the absence of noise.

To quantify the degree of improvement due to the adaptive control algorithm, we define a figure of merit (FOM) as the ratio of the synchronization error with the adaptive algorithm disabled (θ_{OFF}) to that when it is enabled (θ_{ON}). A FOM value > 1 indicates that the adaptive algorithm improves the synchronization compared to the case when there is no adaptation. A higher value of the FOM indicates is desirable as it indicates a larger improvement. In Fig. 4.9 the FOM is plotted as a function of frequency for a modulation depth $\epsilon = 0.4$. We see that the adaptive algorithm performs consistently better in keeping the network synchronized. For low frequency fluctuations, the adaptive algorithm gives a three-fold improvement in the synchronization error.

Finally, we perform an evaluation of the ability of the adaptive technique to

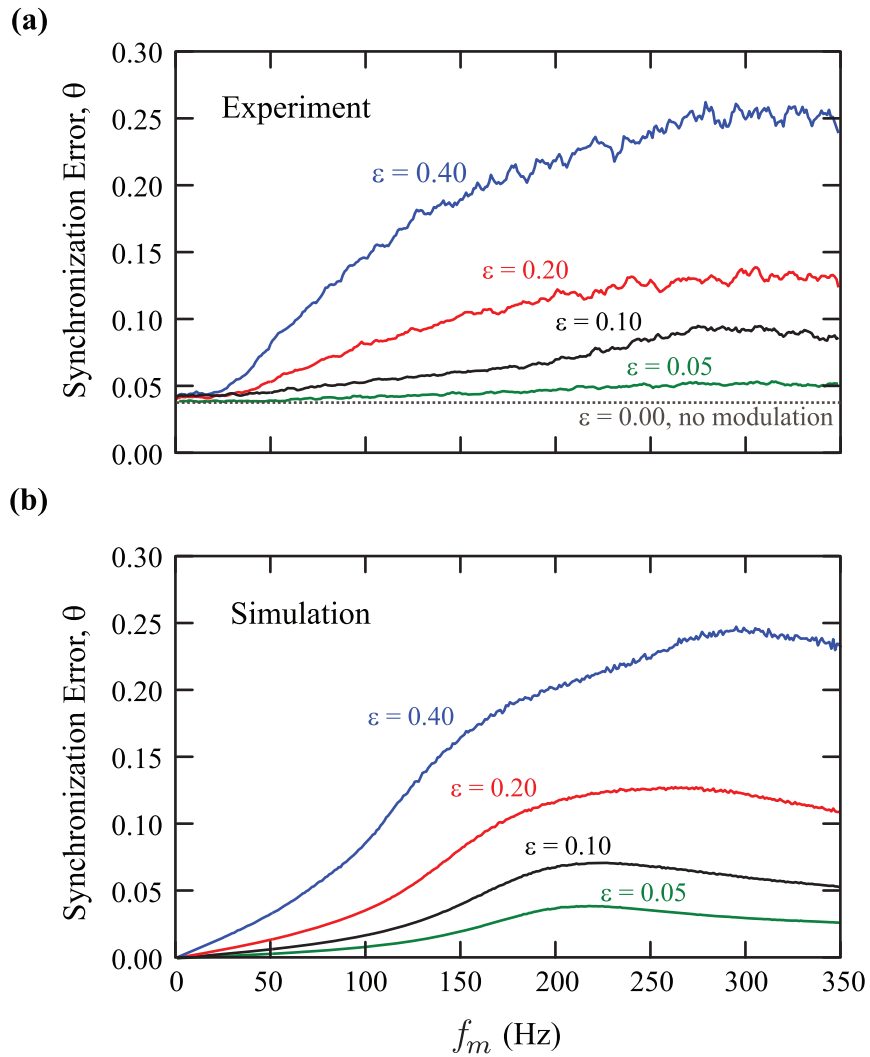


Figure 4.7: Synchronization error θ as a function of the modulation frequency f_m for various values of the modulation depth ϵ . (a) Results from experiments. (b) Results from numerical simulations.

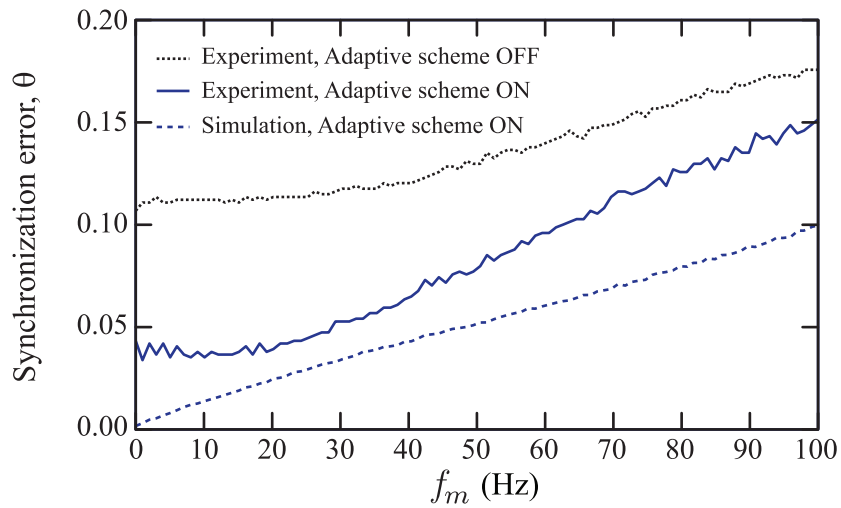


Figure 4.8: Synchronization error θ as a function of the modulation frequency f_m for a modulation depth $\epsilon = 0.40$. The experimentally measured synchronization error when the adaptive strategy is enabled (solid blue line) is lower than when the adaptive strategy is off (dotted line). Numerical simulations result in a smaller θ (dashed line) compared to the experimental observations.

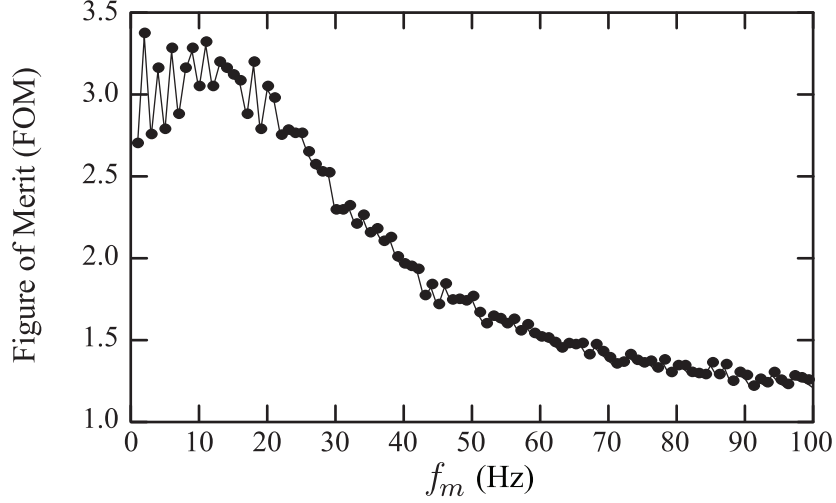


Figure 4.9: Figure of Merit (FOM) as a function of the modulation frequency f_m for modulation depth $\epsilon = 0.4$. FOM is defined as the ratio θ_{OFF}/θ_{ON} of the synchronization error with the adaptive strategy disabled to that when the strategy is enabled.

track coupling perturbations. To this end, we compare the tracking estimate $\bar{\kappa}$ with the actually imposed sinusoidal perturbation $\kappa(t)$. We define the tracking measure η as the ratio $\tilde{\bar{\kappa}}(f_m)/\tilde{\kappa}(f_m)$ of the Fourier amplitudes at the frequency f_m of the tracking estimate $\bar{\kappa}$ to that of κ expressed on a dB scale. A value of $\eta = 0$ dB is desirable as this would mean that the tracking signal has the same amplitude as that of the actual perturbation. The measure η allows us to characterize the tracking ability of the adaptation process independent of the synchronization properties of the network. This characterization helps us determine the limitations of the adaptive algorithm when used for sensing applications. For example, using the measure η , we can establish the speed of the perturbations that can successfully be tracked. In Fig. 4.10, we plot η as a function of the channel perturbation frequency f_m for various values of ϵ . Fig. 4.10 (a) shows the experimentally measured values while the

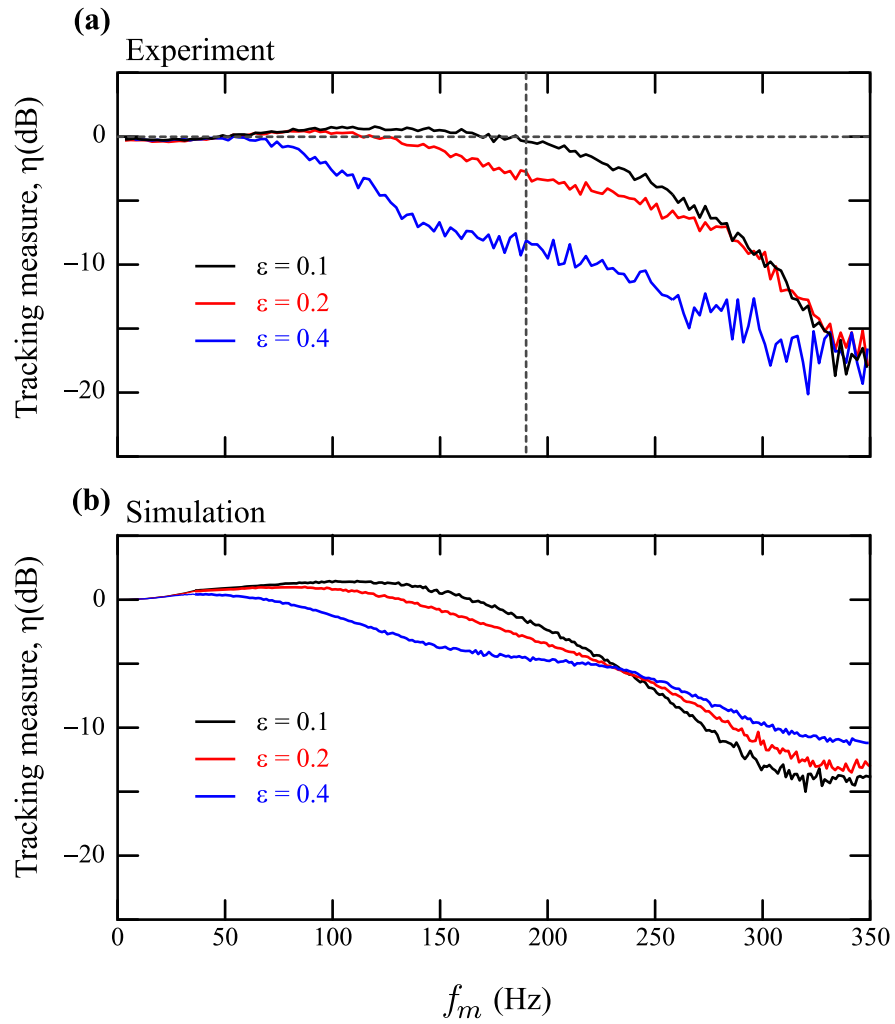


Figure 4.10: Tracking measure η as a function of the modulation frequency f_m .

numerical calculations are shown in Fig. 4.10 (b). Our experimental measurements are obtained using a network analyzer (Agilent 4395A). The horizontal dashed line in the figure identifies the 0 dB level, while the vertical dashed line identifies the frequency corresponding to the lowpass averaging process used in estimating $\bar{\kappa}$. For a low modulation strength $\epsilon = 0.1$, the tracking measure stays at 0 dB up to the lowpass filter frequency corresponding to z_0 . However, for larger modulations, the tracking measure starts deteriorating at a lower frequency.

4.4 Adaptive Synchronization: Three-node Network Experiments

In the preceding section, we presented results from an experimental implementation of the adaptive strategy on a pair of unidirectionally coupled optoelectronic systems. By implementing the adaptive algorithm the receiver system is able to compensate for coupling channel perturbations and remain synchronized with the transmitter. Even though this experiment illustrates the basic functioning of the adaptive algorithm, it does not fully capture the decentralized and distributed nature of the strategy. In this section, we present results from experiments on a network of three optoelectronic oscillators in which all the network nodes implement the adaptive strategy. These experiments demonstrate that a simple locally-applied control algorithm can track and compensate for simultaneous perturbations along multiple coupling channels in order to maintain global network synchrony.

Our experimental network is composed of three optoelectronic oscillators as depicted in Fig. 4.11 (a). The nodes are connected to each other through bidirec-

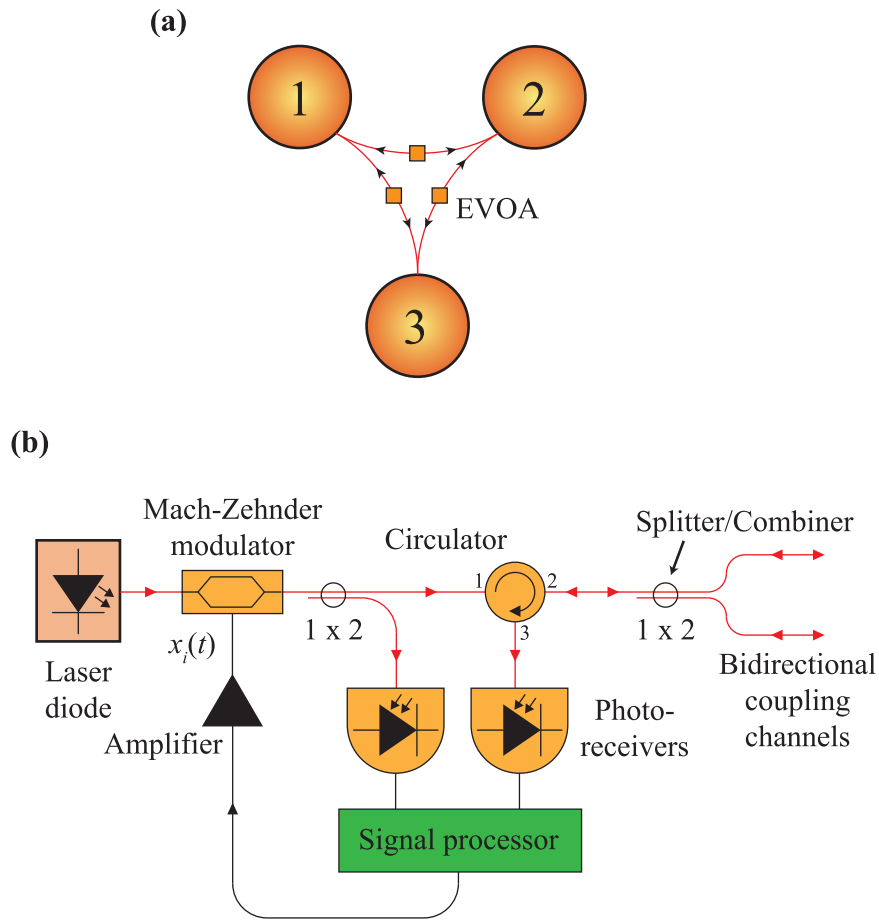


Figure 4.11: Experimental schematic of a network of 3 optoelectronic oscillators. (a) Each node of the network is coupled to the other two nodes through bidirectional optical coupling channels. The coupling strengths are symmetrical ($K_{ij} = K_{ji}$) and are controlled using electronically variable optical attenuators (EVOAs). (b) Schematic of each node of the network.

tional optical fibers. The coupling strengths between the nodes of the network are controlled by applying suitable voltages to electronically variable optical attenuators (EVOAs) placed in the coupling channels. In our experiments, we calibrate the links such that the coupling strengths are symmetric i.e. $K_{ij} = K_{ji}$. The implementation of the coupling is depicted in Fig. 4.11 (b). At each node i the optical output of the MZM is split into two equal components. While one half serves as the self-feedback signal, the other half is relayed to the remaining two nodes. In our network, bidirectional coupling over a fiber-optic channel is realized using an optical circulator. A circulator is a non-reciprocal three-port device that spatially separates the inbound and outbound optical signals. Fiber optic circulators act as signal routers, transmitting light from an input fiber to an output fiber, but directing light that enters along that output fiber to a third port. As shown in Fig. 4.11 (b) the transmitted signal from the node enters port 1 of the optical circulator and exits from port 2. The fiber coming out of port 2 is again split by a 50-50 optical splitter/combiner into two coupling channels which go to the other two nodes. The coupling channels also combine signals transmitted from the other two nodes in a 50-50 splitter/combiner before entering port 2 of the circulator. The combined signal exits through port 3 of the circulator and is detected by a second photoreceiver. The self-feedback and the received signals are then filtered by the DSP and then added to form the net feedback signal s_i . The DSP board at each node implements an adaptive scaling of s_i as discussed in Sec. 4.1 to compensate for unknown coupling fluctuations. The scaled signal serves as the modulation input to the MZM. The equations representing the dynamics of each node i , including

the adaptive strategy, are summarized below. The filter dynamics of the node i are described by the discrete-time equation

$$w_i[n] = -\sum_{l=1}^2 a_l w_i[n-l] + \beta \sum_{l=0}^2 b_l \cos^2(x_i[n-k-l] + \phi_0). \quad (4.17)$$

Here $w_i[n]$ denotes the output of the filter and x_i denotes the modulation signal to the MZM. x_i is obtained by scaling the net received signal $s_i[n] = \sum_{j=1}^N K_{ij} w_j[n]$ by an adaptive estimate \bar{k}_i of the total coupling into the node.

$$x_i[n] = \frac{1}{\bar{k}_i} s_i[n] \quad (4.18)$$

The scale factor \bar{k}_i is obtained from the equations

$$\begin{aligned} \bar{k}_i[n] &= \frac{P_i[n]}{Q_i[n]}, \\ P_i[n] &= z_0 P_i[n-1] + (1-z_0) s_i[n] w_i[n], \\ Q_i[n] &= z_0 Q_i[n-1] + (1-z_0) w_i^2[n]. \end{aligned} \quad (4.19)$$

In our experiments, the node parameters are set to the same values as for the two node experiment presented in the previous section. At each node, we observe the normalized input modulation voltage x_i and the adaptive scale factors \bar{k}_i using digital oscilloscopes (Tektronix TDS 7104, Agilent DSO7054A).

To demonstrate the effectiveness of the adaptive synchronization method, we begin by considering the case when one of the coupling coefficients in the network, K_{12} , changes abruptly. This situation is portrayed in Fig. 4.12. The network is initially tuned to achieve synchronization with $K_{13} = 0$, $K_{23} = 1.5$, and $K_{12} = 2.8$ by appropriately setting the scale factors \bar{k}_i . At $t = 0$, K_{12} is abruptly changed

to 1.3. This breaks the synchrony in the network, as shown by the large synchronization error, measured as the average of the pair-wise absolute differences $(|x_1 - x_2| + |x_2 - x_3| + |x_3 - x_1|) / 3$. This is expected, as our knowledge of the total incoming coupling into each node is no longer perfect and consequently the equations do not admit a synchronous solution. In Fig. 4.12(b), we explore the same situation, only now, we enable the adaptive algorithm. This allows that the scale factors \bar{k}_i to be estimated in real-time. After a short adjustment time following the sudden change of K_{12} at $t = 0$, we see that the synchronous state is rapidly restored. Further, from the tracking signals \bar{k}_i we can learn the individual coupling elements of the symmetric adjacency matrix K . This is possible by solving the linear equations

$$\begin{aligned}\bar{k}_1 &= K_{11} + K_{12} + K_{13}, \\ \bar{k}_2 &= K_{12} + K_{22} + K_{23}, \\ \bar{k}_3 &= K_{13} + K_{23} + K_{33}.\end{aligned}\tag{4.20}$$

In writing the above equations, we make use of the symmetric nature of the coupling matrix $K_{ij} = K_{ji}$. Recognizing that the self-feedback coupling strengths are taken to have the value 1 (see discussion following Eqn. 4.1) and are assumed to be immune to fluctuations and disturbances, allows us to solve the above equations to obtain an unique solution \bar{K}_{12} , \bar{K}_{23} and \bar{K}_{13} for the coupling coefficients. In the top panel of Fig. 4.12 (b), we show the calculated value of the coupling strength \bar{K}_{12} which is in good agreement with the actual variation.

In Fig. 4.13, we consider a case where all the coupling coefficients K_{12} , K_{23} ,

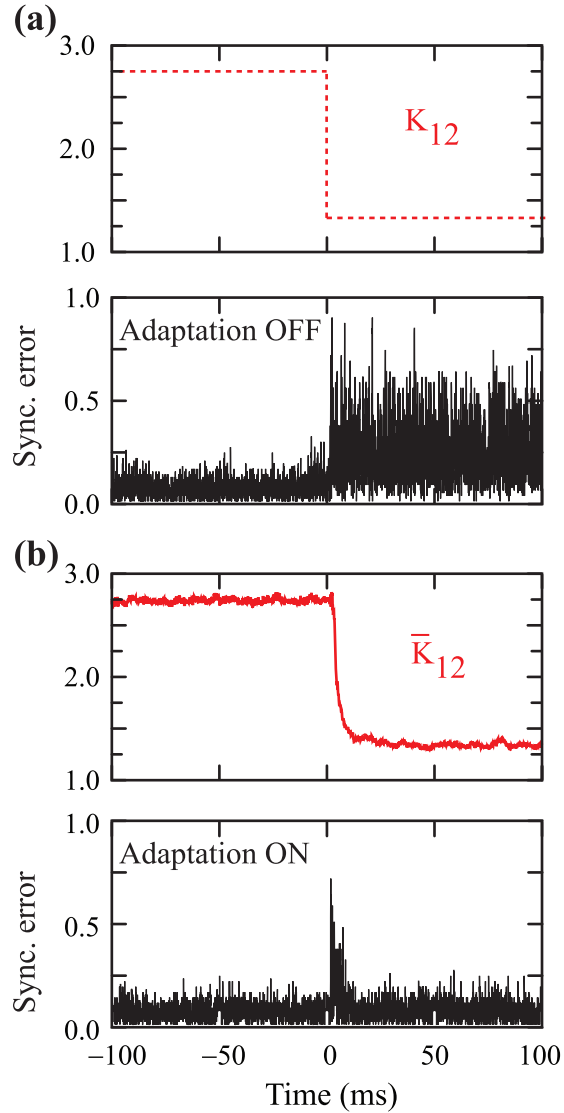


Figure 4.12: Maintenance of synchrony on a network of three optoelectronic oscillators. (a) The uncontrolled network is initially tuned to synchrony. At $t = 0$, the coupling strength K_{12} (top panel) is suddenly decreased to 1.3 causing the network to lose synchrony as is evidenced by the large synchronization error (shown in bottom panel). (b) The same situation as described in (a) is explored except this time the adaptive control is enabled. Global synchrony is maintained despite the sudden change in coupling strength. The estimate \bar{K}_{12} is shown in the top panel.

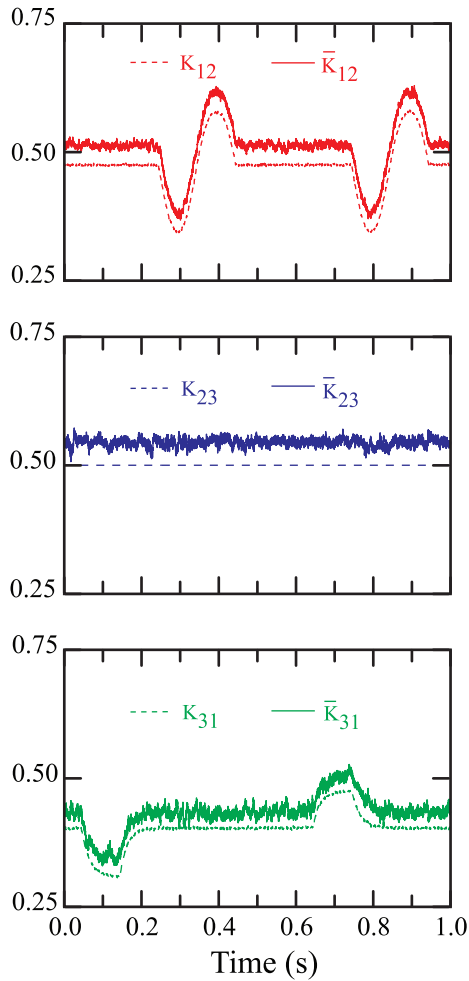


Figure 4.13: Adaptive tracking of multiple simultaneous perturbations. The bidirectional coupling strengths K_{12} , K_{23} , and, K_{31} (shown as dashed lines) are simultaneously varied. The adaptive algorithm successfully estimates (shown as solid lines) all the coupling elements in the network. The estimates are artificially raised by 0.05 to make the dashed lines visible.

and K_{13} are non-zero and both K_{12} and K_{13} are simultaneously time-varying. We see that the adaptive algorithm maintains global synchrony in this case as well and independently tracks the perturbations to each coupling channel. The dashed lines show the actual variations imposed on the coupling channels and the solid lines represent the calculated estimates. In the figure, we artificially shifted the solid lines upward by 0.05 to more easily distinguish the (otherwise superposed) curves.

The ability of the adaptive algorithm to obtain estimates \bar{K}_{ij} of the elements of the coupling matrix may find potential use in sensing applications. In situations where the coupling strength fluctuations are caused by environmental changes, estimating the temporal changes may be used as a means of sensing these changes. The sensing technique presented here is for three nodes. In large networks, the number of links can exceed the number of nodes. Even though simulations show that our adaptive technique still maintains global synchrony in this case [68], the information available through the tracking signals \bar{k}_i may no longer be sufficient to deduce the actual variations in the individual coupling links. Nonetheless, the strategy could still be used in sparsely connected networks with fewer links or when partial information about the links is available (e.g., if not all the links are simultaneously perturbed). The experiment presented here can be considered a proof-of-principle test for the application of coupled dynamical systems as a sensor network. In this prototype system, the nodes act collectively to learn about specific changes in their environment. The control signals \bar{k}_i , which maintain synchrony in the network, also contain practical information used to sense what occurs between the nodes. Depending on the setting, the couplings could be arranged to be in free-space rather

than with fiber-optic cables or could use RF transmitter and receiver antennas.

4.5 Summary

In this chapter, we introduced an adaptive technique designed to maintain global synchronization in a network of chaotic oscillators even when the couplings are unknown and time-varying. We discussed the implementation of this scheme on networks composed of two and three optoelectronic oscillators and presented experimental measurements that demonstrate the success of the strategy. Besides maintaining synchrony by compensating for any external coupling perturbations, the adaptive algorithm also tracks the coupling variations, thus opening up the possibility for sensing applications.

Chapter 5

Optimal Network Topologies for Synchronization ¹

Thus far we have focused our discussion on the maintenance of synchrony in a network of chaotic oscillators when the coupling coefficients change in an *a priori* unknown fashion. We now turn our attention to study of the interplay between network structure and dynamics with a focus on synchronized behavior. In this chapter, we address the specific question of how the network structure influences the readiness with which a given network attains synchronization also called *synchronizability*. Connection topology has a strong influence on the dynamical behavior of complex systems. Spreading of epidemics [69–72], cascades of systemic failures [73], communication-network traffic flows [74], emergence of collective behavior [75–77], design of communication networks, synchronized firing of neurons [78–80] are some examples of complex network problems where connection topology has a critical influence. In many of these cases, such as in the design of communication networks, power-grid systems, and in understanding the behavior of neuronal systems, synchronization plays a crucial role. For efficient design of networks suited for these applications, it is essential to understand the influence of network structure on synchronization. Though there have been many theoretical investigations in this direction, experimental studies of the influence of structure on the synchronization properties of networks have largely been lacking. The work presented here strives

¹The results presented in this chapter have also been presented in Ref. [42]

to bridge this gap.

In Sec. 5.1, we briefly review various theoretical investigations aimed at characterizing the synchronizability of a given network.

Sec. 5.2 gives the details of our experimental network of four optoelectronic oscillators with an easily configurable connection topology. Using this flexible network, we experimentally study the effect of network topology on synchronization properties.

In Sec. 5.3, we discuss a measure of synchronizability proposed in Ref. [41]. We discuss how this measure depends on the structure of a given network of dynamical oscillators. Based on this measure, we identify network configurations that are optimal for synchronization applications.

Sec. 5.4 reports experimental measurements, from the 4-node network, relating the convergence rate of a network to global synchrony with the network structure. From our measurements, we show that having more links does not necessarily imply a faster convergence to synchrony, as is generally thought. We also present simulation results that extend the applicability of the discussed methods to larger networks. Some results presented in this section of the thesis have also been published in Ref. [42].

In Sec. 5.5, we discuss how two different networks having the same number nodes and links but different connection geometry, can display qualitatively different transients to synchrony. We find that, in this case, the nature of the transient is determined by the eigenvector properties of the coupling matrix associated with the network.

Sec. 5.6 summarizes the topics presented in the chapter.

5.1 Synchronizability of a Network: Past Research

The master stability function approach, discussed in Sec. 3.3, was perhaps the first step taken towards a systematic analysis of the influence of network topology on network dynamics. By decoupling the node dynamics from network structure, the MSF provides us with an efficient means to predict if a given network exhibits stable synchronous behavior or not. If all the eigenvalues corresponding to the modes transverse to the synchronization manifold, $\{\lambda_2, \lambda_3, \dots, \lambda_N\}$, of the Laplacian coupling matrix \mathbf{L} fall within the region of stability as determined by the MSF, then the network exhibits stable synchronous behavior². Here, the region of stability corresponds to the domain of complex numbers where the MSF takes a negative value. We point out again that an extension of the standard MSF theory (which is derived based on the assumption that \mathbf{L} is diagonalizable) allows us to identify a region of stability even when the coupling matrix is nondiagonalizable [57]. Motivated by the MSF analysis, it has been hypothesized that the more easily the eigenvalues of the coupling matrix fall in the stability region, the easier the network synchronizes *i.e.* the higher the synchronizability of the network. When the stability region as determined by the MSF is unbounded (assumed to be along the positive real axis, which is usually the case), the synchronizability of the network can be measured by the smallest eigenvalue λ_2 . In this case, if the smallest eigenvalue falls in the stability

²Note that $\lambda_1 = 0$ owing to the zero row-sum property of the Laplacian matrix [58] and corresponds to evolution along the synchronization manifold.

region, the other eigenvalues are guaranteed to lie in the stable region as well. On the other hand, when the region of stability as predicted by the MSF is bounded, as it is for the coupled optoelectronic systems considered here, the ratio λ_N/λ_2 of the largest nonzero eigenvalue λ_N to the smallest nonzero eigenvalue of the Laplacian matrix λ_2 , determines the synchronizability of the network [34]. The smaller the ratio of the eigenvalues the higher is the synchronizability. This is because a smaller eigenvalue ratio λ_N/λ_2 implies that the set of eigenvalues are closely spaced, thereby increasing the ease with which they fall in the region of stability. Recently, another measure of the synchronizability, also reliant on the spectral properties of the Laplacian matrix, has been proposed [41]. We adopt this measure in our network experiments. The discussion of this measure will be deferred to Sec. 5.3, where we present detailed calculations of this measure for several different network topologies.

Apart from techniques based on the spectral properties of the coupling matrix, other methods to analyze the synchronizability of networks have been proposed. In Refs. [34,35], the ability of a given network to synchronize was related to the average node-to-node distance. In Ref. [36], the clustering coefficient was used as a measure of network synchronizability while in Ref. [37] the degree distribution was used to characterize it. Finally, in Refs. [38–40], the weight distribution of the network was used to measure synchronizability. As pointed out earlier, all these investigations of the influence of network structure on synchronization properties of a network have been theoretical. In what follows in this chapter, we present what is perhaps the first systematic experimental investigation of the interplay between coupling structure and network dynamics.

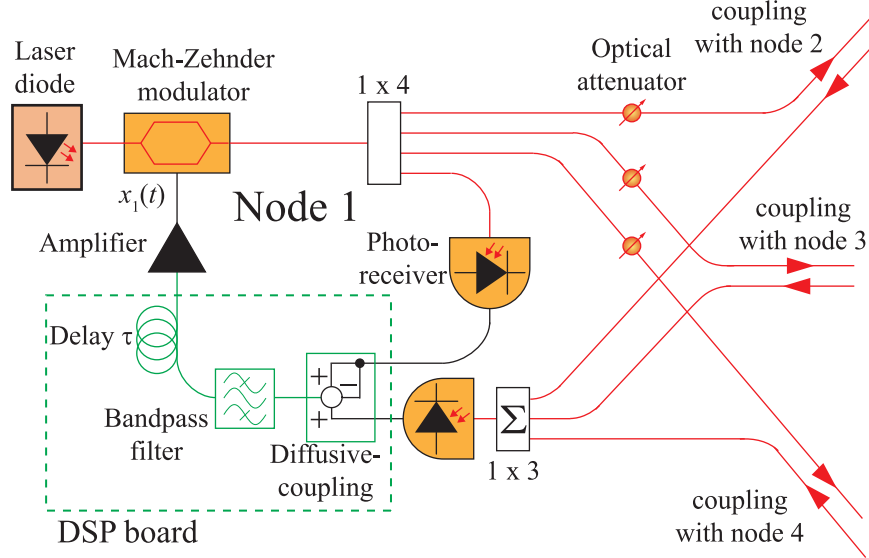


Figure 5.1: Experimental schematic of an optoelectronic node in a 4-node network. Optical attenuators are used to either enable or disable any given network link allowing us to configure the network topology.

5.2 Experimental Setup: Four-node Network

Our experimental setup consists of a network of $N = 4$ optoelectronic oscillators of the type discussed in Chapter 2. The construction of each node in the network is illustrated in Fig. 5.1 in the form of an experimental schematic. The nodes are coupled optically by splitting the output of the MZM into four equal signals and while one of these signals serves as the self-feedback signal, the other 3 signals are relayed to the remaining three nodes through optical fibers. The coupling strengths in the network are controlled using electronically variable optical attenuators. Unlike the case of the 3-node network, a circulator is not used here because we have independently controlled channels rather than shared bidirectional fibers. In our experiments, we set all the coupling strengths to be equal to the feedback strength

(normalized to be 1), effectively creating a binary network. Then, using the optical attenuators, a link can either be enabled or disabled allowing us to arbitrarily control the network topology. Each node also has a 3×1 optical combiner which receives the cumulative optical coupling signal from the other nodes. Both the self-feedback and the received signals are photodetected and the resulting electric signals are processed by the DSP board, to implement bandpass filtering, time-delay and diffusive coupling operations. Using digital oscilloscopes, we record the modulation voltages $x_i(t)$ input to the MZM at each node. The equations describing the dynamics of node i as represented in continuous-time are

$$\begin{aligned} \frac{d\mathbf{u}_i}{dt} &= \mathbf{A}\mathbf{u}_i(t) + \mathbf{B}\beta \cos^2(x_i(t - \tau) + \phi_0), \\ w_i(t) &= \mathbf{C}\mathbf{u}_i(t), \\ x_i(t) &= w_i(t) + \frac{\varepsilon}{d} \sum_{j=1}^N L_{ij} w_j(t). \end{aligned} \quad (5.1)$$

Here the coupling topology is represented by the Laplacian matrix \mathbf{L} as discussed earlier. The off-diagonal elements L_{ij} of the Laplacian matrix are equal to 1 if there exists a link from node j to node i and 0 otherwise. The diagonal elements L_{ii} are equal to the negative of the net number of links coming into each node i , i.e. $L_{ii} = -\sum_{j \neq i}^N L_{ij}$. Note that the total number of links in the network, m , is given by the negative of the sum of the diagonal elements of \mathbf{L} , i.e. $m \equiv -\sum_{i=1}^N L_{ii} = -\mathbf{Tr}(\mathbf{L})$. ε denotes a global coupling strength which is normalized by the average number of links per node in the network $d \equiv m/N$. This normalization of ε by d ensures that, in comparing the properties of coupling configurations with different number of links, the total coupling in the network, $(\varepsilon m/d)$, remains the same. Put differently, it

allows us to investigate the effect of different ways of distributing a given amount of coupling on the synchronization properties of the network.

The parameters of all the feedback loops are set to be nominally identical. For each loop, the feedback strength is set to be $\beta = 3.6$ and the feedback delay is programmed to be $\tau = 1.5$ ms. The highpass and lowpass filter corner frequencies are set to $f_H = 100$ Hz and $f_L = 2.5$ kHz respectively and the modulator bias is adjusted to be $\phi_0 = -\pi/4$.

5.3 Optimal Network Configurations for Synchrony

In Ref. [41], Nishikawa and Motter developed a theoretical framework to identify coupling configurations that are optimal for the attainment of synchronization in a network of N dynamical oscillators. By measuring network synchronizability as the spread of the non-zero eigenvalues of the Laplacian coupling matrix,

$$\sigma^2 = \frac{1}{d^2(N-1)} \sum_{i=2}^N |\lambda_i - \bar{\lambda}|^2, \text{ where } \bar{\lambda} \equiv \frac{\sum_{i=2}^N \lambda_i}{(N-1)}, \quad (5.2)$$

they were able to predict that synchronizability does not depend monotonically on the number of links m in a network as is generally thought. In the above expression $\Lambda = \{0, \lambda_2, \dots, \lambda_N\}$ denote the set of eigenvalues of the Laplacian matrix \mathbf{L} . The definition of σ as a measure of synchronizability of a given network draws its motivation from the MSF formulation. The idea is that the more bunched-up the eigenvalues of the Laplacian matrix are, the easier it is to place them in the region of stability as specified by the MSF by varying the global coupling strength ε (which proportionally scales all the eigenvalues together). Thus, a smaller value of σ implies

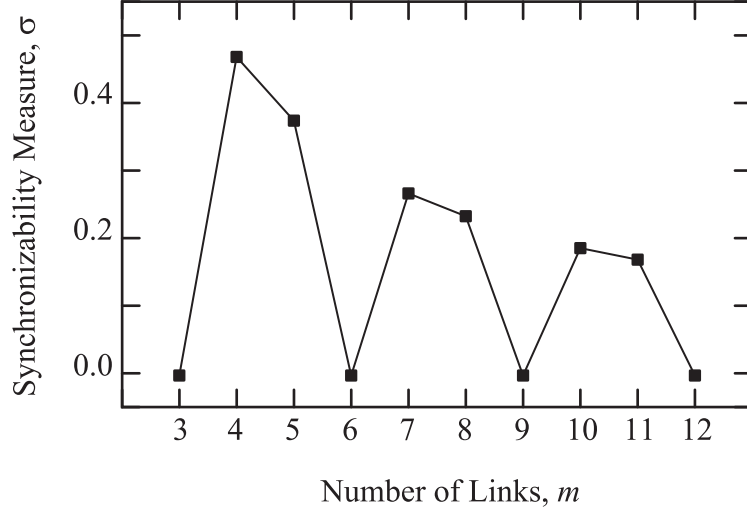


Figure 5.2: Synchronizability measure σ as a function of the number of network links m for a 4-node network.

a higher synchronizability of the network. For oscillators with an unbounded region of stability, minimization of σ corresponds to a minimization of the coupling strength ε required to achieve synchrony (also known as coupling cost). For oscillators with a bounded region of stability, minimization of σ corresponds to maximization of the range of ε for which synchrony is stable. It has also been postulated in Ref. [41] that the minimization of σ also ensures the fastest exponential convergence to synchronization. In order to experimentally verify this claim, we measure here the rate of convergence to synchronization for various network topologies.

Among all possible network configurations with N nodes and m links, it was shown in Ref. [41] that the minimum value of σ that can be achieved is given by the expression

$$\sigma_{min}(m) = \frac{1}{(N-1)d} \sqrt{(m - q_k)(q_{k+1} - m)}, \quad (5.3)$$

where $q_k \equiv k(N - 1)$, $k = 1, 2, \dots, N$. From the above expression, we can see that $\sigma_{min} = 0$ only when $m = q_k$ or $m = q_{k+1}$ i.e. when the number of links in the network is a multiple of $(N - 1)$. This is the absolute minimum possible value of σ and networks with this property are termed as *optimal networks*. We point out that in general there may be configurations with $m = q_k$ that do not minimize σ . However, $\sigma = 0$ does imply that $m = q_k$. Optimal network configurations are expected to have the best synchronization properties (fastest rate to convergence, largest synchronization range of ε , minimum coupling cost etc. . .). Network configurations with $q_k < m < q_{k+1}$, but a minimal eigenvalue spread as given by Eqn. 5.3 are called *suboptimal* networks. All other networks are termed *nonoptimal*. In Fig. 5.2 we plot the minimum value of σ as a function of the network links m for networks with $N = 4$. As is evident from the figure, the eigenvalue spread shows a pronounced non-monotonicity with respect to the number of network links m . Fig. 5.3 shows the sequence of optimal and suboptimal network configurations corresponding to the values of eigenvalue spread shown in Fig. 5.2. In our experiments, we measure the rate of convergence to synchrony for these configurations.

5.4 Experimental Measurements of Optimality

To measure the convergence rate to synchrony μ for a given network, we adopt the method described in Sec. 3.2. We start with an initially uncoupled network with all the couplings disabled. This is achieved by setting the global coupling strength $\varepsilon = 0$. Under these conditions, the oscillators are completely decoupled and hence

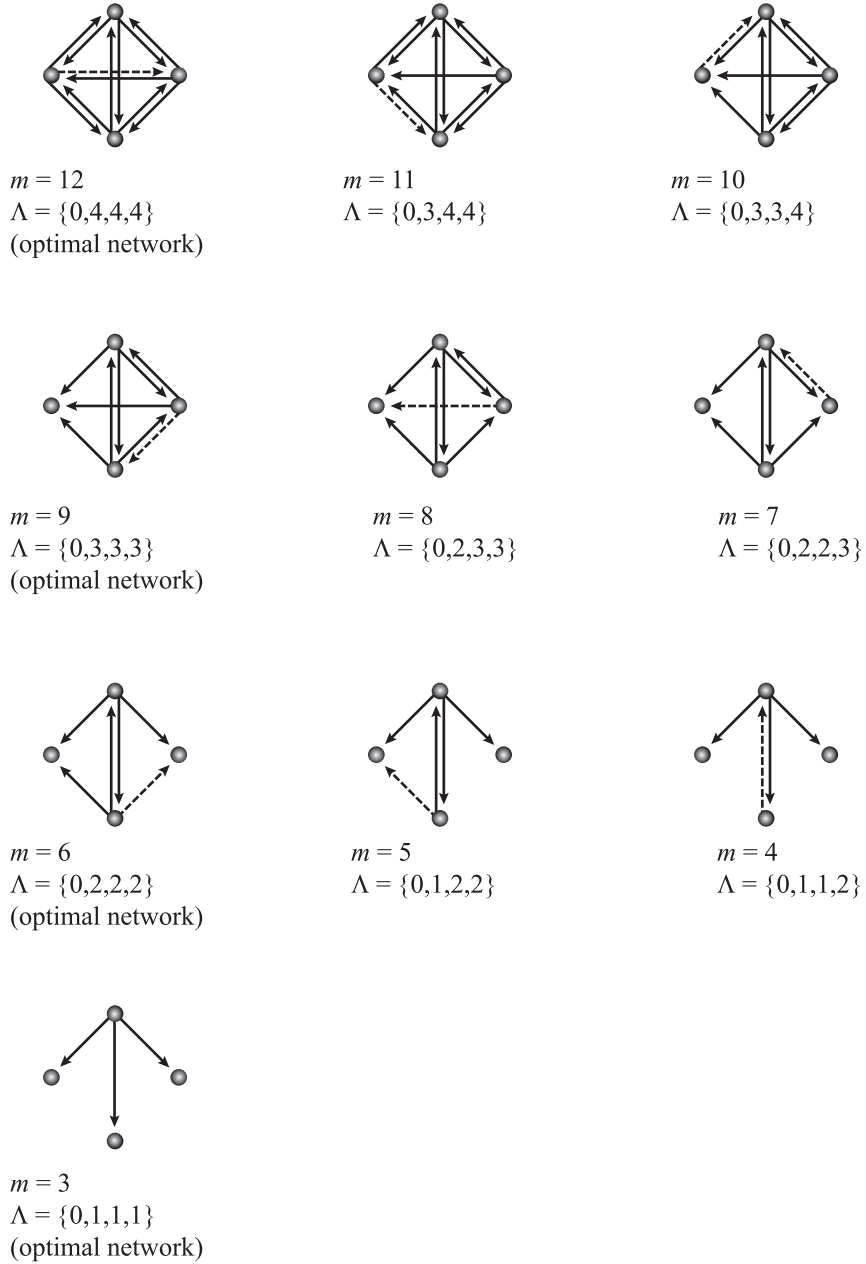


Figure 5.3: A path of optimal and suboptimal configurations from a fully connected network with $m = 12$ links to an optimal tree network with $m = 3$ links. At each step we remove a link (indicated by a dashed line) such that σ is decreased or minimally increased. We experimentally measure the rate of convergence to synchrony for these network configurations. The eigenvalues of the coupling matrix corresponding to each configuration are also shown.

uncorrelated. At some specific instant of time ($t = 0$), selected coupling links are simultaneously enabled by switching ε to 0.7. With the coupling enabled, the synchronization error, defined as,

$$\theta(t) \equiv \frac{1}{N(N-1)} \sum_{i,j} |x_i(t) - x_j(t)|, \quad (5.4)$$

is expected to ideally approach zero. However, for real networks that synchronize, the effect of noise and parameter mismatches means that θ approaches a synchronization floor θ_0 . Note that the above definition of θ measures the degree of network synchronization as a function of time t , in contrast with Eqns. 3.10 and 4.16 which measure the asymptotic degree of synchrony. The rate of convergence to synchrony is measured as the exponent μ of the exponential decay of θ to θ_0 , $(\theta - \theta_0) \sim \exp(-\mu t)$. Fig. 5.4 presents the measured convergence rates for the optimal and suboptimal configurations shown in Fig. 5.3. We note that for all these configurations, the effective coupling strength ε/d changes when the number of links is increased/decreased so that a network with fewer links also has stronger links. In order to avoid problems with zero crossings of $[x_i(t) - x_j(t)]$, we perform a moving-window boxcar average of $\theta(t)$ over a small time window to obtain $\langle \theta(t) \rangle$. To measure μ , we fit $\langle \theta(t) \rangle$ to an exponential function over a fixed time interval from 0.5 ms to 2.0 ms. We avoid starting our fit at $t = 0$ to eliminate the artificial influence of the boxcar averaging. Under these conditions the measured convergence rate is found to be independent of the smoothing window size. We carry out the measurement process, as described above, for 100 different realizations to obtain the mean value of μ , denoted as $\bar{\mu}$. The standard deviations for our measurements, also shown in the figure as bars, in-

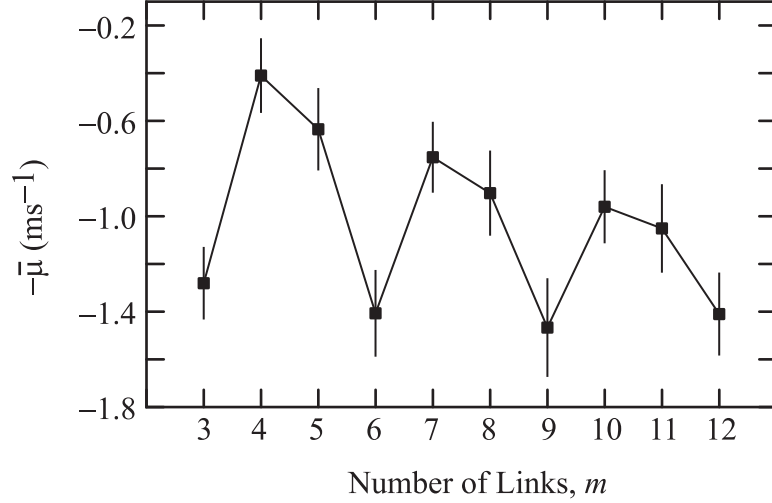


Figure 5.4: Convergence rate to synchronization $\bar{\mu}$ measured for the set of optimal and suboptimal configurations shown in Fig. 5.3.

indicate only a small variability across different realizations. As predicted in Ref. [41], the trend of our measurements of the convergence rate corresponds well with the eigenvalue spread σ (shown in Fig. 5.2). The mean convergence rate shows a marked non-monotonicity with respect to the number of network links, m . The rate of convergence is found to be fastest for optimal networks with $m = k(N - 1)$. From our results, we can conclusively say that having more links in a network does not necessarily imply better synchronization properties. Rather, by engineering the coupling topology to have the maximal synchronizability (minimum eigenvalue spread $\sigma = 0$) we can attain with fewer network links, the same convergence rate as in the extreme case of a fully connected network.

Next, we investigate whether the experimental results obtained from the 4-node network are scalable to larger networks. Using Eqns. 5.1, we numerically measure μ for various optimal and suboptimal configurations of a 50-node network as the

number of links m is varied. Again, our statistics are obtained from 100 different realizations of initial conditions. The results from our simulations are shown in Fig. 5.5. We start with a fully connected network configuration with $m = 50 \times 49 = 2450$ links. We successively remove links from the fully connected network, ensuring that for each step the eigenvalue spread σ is minimized. Fig. 5.5 (a) shows the calculated value of σ for these configurations. The results from our numerical measurement of μ are presented in Fig. 5.5 (b). We clearly see the predicted non-monotonic trend, with the rate of convergence being maximal for optimal configurations for which the number of links is a multiple of $(N - 1) = 49$ and the eigenvalue spread $\sigma = 0$.

We analyze further the influence of network topology on synchronization by looking at yet another synchronization property: the range of ε for which the global synchronous solution is stable. We denote this quantity as ρ . We infer ρ from an experimental measurement of the MSF. Our measurement of the MSF is accomplished using a two-node network. For a two-node network, the Laplacian coupling matrix has only two eigenvalues, $\{\lambda_1, \lambda_2\}$ of which $\lambda_1 = 0$ due to the zero row-sum property of \mathbf{L} . The free eigenvalue λ_2 can easily be varied along the real axis by controlling the coupling strength ε . For each value of the coupling strength ε , we measure the converge rate to synchronization μ as described before. The value $-\mu$ is the maximal transverse Lyapunov exponent which directly corresponds to the MSF. In Fig. 5.6, we present a measurement of the MSF along the real axis as a function of the eigenvalue scaled by ε/d . A disadvantage of using the convergence based measurement process described above is that the positive-valued part of the MSF cannot be determined which makes the identification of the stability bounds (the

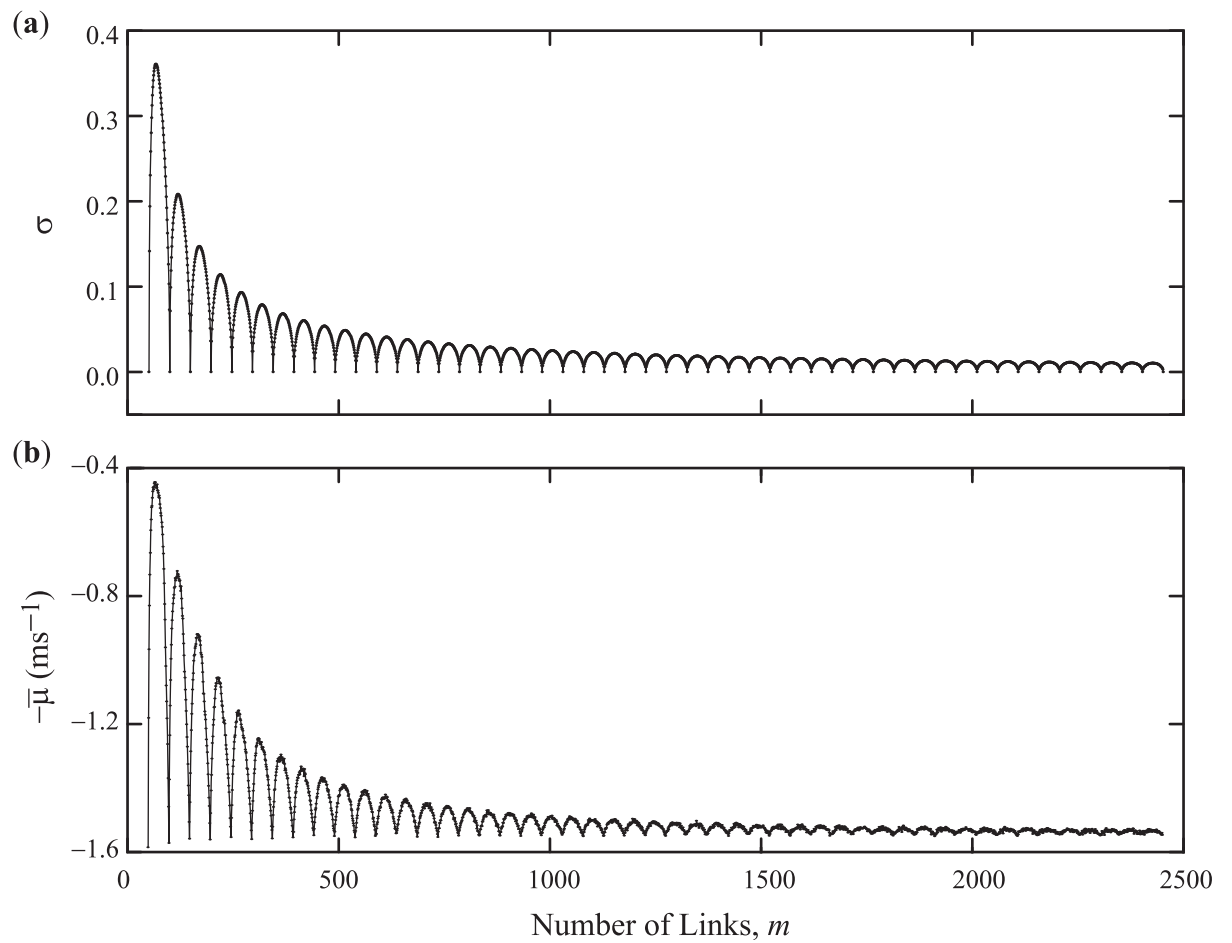


Figure 5.5: Numerical measurement of convergence rate of optimal and suboptimal configurations of a 50-node network. (a) Synchronizability measure σ as a function of the number of network links m . (b) Mean convergence rate $\bar{\mu}$ obtained from 100 independent measurements of μ for the network configurations corresponding to the synchronizability values shown in (a).

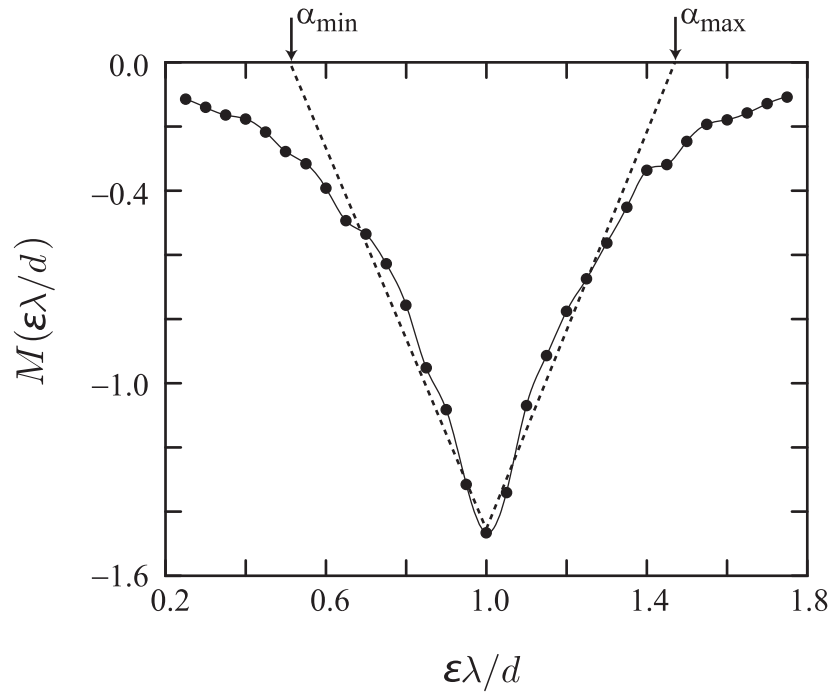


Figure 5.6: A measurement of the MSF along the real axis is accomplished by measuring the rate of convergence to synchronization of a symmetric bidirectionally coupled network of two optoelectronic oscillators as the coupling strength ϵ is varied. The solid dots show the measured data points. The dotted curve is a piecewise linear fit to the MSF in the interval $\epsilon\lambda/d \in [0.5, 1.5]$. The stability bounds are indicated by vertical arrows.

points at which the MSF changes sign) difficult. We circumvent this problem by using a piecewise-linear fit (shown in Fig. 5.6 as dashed lines) to our MSF. By determining the eigenvalues where the linear-fit changes sign, we can identify the region of stability as the range $[\alpha_{\min}, \alpha_{\max}] = [0.51, 1.47]$. Thus, for any given network of optoelectronic oscillators to synchronize, it is imperative for the scaled eigenvalues of the corresponding Laplacian matrix to lie within this range. Using the stability bounds determined from the MSF, we can now infer ρ as

$$\rho \equiv \varepsilon_{\max} - \varepsilon_{\min} = \frac{\alpha_{\max}d}{\lambda_N} - \frac{\alpha_{\min}d}{\lambda_2} \quad (5.5)$$

where λ_N and λ_2 denote the largest and smallest non-zero eigenvalues of the Laplacian matrix, and ε_{max} and ε_{min} denote the maximum and minimum values of ε for which the network synchronizes. Fig. 5.7 presents the inferred value of the stability range ρ as a function of the number of links m for the 4-node network configurations shown in Fig. 5.3. From the results, we see that the stability range is maximal for the optimal networks as is expected.

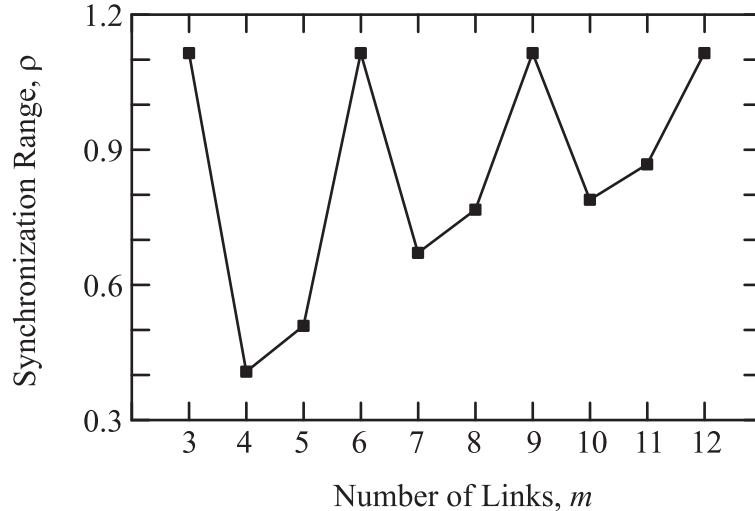


Figure 5.7: Synchronization range ρ , inferred from the measured MSF, as a function of the number of network links m .

5.5 Influence of Connection Geometry

In the preceding section, we discussed the influence of the number of network links m on the synchronization properties of a network. But does the synchronizability measure σ completely characterize the synchronization properties of a network, especially the rate of convergence to synchrony? The theoretical answer to this question is yes because the asymptotic properties of the convergence transient to synchrony are completely determined by the eigenvalues of the Laplacian matrix [41]. However, in practice, a finite synchronization error floor limits our ability to observe convergence arbitrarily close to the synchronous manifold. Thus for real networks, the initial transients soon after the coupling is enabled, play a crucial role in determining the nature of convergence to synchrony. In these situations, we find that the convergence properties, in addition to being dependent on the eigenvalues,

are also influenced by the eigenvectors of the coupling matrix.

The network configurations (shown in Fig. 5.3) considered for our convergence rate measurements were chosen such that the coupling matrix \mathbf{L} is diagonalizable. However, coupling matrices of general directed networks are not always diagonalizable. In fact, there exist many coupling matrices with the same eigenvalue spectra (co-spectral graphs), that are nondiagonalizable i.e. their eigenvectors are not linearly independent. Mathematically, the diagonalizability of a matrix can be characterized by its geometric degeneracy, g_d . Geometric degeneracy is defined as the largest number of repeated eigenvalues of the coupling matrix associated with the same degenerate eigenvector. A matrix is said to be diagonalizable if it has $g_d = 1$, i.e. when all the eigenvectors are linearly independent. In Fig. 5.8, we show all the 4-node optimal networks with $m = 3$ links identified by their geometric degeneracies. Of these networks, only the star configuration has a coupling matrix that is diagonalizable. In Fig. 5.9 we show all 4-node optimal and sub-optimal network configurations with the same eigenvalue spectra but have different eigenvector properties characterized by their geometric degeneracies.

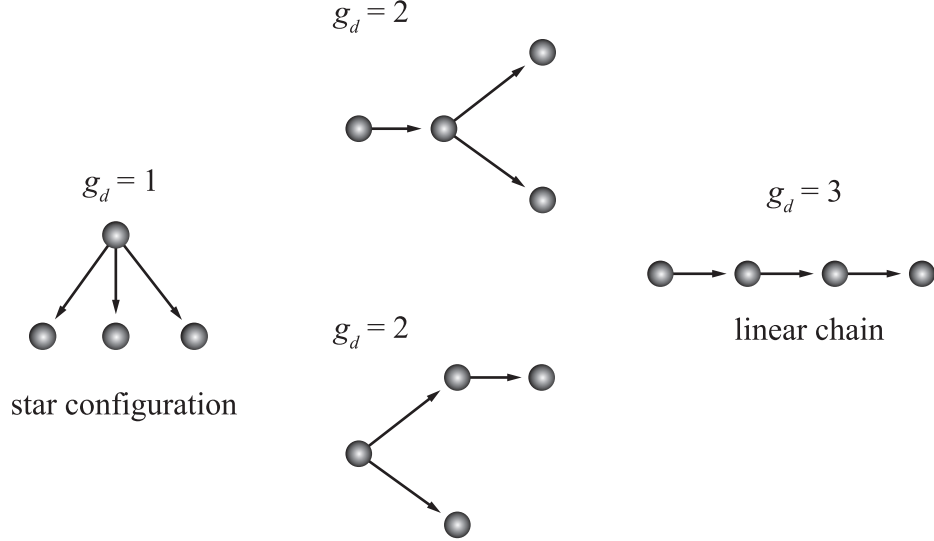


Figure 5.8: Optimal configurations with $m = 3$ for the 4-node network. The associated coupling matrices for all the configurations shown above have the same eigenvalue spectrum. However, only the star configuration ($g_d = 1$) has a diagonalizable coupling matrix.

Going by just the synchronizability measure σ , we expect the diagonalizable star network ($g_d = 1$) and the non-diagonalizable linear chain ($g_d = 3$) (shown in Fig. 5.8), to have the same convergence properties to synchrony. Fig. 5.10 compares the approach to synchrony for both configurations. Fig. 5.10 (a) shows results from experiments while Fig. 5.10 (b) shows numerical results obtained by simulating Eqns. 5.1. In order to accurately mimic experimental conditions, we impose a 1% mismatch in the self-feedback strengths of the nodes and coupling strengths. Further, to model digitization error from our oscilloscope measurements, we added a Gaussian noise term with zero mean and a standard deviation of 0.06, to our numerical simulations. We performed 100 independent measurements of $\langle \theta(t) \rangle$ starting with different initial conditions for both networks. As is evident from the measure-


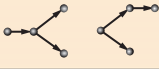
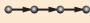


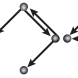
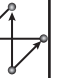





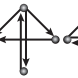
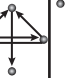

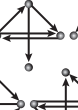




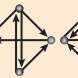

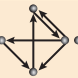


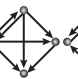
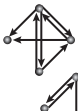


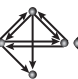



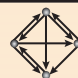
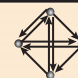
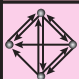


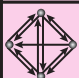

m	Geometric degeneracy			Λ	
	$g_d = 1$	$g_d = 2$	$g_d = 3$		
3				{0,1,1,1}	optimal
4	   	  		{0,1,1,2}	suboptimal
5	   	  		{0,1,2,2}	suboptimal
6		  	 	{0,2,2,2}	optimal
7	  	 		{0,2,2,3}	suboptimal
8	 	 		{0,2,3,3}	suboptimal
9				{0,3,3,3}	optimal
10	 			{0,3,3,4}	suboptimal
11				{0,3,4,4}	suboptimal
12				{0,4,4,4}	optimal

Figure 5.9: Structure of all optimal (shaded rows) and suboptimal (white rows) binary networks with $N = 4$ nodes. Each network is classified according to the number of connections m (rows) and geometric degeneracy g_d (columns). The highlighted column (leftmost) shows a path from an optimal tree ($m = 3$) to a fully connected network ($m = 12$) which contains only nonsensitive configurations ($g_d = 1$).

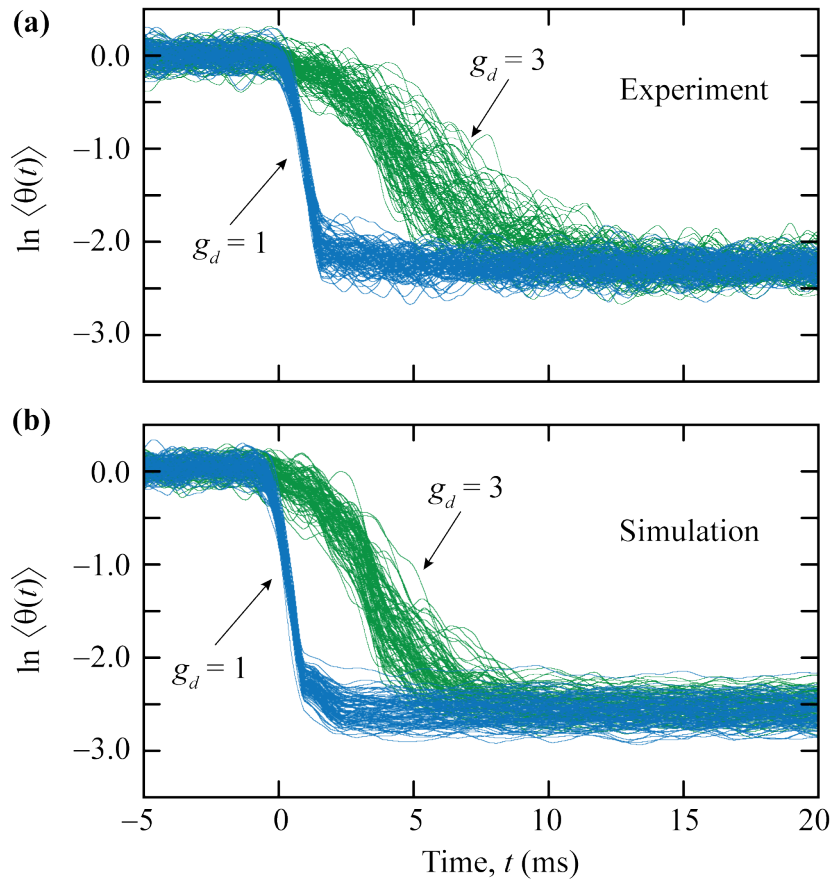


Figure 5.10: Differentiating behavior between sensitive and nonsensitive networks. Experimentally measured convergence transient $\langle \theta(t) \rangle$ for the nonsensitive star configuration ($g_d = 1$) and the sensitive linear chain configuration ($g_d = 3$). The coupling is enabled at $t = 0$. (b) Results from numerical simulations.

ments, the convergence transient to synchrony is systematically different for these networks. It is also seen that, even though measurements for both the networks are performed under similar conditions, the curves corresponding to the linear chain configuration ($g_d = 3$) have a larger variability compared to those for the star configuration ($g_d = 1$). Since the experiments and simulations show that network configurations with non-diagonalizable matrices have a greater susceptibility to noise and parameter mismatches, we call these networks *sensitive networks*. On the other hand, networks with $g_d = 1$ are referred to as *nonsensitive networks*. Also, we find that while the nonsensitive star configuration has an exponential convergence to synchronization, the sensitive linear chain topology has a non-exponential transient, in agreement with theoretical predictions [57, 81]. To illustrate this qualitative difference between the sensitive and the non-sensitive configurations in their approach to synchrony, we consider a simplified linear model that captures the essential features of the problem. Consider the equation

$$\frac{d\boldsymbol{\xi}}{dt} = -\mathbf{J}\boldsymbol{\xi}, \quad (5.6)$$

which is the generic form of variational equations for diffusively coupled oscillators [33]. Here $\boldsymbol{\xi} = (\xi_1, \xi_2, \dots, \xi_N)$ represents the synchronization errors along various eigenmodes [82, 83] indexed as $l = 1, 2, \dots, N$. For the purpose of comparing non-sensitive and sensitive optimal networks, it suffices to consider two types of the Jacobian coupling matrix \mathbf{J} (with linearly independent and dependent eigenvectors) that have the same set of eigenvalues but different geometric degeneracies: $\mathbf{J}^{(n)} = \lambda \mathbf{I}_{N \times N}$, where $\lambda > 0$ and $\mathbf{J}^{(s)} = \mathbf{J}^{(n)} + (\delta_{i,j+1})_{N \times N}$. We denote the states of these two

systems by $\boldsymbol{\xi}^{(n)} = (\xi_l^{(n)})$ and $\boldsymbol{\xi}^{(s)} = (\xi_l^{(s)})$ respectively. We note that even though $\mathbf{J}^{(n)}$ and $\mathbf{J}^{(s)}$ both have the same eigenvalues, $\mathbf{J}^{(n)}$ is diagonalizable (with $g_d = 1$) while $\mathbf{J}^{(s)}$ is not (with $g_d = N - 1$). The exact solution of Eqn. 5.6 for both cases can be expressed as

$$\begin{aligned}\xi_l^{(n)} &= [\xi_l^{(n)}(0)] e^{-\lambda t}, \\ \xi_l^{(s)}(t) &= \sum_{k=1}^l (-1)^{(l-k)} [\xi_l^{(s)}(0)] \frac{t^{l-k}}{(l-k)!} e^{-\lambda t}.\end{aligned}\quad (5.7)$$

The dominant eigenstates (the ones that decay the slowest) are $\xi_N^{(n)}(t)$ and $\xi_N^{(s)}(t)$ respectively. From Eqns. 5.7, we see that $\xi_N^{(n)}(t)$ decays exponentially while the decay of $\xi_N^{(s)}(t)$ is of the form $g(t)e^{-\lambda t}$, where $g(t)$ is a polynomial function of order $N - 1$. We note that the asymptotic ($t \rightarrow \infty$) behavior of $\xi_N^{(s)}(t)$ is the same as that of $\xi_N^{(n)}(t)$, but the transient is not. In experiments, the time it takes to reach the synchronization floor (caused by parameter mismatches and noise) could be relatively short rendering a measurement of the asymptotic exponential convergence rate impossible.

In our linear model above, we chose an extreme case of $\mathbf{J}^{(s)}$ with $g_d = N - 1$. In general, the order of the polynomial transient is equal to the coupling matrix geometric degeneracy g_d . In Fig. 5.11 we show simulated transient behavior for configurations with varying values of g_d for a 50-node network with $m = 49$ links. Again, we add an observational noise term and a 1% coupling link and feedback strength mismatch. From the results, we clearly see that the duration of the polynomial transient increases as the geometric degeneracy increases. In order to further establish the generality our observations with respect to coupling link density, we

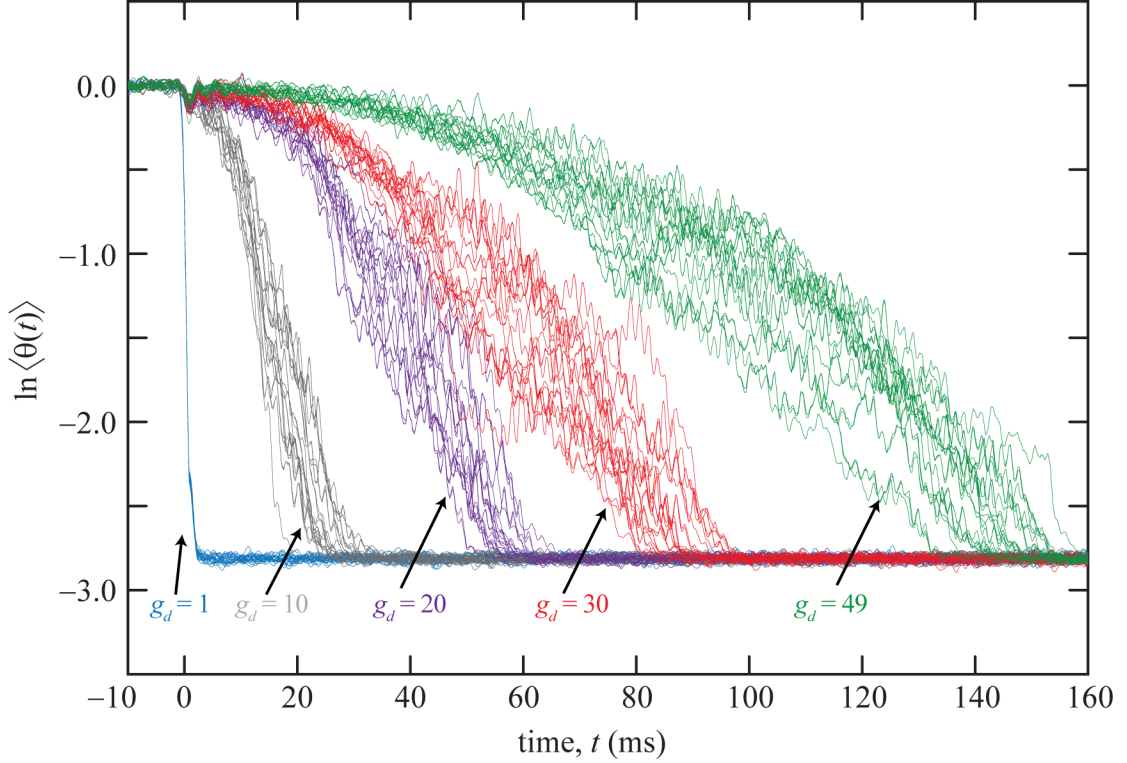


Figure 5.11: Simulated convergence transient $\langle\theta(t)\rangle$ of 50-node network configurations with various values of g_d . The coupling is enabled at $t = 0$. While the nonsensitive network ($g_d = 1$) has an exponential transient, sensitive networks ($g_d > 1$) show a markedly different nonexponential transient. We see that the higher the geometric degeneracy, the longer the polynomial transient.

performed the same simulations for 50-node networks with $m = 98$ links and $g_d = 1$ and $g_d = 15$. The network configurations for these cases are shown in Fig. 5.12 (a) and (b). The transient behavior for the two networks is shown in Fig. 5.12 (c). Again, we observe that while the nonsensitive configuration with $g_d = 1$ has an exponential transient, the sensitive configuration ($g_d = 15$) shows a non-exponential trend with a larger variability.

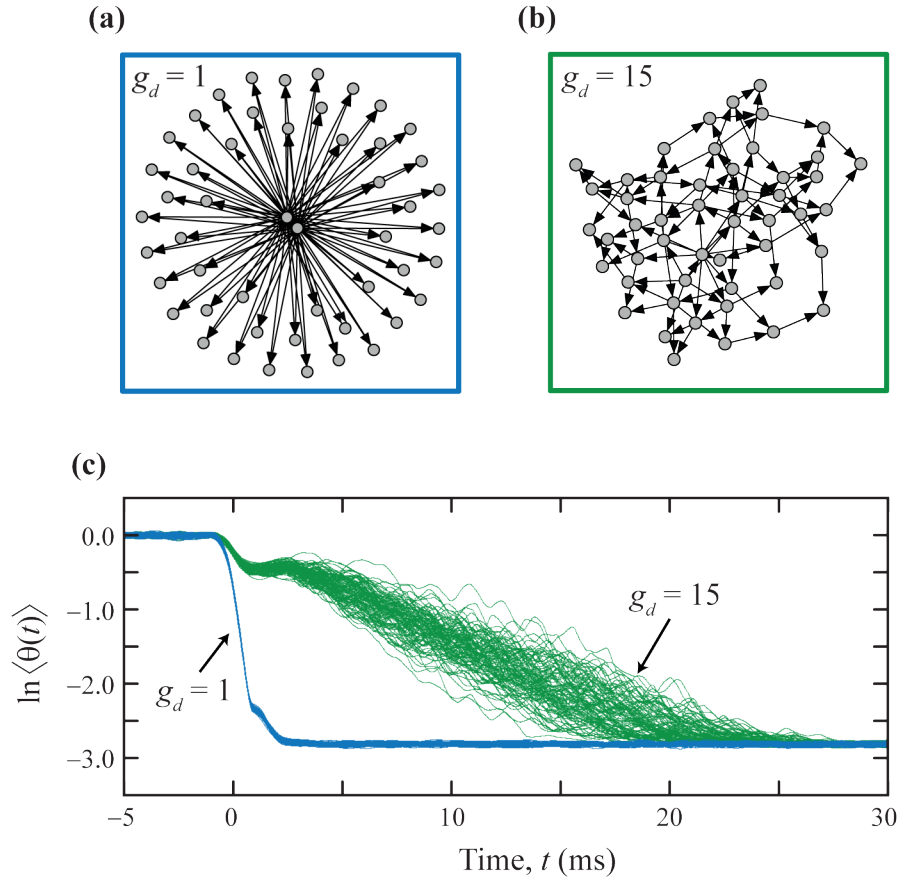


Figure 5.12: Transient to synchronization for sensitive and nonsensitive networks with $N = 50$ nodes. (a, b) Configurations with $m = 98$ links and $g_d = 1$ and 15, respectively. (c) Simulated convergence transient $\langle \theta(t) \rangle$.

5.6 Summary

In this chapter, we considered the influence of network structure on the synchronization properties of dynamical networks. Using experimental observations from a 4-node network of optoelectronic oscillators we verified that the configurations that lead to optimal synchronization properties have a degenerate eigenvalue spectrum as predicted in Ref. [41]. Further, using simulations, we showed that this prediction may in fact be extended to be true for any network size N . Within the set of optimal networks, we identified configurations that are sensitive to perturbations to the network structure (sensitive networks) and ones that are less affected by such changes (non-sensitive networks). We analytically derived and experimentally demonstrated that the approach to synchrony for sensitive and non-sensitive networks is different though they have the same eigenvalue spectrum.

Chapter 6

Conclusions and Future Research

6.1 Conclusions

Synchronization of chaos is an interesting phenomenon with implications for many fields of science and technology. From a basic science point of view, the study of synchronization of chaos can lead to a better understanding of the collective behavior exhibited by many complex networks encountered in nature. From a technological standpoint, several practical applications of this phenomenon have been proposed. Synchronization of chaos finds application in secure communications, weather prediction models, parameter estimation and sensing. Though a huge amount of past research on dynamical systems has been devoted to the fascinating idea of chaos synchronization, a large proportion of it has been theoretical. In this thesis, we presented an experimental study of the synchronism of chaos using networks of nonlinear optoelectronic time-delayed feedback oscillators. Our modular optoelectronic oscillators are easy to assemble and built using readily available optical and electronic equipment.

In Chapter 2, we characterized the dynamical behavior of our nonlinear optoelectronic feedback loop. We observed that the feedback loop can exhibit a wide variety of dynamical behaviors, ranging from simple periodic oscillations to very complicated high-dimensional chaos, as the feedback parameters are varied. We

also developed a mathematical model to describe the dynamics of our optoelectronic system based on the operating characteristics of its components. We find a good correspondence between experimental observations and numerical simulations of our model.

In Chapter 3, we performed a detailed characterization of the synchronized behavior of coupled optoelectronic oscillators. We explored the range of coupling parameters for which optoelectronic oscillators are stably synchronized. Our experimental observations show good correspondence with results obtained from numerical simulations. We also presented details of the master stability function formulation which can be used to extend the results derived from a network with a small number of oscillators to arbitrarily large networks.

In Chapter 4, we presented details of an experimental demonstration of a recently proposed adaptive synchronization scheme designed to maintain synchronization in a network of chaotic oscillators even when the coupling strengths are unknown and changing in time. Our research in this direction has implications for chaos-based encrypted communication applications which critically depend on the maintenance of high-quality synchronization robust to environmental perturbations. In maintaining global network synchrony, the adaptive scheme also produces a real-time estimate of the coupling strength fluctuations. Using a network of three optoelectronic systems, we demonstrated the tracking of simultaneous coupling perturbations occurring in multiple network links. Through this experiment, we established the potential utility of a network of chaotic oscillators for sensing applications.

Next, in Chapter 5, we considered the important problem of the interplay between network dynamics and the underlying coupling topology. Using a network of four chaotic optoelectronic oscillators with a configurable connection topology, we experimentally explored the dependence of synchronization properties, such as the rate of convergence to synchronization and the parameter range for stable synchronization, on the number of network links. Our findings show that having more network links does not necessarily imply better synchronization properties. Our observations are consistent with a recently proposed theoretical study which identified, based on a synchronizability measure determined purely from the eigenvalues of the coupling matrix, network configurations that are optimal for the establishment of synchrony. Further, contrary to what has been previously thought (based on theoretical analysis), we noticed that networks with the same eigenvalue spectra (and consequently the same synchronizability measure) can exhibit different convergence rates to synchronization. This difference manifests in real-life situations due to the presence of unavoidable noise and parameter mismatches. In fact, for certain cospectral configurations, our observations reveal a marked qualitative difference in the nature of the approach to synchrony. We explain this difference in terms of the properties of the eigenvectors of the coupling matrix. Network configurations with diagonalizable coupling matrices exhibit an exponential convergence transient to synchronization while those described by nondiagonalizable coupling matrices exhibit a polynomial convergence transient. We also find that nondiagonalizable configurations are more sensitive to perturbations to the network structure.

6.2 Discussion: Generality and Significance of Results Presented

In this thesis, we presented experimental results addressing two important aspects of chaos synchronization:

- The adaptive maintenance of global network synchrony when the couplings are unpredictable and time-dependent and
- the influence of the connection topology on global network synchronization properties.

Our experiments are performed on fiber-optic networks consisting of either three or four chaotic optoelectronic nodes. However, we note that the theoretical basis of our experiments is general and applicable to networks of arbitrary size and consisting of arbitrary dynamical nodes [27, 41]. The master stability function (which can be completely determined using a network of three oscillators) approach, allows us to extend our experimental results to arbitrarily large networks. In fact, numerical simulations of larger networks comprising 50 optoelectronic nodes (shown in Figs. 5.5, 5.11, and 5.12) agree with the predictions obtained from the MSF analysis and explicitly establish the independence of our results with respect to network-size [42, 68].

Further, simulations performed in the process of designing our experiments (not shown here) indicate that the results reported in this thesis are not limited to the specific set of system parameters chosen in our experiments. For example, we find that changing the net feedback loop gain leads to results that are qualitatively similar to what have been included in the thesis. This is justified by the fact that the master

stability function, on which our theory is based, retains its qualitative form even as the feedback strength of our optoelectronic oscillators is changed (but, such that the dynamics is still chaotic) [68]. Also, in carrying out our study of the influence of connection topology on synchronization, we have simulated networks comprised of Bernoulli map oscillators and obtained results (not shown here) similar to what have been reported in the thesis. Specifically, we observed that the rate of convergence to synchronous solution depends nonmonotonically on the number of network links with the convergence rate being maximized for networks with a minimal eigenvalue spread (optimal networks). This indicates that our experiments represent a case of behavior which is generic to networks of chaotic dynamical systems.

Finally, we note that our experiments can be scaled to operate at arbitrarily fast time scales by using either RF analog signal processing or faster digital signal processing. This has practical implications to the construction of sensor networks capable of tracking faster variations compared to what have been imposed in our experiments. Our optoelectronic feedback loops, constructed from readily available standard optoelectronic equipment thus offer a convenient and versatile test bed to study synchronization properties of complex networks in general.

6.3 Future Directions

The research presented in this thesis can be considered as a starting point for a deeper exploration of various aspects of chaos synchronization through experiments. It will be very interesting to consider the application of the methods developed

here to larger, more complex networks commonly encountered in the real-world. For example, synchronization plays a crucial role in power-grids. For the effective operation of a power-grid, various generating stations (can be modeled as dynamical oscillators) need to operate in lock-step with each other. Our study on the interplay of connection topology and network synchronization can potentially provide insights into the designing of grid systems. Perhaps a first step in this direction would be to scale our experiments to incorporate a large number of network nodes.

An optical network with a large number of nodes similar to those considered in our research can be realized using an assembly comprising a spatial light modulator (SLM) and a camera. A spatial light modulator is a device that can impose an arbitrary spatial pattern on a propagating optical wave front. This is accomplished by the many pixels of the SLM acting as independently configurable optical intensity modulators. Each SLM pixel is essentially a polarizer-analyzer assembly, whose transmission can be adjusted by offsetting their polarization axes suitably via an input electronic signal. In fact, the transmission characteristic of each SLM pixel follows a trigonometric nonlinearity much like our electro-optic modulators. The output optical wave front of the SLM can then be detected using a camera whose pixels act as independent photoreceivers. The output of the camera can be suitably processed and used as a feedback signal to modulate the SLM output at a later point of time. This allows us to create a large number of nonlinear feedback oscillators, similar to our optoelectronic system, which can be coupled by superposing the intensity signals as detected by various pixels of the camera. The network topology in this case can be controlled accurately by adjusting how the information

from various pixels is superposed. Using this configurable network, one can model networks which are comparable in size to real world complex networks.

As part of this thesis, we also presented the details of an experimental implementation of an adaptive strategy that maintains synchronization even when the network coupling strengths are unknown and time-dependent. A possible extension to this line of research is to broaden the scope of the adaptive algorithm to include situations where the node parameters (such as the feedback time-delay, the feedback strength, etc ...) may be fluctuating in time. This scenario can serve as a model for many natural complex systems (such as neurons in the brain whose firing rates can change depending on external chemical concentrations) and help us gain insight into the development of collective behavior in nature.

Finally, it would be of great interest to consider an amalgamation of the two central ideas discussed in this thesis: adaptive synchronization techniques and network topologies optimal for synchronization. Implementation of the adaptive synchronization scheme on a network configured to be optimally synchronizable, can lead to the establishment of robust synchronization necessary for many practical applications.

Bibliography

- [1] H. Goldstein, C. Poole, and J. Safko. *Classical Mechanics*. Addison Wesley, Boston, MA, third edition, 2001.
- [2] M. C. Mackey and L. Glass. Oscillation and chaos in physiological control systems. *Science*, 197(4300):287–289, 1977.
- [3] J. E. Skinner. Low-dimensional chaos in biological systems. *Nature Biotechnology*, 12(6):596–600, 1994.
- [4] I. R. Epstein. Oscillations and chaos in chemical systems. *Physica D: Nonlinear Phenomena*, 7(1-3):47–56, 1983.
- [5] Y. Kuramoto. *Chemical Oscillations, Waves, and Turbulence*. Dover Publications, New York, NY, 2003.
- [6] T. Matsumoto. Chaos in electronic circuits. *Proceedings of the IEEE*, 75(8):1033–1057, 1987.
- [7] L. O. Chua, C. W. Wu, A. Huang, and G.-Q. Zhong. A universal circuit for studying and generating chaos. *IEEE Transactions on Circuits and Systems I: Fundamental Theory and Applications*, 40(10):732–744, 1993.
- [8] H. M. Gibbs, F. A. Hopf, D. L. Kaplan, and R. L. Shoemaker. Observation of chaos in optical bistability. *Phys. Rev. Lett.*, 46(7):474–477, 1981.
- [9] K. Ikeda and K. Matsumoto. High-dimensional chaotic behavior in systems with time-delayed feedback. *Physica D: Nonlinear Phenomena*, 29(1-2):223–235, 1987.
- [10] H. Fujisaka and Y. Yamada. Stability theory of synchronized motion in coupled-oscillator systems. *Progress of Theoretical Physics*, 69(1):32–47, 1983.
- [11] V. S. Afraimovich, N. N. Verichev, and M. I. Rabinovich. Stochastic synchronization of oscillation in dissipative systems. *Radiophysics and Quantum Electronics*, 29(9):795–803, 1986.
- [12] L. M. Pecora and T. L. Carroll. Synchronization in chaotic systems. *Phys. Rev. Lett.*, 64(8):821–824, 1990.
- [13] S. H. Strogatz. *SYNC: The Emerging Science of Spontaneous Order*. Hyperion, New York, NY, first edition, 2003.
- [14] L. Glass. Synchronization and rhythmic processes in physiology. *Nature*, 410(6825):277–284, 2001.

- [15] K. Wiesenfeld, P. Colet, and S. H. Strogatz. Synchronization transitions in a disordered Josephson series array. *Phys. Rev. Lett.*, 76(3):404–407, 1996.
- [16] R. Roy and K. S. Thornburg. Experimental synchronization of chaotic lasers. *Phys. Rev. Lett.*, 72(13):2009–2012, 1994.
- [17] J. R. Terry, K. S. Thornburg, D. J. DeShazer, G. D. VanWiggeren, S. Zhu, P. Ashwin, and R. Roy. Synchronization of chaos in an array of three lasers. *Phys. Rev. E*, 59(4):4036–4043, 1999.
- [18] I. Cohen, V. Navarro, S. Clemenceau, M. Baulac, and R. Miles. On the origin of interictal activity in human temporal lobe epilepsy in vitro. *Science*, 298(5597):1418–1421, 2002.
- [19] E. Ott. *Chaos in Dynamical Systems*. Cambridge University Press, Cambridge, U. K., second edition, 2002.
- [20] T. Erneux. *Applied Delay Differential Equations*. Springer, first edition, 2009.
- [21] X. S. Yao and L. Maleki. Optoelectronic microwave oscillator. *J. Opt. Soc. Am. B*, 13(8):1725–1735, 1996.
- [22] A. Argyris, D. Syvridis, I. Larger, V. Annovazzi-Lodi, P. Colet, I. Fischer, J. García-Ojalvo, C. R. Mirasso, L. Pesquera, and K. A. Shore. Chaos-based communications at high bit rates using commercial fibre-optic links. *Nature*, 438(7066):343, 2005.
- [23] K. M. Cuomo and A. V. Oppenheim. Circuit implementation of synchronized chaos with applications to communications. *Phys. Rev. Lett.*, 71(1):65–68, 1993.
- [24] G. D. VanWiggeren and R. Roy. Communication with chaotic lasers. *Science*, 279(5354):1198–1200, 1998.
- [25] A. B. Cohen, B. Ravoori, T. E. Murphy, and R. Roy. Using synchronization for prediction of high-dimensional chaotic dynamics. *Phys. Rev. Lett.*, 101(15):154102, 2008.
- [26] J. C. Quinn, P. H. Bryant, D. R. Creveling, S. R. Klein, and H. D. I. Abarbanel. Parameter and state estimation of experimental chaotic systems using synchronization. *Phys. Rev. E*, 80(1):016201, 2009.
- [27] F. Sorrentino and E. Ott. Adaptive synchronization of dynamics on evolving complex networks. *Phys. Rev. Lett.*, 100(11):114101, 2008.
- [28] G. Jakimoski and L. Kocarev. Analysis of some recently proposed chaos-based encryption algorithms. *Phys. Lett. A*, 291(6):381 – 384, 2001.
- [29] I. Kanter, E. Kopelowitz, and W. Kinzel. Public channel cryptography: Chaos synchronization and Hilbert’s tenth problem. *Phys. Rev. Lett.*, 101(8):084102, 2008.

- [30] G. D. VanWiggeren and R. Roy. Optical communication with chaotic waveforms. *Phys. Rev. Lett.*, 81(16):3547–3550, 1998.
- [31] B. Ravoori, A. B. Cohen, A. V. Setty, F. Sorrentino, T. E. Murphy, E. Ott, and R. Roy. Adaptive synchronization of coupled chaotic oscillators. *Phys. Rev. E*, 80(5):056205, 2009.
- [32] A. B. Cohen, B. Ravoori, F. Sorrentino, T. E. Murphy, E. Ott, and R. Roy. Dynamic synchronization of a time-evolving optical network of chaotic oscillators. *Chaos*, 20(4):043142, 2010.
- [33] L. M. Pecora and T. L. Carroll. Master stability functions for synchronized coupled systems. *Phys. Rev. Lett.*, 80(10):2109–2112, 1998.
- [34] M. Barahona and L. M. Pecora. Synchronization in small-world systems. *Phys. Rev. Lett.*, 89(5):054101, 2002.
- [35] T. Nishikawa, A. E. Motter, Y-C. Lai, and F. C. Hoppensteadt. Heterogeneity in oscillator networks: Are smaller worlds easier to synchronize? *Phys. Rev. Lett.*, 91(1):014101, 2003.
- [36] P. N. McGraw and M. Menzinger. Clustering and the synchronization of oscillator networks. *Phys. Rev. E*, 72(1):015101, 2005.
- [37] L. Kocarev and L. Amato. Synchronization in power-law networks. *Chaos*, 15(2):024101, 2005.
- [38] A. E. Motter, C. S. Zhou, and J. Kurths. Enhancing complex-network synchronization. *Europhysics Letters*, 69(3):334, 2005.
- [39] A. E. Motter, C. Zhou, and J. Kurths. Network synchronization, diffusion, and the paradox of heterogeneity. *Phys. Rev. E*, 71(1):016116, 2005.
- [40] A. E. Motter, C. Zhou, and J. Kurths. Weighted networks are more synchronizable: How and why. *AIP Conference Proceedings*, 776:201–214, 2005.
- [41] T. Nishikawa and A. E. Motter. Network synchronization landscape reveals compensatory structures, quantization, and the positive effect of negative interactions. *Proc. Natl. Acad. Sci. USA*, 107(23):10342, 2010.
- [42] B. Ravoori, A. B. Cohen, J. Sun, A. E. Motter, T. E. Murphy, and R. Roy. Robustness of optimal synchronization in real networks. *Phys. Rev. Lett.*, 107(3):034102, 2011.
- [43] M. Schanz and A. Pelster. Analytical and numerical investigations of the phase-locked loop with time delay. *Phys. Rev. E*, 67(5):056205, 2003.
- [44] Y. Chembo Kouomou, P. Colet, L. Larger, and N. Gastaud. Chaotic breathers in delayed electro-optical systems. *Phys. Rev. Lett.*, 95(20):203903, 2005.

- [45] K. E. Callan, L. Illing, Z. Gao, D. J. Gauthier, and E. Schöll. Broadband chaos generated by an optoelectronic oscillator. *Phys. Rev. Lett.*, 104(11):113901, 2010.
- [46] E. L. Wooten, K. M. Kissa, A. Yi-Yan, E. J. Murphy, D. A. Lafaw, P. F. Hallemeier, D. Maack, D. V. Attanasio, D. J. Fritz, G. J. McBrien, and D. E. Bossi. A review of lithium niobate modulators for fiber-optic communications systems. *Selected Topics in Quantum Electronics, IEEE Journal of*, 6(1):69–82, 2000.
- [47] R. W. Boyd. *Nonlinear Optics*. Academic Press, San Diego, CA, third edition, 2008.
- [48] B. G. Streetman. *Solid State Electronic Devices*. Prentice Hall, Englewood Cliffs, NJ, fourth edition, 1995.
- [49] Spectrum Digital, Inc. *TMS320C6416T DSK Technical Reference*, 508035-0001 rev. a edition, November 2004.
- [50] Spectrum Digital, Inc. *TMS320C6713 DSK Technical Reference*, 506735-0001 rev. b edition, November 2003.
- [51] Curtiss-Wright Controls, Inc. *AD3000 3GSPS Analog Input XMC/PMC with Xilinx Virtex-5 FPGA*, mkt-ds-ad3000-060809v4 edition, 2008. http://www.cwembedded.com/ad3000_fpga_processing.htm.
- [52] A. V. Oppenheim, R. W. Schaffer, and J. R. Buck. *Discrete-time signal processing*. Prentice Hall, New Jersey, NJ, second edition, 1999.
- [53] Y. C. Kouomou. *Nonlinear Dynamics of Semiconductor Laser Systems with Feedback: Applications to Optical Chaos Cryptography, Radar Frequency Generation, and Transverse Mode Control*. PhD thesis, University of the Balearic Islands, Palma de Mallorca, Spain, 2006.
- [54] A. Arenas, A. Diaz-Guilera, J. Kurths, Y. Moreno, and C. Zhou. Synchronization in complex networks. *Phys. Rep.*, 469(3):93, 2008.
- [55] T. E. Murphy, A. B. Cohen, B. Ravoori, K. R. B. Schmitt, A. V. Setty, F. Sorrentino, C. R. S. Williams, E. Ott, and R. Roy. Complex dynamics and synchronization of delayed-feedback nonlinear oscillators. *Philosophical Transactions of the Royal Society A: Mathematical, Physical and Engineering Sciences*, 368(1911):343–366, 2010.
- [56] W. J. Rugh. *Linear System Theory*. Prentice Hall, New Jersey, second edition, 1996.
- [57] T. Nishikawa and A. E. Motter. Synchronization is optimal in nondiagonalizable networks. *Phys. Rev. E*, 73(6):065106, 2006.

- [58] D. M. Cvetkovic, M. Doob, and H. Sachs. *Spectra of Graphs: Theory and Applications*. Johann Ambrosius Barth Verlag, Heidelberg, Germany, 1995.
- [59] F. Mossayebi, H. K. Qammar, and T. T. Hartley. Adaptive estimation and synchronization of chaotic systems. *Phys. Lett. A*, 161(3):255 – 262, 1991.
- [60] C. R. Johnson Jr. and J. S. Thorp. An adaptive calibration algorithm for synchronized chaos. *Signal Processing Letters, IEEE*, 1(12):194 –195, 1994.
- [61] U. Parlitz and L. Kocarev. Multichannel communication using autosynchronization. *International Journal of Bifurcation and Chaos in Applied Sciences and Engineering*, 6(3):581–588, 1996.
- [62] C. W. Wu, T. Yang, and L. O. Chua. On adaptive synchronization and control of nonlinear dynamical systems’. *International Journal of Bifurcation and Chaos in Applied Sciences and Engineering*, 6(3):455–471, 1996.
- [63] L. O. Chua, T. Yang, G.-Q. Zhong, and C. W. Wu. Adaptive synchronization of Chua’s oscillators. *International Journal of Bifurcation and Chaos in Applied Sciences and Engineering*, 6(1):189–201, 1996.
- [64] S. Boccaletti, A. Farini, and F. T. Arecchi. Adaptive synchronization of chaos for secure communication. *Phys. Rev. E*, 55(5):4979–4981, 1997.
- [65] D. J. Sobiski and J. S. Thorp. PDMA-1: Chaotic communication via the extended Kalman filter. *Circuits and Systems I: Fundamental Theory and Applications, IEEE Transactions on*, 45(2):194 –197, 1998.
- [66] J. Ito and K. Kaneko. Spontaneous structure formation in a network of chaotic units with variable connection strengths. *Phys. Rev. Lett.*, 88(2):028701, 2001.
- [67] F. Sorrentino and E. Ott. Using synchronism of chaos for adaptive learning of time-evolving network topology. *Phys. Rev. E*, 79(1):016201, 2009.
- [68] A. B. Cohen. *Synchronization and prediction of chaotic dynamics on a network of optoelectronic oscillators*. PhD thesis, University of Maryland, College Park, Maryland, 2011.
- [69] R. Pastor-Satorras and A. Vespignani. Epidemic spreading in scale-free networks. *Phys. Rev. Lett.*, 86(14):3200, 2001.
- [70] M. E. J. Newman. Spread of epidemic disease on networks. *Phys. Rev. E*, 66(1):016128, 2002.
- [71] J. C. Miller. Percolation and epidemics in random clustered networks. *Phys. Rev. E*, 80(2):020901, 2009.
- [72] C. Kamp. Untangling the interplay between epidemic spread and transmission network dynamics. *PLoS Comput. Biol.*, 6(11):e1000984, 2010.

- [73] D. J. Watts. A simple model of global cascades on random networks. *Proc. Natl. Acad. Sci. USA*, 99(9):5766, 2002.
- [74] Z. Y. Chen and X. F. Wang. Effects of network structure and routing strategy on network capacity. *Phys. Rev. E*, 73(3):036107, 2006.
- [75] C. Zhou, A. E. Motter, and J. Kurths. Universality in the synchronization of weighted random networks. *Phys. Rev. Lett.*, 96(3):034101, 2006.
- [76] S. Boccaletti, D. U. Hwang., M. Chavez, A. Amann, J. Kurths, and L. M. Pecora. Synchronization in dynamical networks: Evolution along commutative graphs. *Phys. Rev. E*, 74(1):016102, 2006.
- [77] D. A. Wiley, S. H. Strogatz, and M. Girvan. The size of the sync basin. *Chaos*, 16(1):015103, 2006.
- [78] E. M. Izhikevich. Synchronization of elliptic bursters. *SIAM Review*, 43(2):315–344, 2001.
- [79] Y. Gao and J. Wang. Oscillation propagation in neural networks with different topologies. *Phys. Rev. E*, 83(3):031909, 2011.
- [80] K. Pablo, S. Charlotte, and M. Hildegard. Noise as control parameter in networks of excitable media: Role of the network topology. *Phys. Rev. E*, 82(3):036104, 2010.
- [81] T. Nishikawa and A. E. Motter. Maximum performance at minimum cost in network synchronization. *Physica D (Amsterdam)*, 224(1-2):77, 2006.
- [82] J. Sun, E. M. Bollt, and T. Nishikawa. Master stability functions for coupled nearly identical dynamical systems. *Europhysics Letters*, 85(6):60011, 2009.
- [83] A. Milanese, J. Sun, and T. Nishikawa. Approximating spectral impact of structural perturbations in large networks. *Phys. Rev. E*, 81(4):046112, 2010.